

Design and Analysis of Graphene Surface Plasmon Biosensors

by

Md. Mahbub Hossain

DOCTOR OF PHILOSOPHY



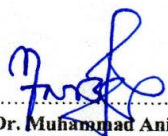
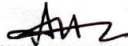
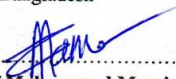


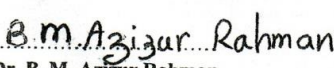
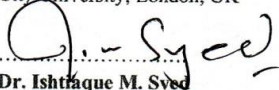
**Department of Electrical and Electronic Engineering
BANGLADESH UNIVERSITY OF ENGINEERING AND
TECHNOLOGY**

November 2022

APPROVAL

The thesis titled “**DESIGN AND ANALYSIS PLASMON BIOSENSORS**” submitted by Mr. 1014064001, Session: October 2014 to the Department of Engineering and Technology has been accepted as the requirement for the degree of **Doctor of Philosophy**

BOARD OF EXAMINERS

1. 
.....
Dr. Muhammad Anisuzzaman Talukder
Professor
Department of Electrical and Electronic Engineering
BUET, Dhaka, Bangladesh
2. 
.....
Dr. Md. Aynal Haque
Professor and Head
Department of Electrical and Electronic Engineering
BUET, Dhaka, Bangladesh
3. 
.....
Dr. Md. Sharif Mohammad Mominuzzaman
Professor
Department of Electrical and Electronic Engineering
BUET, Dhaka, Bangladesh
4. 
.....
Dr. Md. Shah Alam
Professor
Department of Electrical and Electronic Engineering
BUET, Dhaka, Bangladesh
5. 
.....
Dr. Md. Zahurul Islam
Professor
Department of Electrical and Electronic Engineering
BUET, Dhaka, Bangladesh
6. 
.....
Dr. B. M. Azizur Rahman
Professor
Electrical and Electronic Engineering
City University, London, UK
7. 
.....
Dr. Ishtiaque M. Syed
Professor
Department of Physics
University of Dhaka, Dhaka, Bangladesh

Declaration

It is hereby declared that this thesis is an original work, both in terms of research content and narrative, and has not been submitted elsewhere, in part or in full, for a degree.

Signature of the Candidate



Md. Mahbub Hossain

Acknowledgements

At first, I would like to express my sincere gratitude to the Almighty Allah whose leniency and kindness enabled me to complete the Ph.D. thesis successfully. There are no proper words I found to correctly describe His blessings that I have enjoyed my Ph.D. research. It was very difficult situation for me to start my Ph.D. without any funding and living in Dhaka. However, I am very much thankful to the Almighty that He gave me the patience, kept me healthy, and made my time more productive in the entire period of my Ph.D. study even so during the time of Corona pandemic.

I would say thanks to my supervisor Prof. Dr. Muhammad Anisuzzaman Talukder to guide me well throughout the research work from the research area selection to finding the results. His immense knowledge, motivation and patience have given me more power and spirit to excel in my research. He was always accessible and willing to help during the thesis period. He unhesitatingly provided all the resources and assistance for successful execution of this thesis when I used the Photonics laboratory. His keen sight and judicious advice have given me precise guiding framework of the Ph.D. research. He also taught me how to do research and feel love with research. He is my mentor and best academic advisor beyond my imagination. Prof. Dr. Muhammad Anisuzzaman Talukder has given me a marvelous amount of freedom to set my own researches and finds new solutions of the problem. I always feel proud and happy to pursue my Ph.D. research under his supervision.

I have encouraged from many inspiring conversations with Prof. Dr. Md. Shah Alam, and great honor for his deepest knowledge and unbeatable passion in scattering matrix and finite element method. It was my pleasure to attend his class meetings since November 2014. I would not forget to express the appreciation to rest of the Doctoral Committee members such as Dr. Sharif Mohammad Mominuzzaman, Dr. Md. Zahurul Islam, Dr. Md. Aynal Haque (Head, Department of EEE), and Dr. Md. Kamrul Hasan (Former Head, Department of EEE) for giving

me the inspiration and sharing perceptive suggestions. They all have played a key role in improving my research writing skills.

I must acknowledge the persistent support of Prof. Dr. B. M. Azizur Rahman, City University London, UK. He has been very considerate and enthusiastically supported my work on graphene surface plasmon. His enormous knowledge and abundant experience in photonics research have encouraged me in all the time of my academic carrier. I also give an immense thanks and grateful to Prof. Dr. Ishtiaque M. Syed, Department of Physics, University of Dhaka for all his valuable guidance, and outstanding feedback. I also thanks Prof. Dr. Farseem Mannan Mohammedy for his inspiration in my Ph.D. study.

I am truly indebted to all of my teachers who have taught me in various stages in my life. All of them have played very important roles in my education as well as in my practical life. I would like to thank all the past fellow members of the Nanophotonics Research Group. I also thank all administrative staffs in BUET especially Nasir Bhai (Department of EEE) and Selim Bhai (CASR, BUET) for their cordial cooperation made my Ph.D. life easier. Along with this, I would like to acknowledge the Khulna University authority for their support in my Ph.D. study such as allowed study leave as well as earned leave when required.

Lastly, I would like to acknowledge my family for their diligent love, inspiration and support over the long period in my Ph.D. study. My mother (Mrs. Chamon Ara Begum) as usual her altruistic supports during my Ph.D. She was made me mentally strong when I was suffering Anal related medical problem and needed moderate surgery in the middle of this year. I am grateful to my Father-in-law (Md. Abdul Wahab), my sister (Roshena Hossain), Brother-in-law (Kazi. Bazlur Rahman), wife (Sabrina Milky), uncle (Rejaul Islam), and eldest son (Ehan) and other family members, relatives, and colleagues. They always support me and encourage me with their best wishes, inspiration and suggestions.

Dedicated to My Father Late Md. Yawar Hossain

Abstract

Absorption of incident light is the most critical property of surface plasmon resonance (SPR) biosensors. Besides, damping of electron oscillations in metal is another significant issue. Hence, the reflected light intensity-profile is widened. Instead, SPR-based Kretschmann biosensors show poor magnetic response and their magnetic properties have never been applied for biosensing. We have proposed the use of magnetic resonance of a Kretschmann based SPR biosensor which is promising in biosensing. Moreover, a SPR-based glucose sensor is proposed where monolayer graphene optical property is controlled by applying a suitable gate voltage (V_g). We find that the sensor performance parameters such as figure-of-merit and sensitivity are improved by 49.57% and 21.48%, respectively when $V_g = 20$ V applied to the graphene monolayer. We use a linear regression model to calculate the detection accuracy of the blood sugar level. We observe the detection error in 4.75% on an average and within 7.40% of the worst-case situation when temperature changes by $\pm 10^\circ$ C from a reference 25° C.

Precise detection of ultra-low-level severe acute respiratory syndrome coronavirus 2 (SARS-CoV-2) is censoriously important, recently. We have proposed a SPR sensor with multi-layer graphene to detect the SARS-CoV-2. The proposed sensor has detected as small as ~ 1 fM SARS-CoV-2, S-protein concentration. However, using multi-layer graphene in SPR biosensors show low detection accuracy. Then, a graphene photonic crystals-based Tamm plasmon and surface plasmon hybrid mode for hemoglobin detection is proposed. We use double-dips method which shows polarization-dependent behavior where the maximum sensitivity is 314.5 degree/RIU when hemoglobin level is 189 g/L. From terahertz to mid infrared wavelength range, graphene shows a metallic response that supports high light confinement. We have shown that transverse magnetic mode is created in graphene at the visible spectrum by applying a suitable V_g and appropriate ZnO thickness. We have proposed graphene nanostrips-based dual-channel refractive index sensor, an optimistic alternative to the traditional Kretschmann arrangement where no need of noble metal in the structure. The propose sensor gives a maximum 2530 degree/RIU sensitivity when both the sensing channels have the same refractive index.

Contents

Approval	ii
Declaration	iii
Acknowledgements	iv
Abstract	vii
List of Figures	xi
List of Tables	xv
Abbreviations	xvi
Symbols	xviii
List of Publications	xix
1 INTRODUCTION	1
2 OPTICAL MAGNETISM IN SPR-BASED SENSOR FOR ENHANCED PERFORMANCES	15
2.1 Introduction.....	16
2.2 Theoretical Modeling	18
2.3 Sensor Structure and Simulation Setup.....	21
2.4 Feasible Experimental Setup.....	22
2.5 Results and Discussions	23
2.6 Conclusion	29
3 GATE-CONTROLLED GRAPHENE SPR GLUCOSE SENSOR	31
3.1 Introduction.....	32

3.2	Sensor Configuration.....	35
3.3	Theoretical Modeling	37
3.3.1	Optical Properties	37
3.3.2	Response to the Incident Light.....	40
3.4	Simulation Approach.....	41
3.5	Results and Discussion.....	42
3.5.1	Sensor Performance.....	42
3.5.2	Detection Accuracy	47
3.5.3	Effects of Temperature	48
3.6	Conclusion	52
4	GRAPHENE SP SENSOR FOR ULTRA-LOW-LEVEL SARS-COV-2 DETECTION	54
4.1	Introduction.....	55
4.2	Proposed Sensor.....	58
4.2.1	Configuration.....	58
4.2.2	Optimization of Layer Thicknesses	62
4.3	Modeling and Simulation	64
4.3.1	Optical Properties	64
4.3.2	Calculation of the Reflection Profile.....	67
4.3.3	Sensor Performance Parameters.....	68
4.3.4	Simulation Method.....	68
4.4	Results and Discussion.....	69
4.4.1	Detection Approach and Limit of Detection	69
4.4.2	Sensor Resolution and Binding Affinity	71
4.4.3	Sensing Performance	73
4.5	Conclusion	77
5	ANISOTROPIC GPCS-BASED TP AND SP HYBRID MODES FOR HEMOGLOBIN DETECTION	79
5.1	Introduction.....	80
5.2	Proposed Sensor.....	84
5.2.1	Configuration.....	84
5.2.2	Optimization of Sensor Structure	86
5.2.3	Anti-crossing Effect.....	87
5.2.4	Simulation Method.....	88
5.3	Modeling of the Proposed Sensor	89
5.3.1	Optical Properties	89
5.3.2	Calculation of the R-Profile	92
5.3.3	Tps and Sps Analysis	93
5.3.4	Effect of Energy Transfer.....	95
5.3.5	Sensor Performance Parameters.....	97
5.4	Sensing Performance	98

5.5	Conclusion	104
6	GRAPHENE NANOSTRIP-BASED TM MODE DUAL-CHANNEL REFRACTIVE INDEX SENSOR	106
6.1	Introduction.....	107
6.2	Sensor Structure and Materials.....	110
6.3	Optical Properties	112
6.4	Simulation Method	113
6.5	Dynamics of Incident Light.....	114
6.6	Results and Discussion.....	115
6.7	Conclusion	121
7	CONCLUSIONS	123
	Bibliography	128

List of Figures

1.1	Classification of biosensors.....	2
1.2	Basic Kretschmann configuration for creation of SPR.....	4
2.1	Schematic illustration of a feasible experimental setup for the proposed technique of the Kretschmann configuration based SPR sensor.	21
2.2	Effective constitutive parameters (a) μ_{eff} and ϵ_{eff} , and (b) n_{eff} and z for the Kretschmann based SPR sensor when n_s varying from 1.3 to 1.9.	23
2.3	Magnetic field profiles polarized in the z-direction for 633 nm incident wavelength when (a) $n_s = 1.30$, (b) $n_s = 1.546$, (c) $n_s = 1.75$ and (d) $n_s = 1.82$	24
2.4	(a) μ_{eff} and (b) R as functions of resonant incident angles for $n_s = 1.70$ and 1.71 at 633 nm incident wavelength.....	26
2.5	Variation of FWHM for μ_{eff} and R profiles, respectively as a function of specific n_s	27
2.6	Variation of (a) S and (b) FoM against n_s . The subscripts μ and R are used when the parameters are calculated using μ_{eff} and R profiles, respectively	28
3.1	Schematic illustration of the proposed gate-controlled graphene SPR glucose sensor.....	35
3.2	R vs. ϑ of the proposed sensor for different thicknesses of (a) air gap, (b) Ag, and (c) SiO ₂ . In these studies, $n_s = 1.3323$	37
3.3	Refractive index of the blood sample (n_s) as a function of blood sugar level.....	40
3.4	(a) n and μ and (b) σ and E_f of a graphene mono-layer as functions of V_g . We assume $\epsilon_0 = 8.85 \times 10^{-12} \text{ Fm}^{-1}$, $\epsilon_g = 3.9$, $d = 8 \text{ nm}$, and $e = 1.6021 \times 10^{-19} \text{ C}$	42
3.5	(a) R as a function of ϑ and (b) FWHM of the R profile as a function of the BSL of the proposed gate-controlled graphene SPR glucose sensor for different V_g . To calculate R profile, we assume $n_s = 1.3625$, which corresponds to a BSL of 78.60 mg/dl.....	43
3.6	(a) S and (b) FoM as functions of BSL of the proposed glucose sensor for different V_g	44

3.7	(a) R profile as a function of ϑ and (b) $\Delta\vartheta_r$ as functions of BSL and V_g for the proposed glucose sensor.	45
3.8	Simulation results of ϑ_r and R vs. BSL (dashed lines), and regression lines of ϑ_r and R vs. BSL (solid lines). The solid green line determines 180 mg/dl BSL, when measured $\vartheta_r = 58.8^\circ$ or $R = 0.01425$. We assume $V_g = 20$ V.	47
3.9	Effects of T on graphene (a) μ , and (b) τ for five different V_g	49
3.10	ϑ_r vs. BSL of the proposed sensor for different sensor temperature. We assume that the sample temperature remains fixed at (a) 15°C , (b) 25°C , and (c) 35°C	51
3.11	ϑ_r vs. blood sugar level for different temperatures (T) of the sensor and sample layer. The sensor and sample layer temperatures are equal and they vary simultaneously	51
4.1	Schematic illustration of the proposed graphene SPR sensor for the SARS-CoV-2 S-protein detection.....	59
4.2	Reflectance (R) of plasmonic structure in Kretschmann configuration against layer thicknesses of (a) WS_2 , (b) KNbO_3 , (c) BP (solid) and BlueP (dashed), and (d) Graphene.	62
4.3	Sensing layer refractive index (n_s) vs. SARS-CoV-2 S-protein concentration for 100- μL and 200- μL PBS solutions.....	66
4.4	(a) R -profile of the proposed graphene SPR sensor for different SARS-CoV-2 S-protein concentrations as a function of ϑ_i . In this case, SARS-CoV-2 S-proteins are added to 100- μL PBS solution. (b) $\Delta\vartheta_r$ against SARS-CoV-2 S-protein concentration for 100- μL and 200- μL PBS solution	69
4.5	(a) SR and (b) K_D as a function of S-protein concentration of the proposed graphene SPR sensor for 100- μL and 200- μL PBS solutions.	72
4.6	(a) S and (b) FoM using BP and (c) S and (d) FoM using BlueP as a function of S-protein concentration of the proposed graphene SPR sensor for 100- μL and 200- μL PBS solutions.	73
4.7	(a) Dispersion relations of the proposed sensor when S-protein concentration is 1 fM using BP. The most left straight line is the light line, (b) Propagation length, and (c) Propagation loss of the proposed sensor as a function of SARS-CoV-2 S-protein concentration for 100 μL and 200 μL PBS solutions.....	75
5.1	Schematic of the proposed anisotropic GPCs based TPs and SPs hybrid mode Hb detection sensor.	83
5.2	R -profile of the GPCs based proposed sensor as a function of ϑ_i when $n_{\text{Hb}} = 1.32919$ (a) Varying the number of GPCs unit N , and (b) Different thicknesses of Ag layer.	85

5.3	<i>R</i> -profile of the GPCs based proposed sensor as a function of polarization angle when $n_{\text{Hb}} = 1.32919$ (a) $d_{\text{Ag}} = 50$ nm, (b) $d_{\text{Ag}} = 60$ nm, and (c) $d_{\text{Ag}} = 70$ nm.....	87
5.4	(a) <i>R</i> -profile of the proposed GPCs based TPs and SPs hybrid mode when $N = 9$, $n_{\text{Hb}} = 1.32919$, and $d_{\text{Ag}} = 60$ nm, and (b) <i>R</i> -profile of the proposed GPCs based sensor using the similar sensor parameters with or without the Ag layer. The solid red line lies within the PBG at 57.52° indicates the excitation of TPs resonance mode.	93
5.5	Fourier power spectrum as a function of spatial frequency when $n_{\text{Hb}} = 1.32919$, and $d_{\text{Ag}} = 60$ nm (a) Variation the number of unit N , and (b) Different polarization angle.	95
5.6	(a) Sensing layer refractive index vs. Hb concentration, (b) $\Delta\vartheta_r$ as a function of Hb concentration for TPs resonance mode, and (c) $\Delta\vartheta_r$ as a function of Hb concentration for SPs resonance mode.	97
5.7	(a) S , (b) FWHM, and (c) FoM as a function of Hb concentration of the proposed GPCs based sensor using TPs resonance mode.	99
5.8	(a) S , (b) FWHM, and (c) FoM as a function of Hb concentration of the proposed GPCs based sensor using SPs resonance mode.....	100
5.9	(a) S , (b) FWHM, and (c) FoM as a function of Hb concentration of the proposed GPCs based sensor of TPs and SPs hybrid resonance mode applying DDM.	101
6.1	(a) 2-D schematic of the proposed graphene nanostrips based TM mode dual-channel refractive index sensor (one unit cell), and (b) 3-D schematic view of BK7, graphene-nanostrips, and ZnO of the proposed refractive index sensor.....	110
6.2	Optical properties of graphene as a function of V_g for three different thickness of ZnO (a) n_g , (b) E_f , and (c) μ_g	115
6.3	The ϵ_g of graphene as a function of wavelength. Three different thickness of ZnO where $V_g = 20$ V (a) Real, and (b) Imaginary and three different V_g where $d_{\text{ZnO}} = 5$ nm (c) Real, and (d) Imaginary	116
6.4	Observation of TM mode excitation when $d_{\text{ZnO}} = 5$ nm, $n_{S1} = n_{S2} = 1.33$, $L_a = 100$ nm, and $t_g = 50$ nm (a) $V_g = 20$ V, (b) $V_g = 40$ V, and (c) $V_g = 60$ V.	117
6.5	<i>R</i> -profile of the proposed dual-channel refractive index sensor (a) Similar n_s for both the sensing channel when $L_a = 100$ nm and $t_g = 50$ nm, (b) Variation of t_g when $L_a = 100$ nm, and $n_{S1} = n_{S2} = 1.33$, and (c) Variation of L_a when $n_{S1} = n_{S2} = 1.33$, and $t_g = 50$ nm.	118
6.6	The resonance angle shifting of the proposed structure as a function of dual-channel sensing layer refractive index (a) ϑ_{r1} , and (b) ϑ_{r2}	119
6.7	Resonance angle shifting and sensitivity analysis when both sensing channels have the same refractive index (a) Resonance angle shifting, and (b) Sensitivity	119

6.8	Sensitivity analysis of the proposed dual-channel sensor as a function of dissimilar sensing layer refractive index (a) S_1 , and (b) S_2	121
-----	---	-----

List of Tables

2.1	Comparison of FoM with previously reported sensors.	28
3.1	Refractive indices and thicknesses of different layers of the proposed glucose sensor. The refractive indices are for a 633-nm incident light.	38
3.2	Performance comparison of our proposed sensor with several recently proposed graphene-based sensors.	46
3.3	Maximum measurement error and average error of detected BSL when sensor T is varying from 25°C for different n_s temperature.....	52
3.4	Maximum and average %Error of the calculated BSL when both the sensor and sample temperatures vary.....	52
4.1	Refractive indices and thicknesses of the proposed sensor layers.....	64
4.2	Comparisons of LoD of the proposed sensor with different recently proposed sensors for SARS-CoV-2 S-protein detection.	71
4.3	Performance comparison of our proposed sensor with different recently proposed sensors.....	77
5.1	Performance comparison of our proposed sensor with different recently proposed sensors with or without using DDM.....	104

Abbreviations

ACE2	angiotensin converting enzyme 2
AEC	antibody enzyme complex
ATR	attenuated total reflectance
BK7	boro-silicate crown-glass 7
BRE	bio recognition element
BSL	blood sugar level
DDM	double dips method
FoM	figure-of-merit
FMSA	Fourier mode spectral analysis
FWHM	full width half maximum
FDTD	finite difference time domain
GPs	graphene plasmons
GPCs	graphene photonic crystals
IMI	insulator metal insulator
LoD	limit of detection
LSPR	localize surface plasmon resonance

PBS	phosphate buffer saline
PGB	photonic band gap
PML	perfectly matched layers
RIU	refractive index unit
SPR	surface plasmon resonance
TM	transverse magnetic
TE	transverse electric
TMM	transfer matrix method

Symbols

c	speed of light in vacuum
ϵ_0	dielectric constant/permittivity
k_0	wave-vector in free space
k_{SP}	wave-vector of surface plasmon
$\Delta\vartheta_r$	change of resonance angle
μ_{eff}	effective permeability
ω	angular frequency
λ	wavelength
\hbar	reduced Planck's constant
E_f	Fermi energy
E_p	photon energy
v_f	Fermi velocity
V_g	gate voltage
σ	graphene conductivity
τ	carrier relaxation time
n_g	graphene electron density
μ_g	graphene electron mobility
ϵ_g	graphene permittivity
k_B	Boltzmann constant
φ	polarization angle
r_p	reflection coefficient of TM-polarized incident light

List of Publications

Publications from Thesis

1. **Md. Mahbub Hossain**, and Muhammad Anisuzzaman Talukder, "Optical magnetism in surface plasmon resonance–based sensors for enhanced performance." *Plasmonics* 16, no. 2 (2021): 581-588.
2. **Md. Mahbub Hossain**, and Muhammad Anisuzzaman Talukder, "Gate-controlled graphene surface plasmon resonance glucose sensor." *Optics Communications* 493 (2021): 126994.
3. **Md. Mahbub Hossain**, and Muhammad Anisuzzaman Talukder, "Graphene surface plasmon sensor for ultra low-level SARS-CoV-2 detection." Accepted in *Plos One* (revision required).
4. **Md. Mahbub Hossain**, and Muhammad Anisuzzaman Talukder, "Graphene nano-strips based transverse magnetic mode dual-channel refractive index sensor." in preparation.
5. **Md. Mahbub Hossain**, and Muhammad Anisuzzaman Talukder, "Anisotropic graphene-photonic-crystals based Tamm and surface plasmons hybrid mode for hemoglobin detection." in preparation.

CHAPTER 1

INTRODUCTION

Biosensors are exceptional devices used for bio-analysis, altering a biological effect into a measurable signal. Biosensors must be extremely precise, free of physical parameters such as pH and temperature, and should be reusable [1]. Different technological advancements have made biosensors reliable in the last few decades. Functionally, biosensors require two essential parts: a bio recognition element (BRE) and a transducer [2]. A biosensor is expected to produce fast, precise, and reliable information from the sensing element. Biosensors must be able to respond continuously and not alter the sensing elements' properties. Nowadays, biosensors play an important role in disease detection, security, food safety, telemedicine, agriculture, bio-processing, environmental and industrial pollution detection, etc. [3].

The classification of biosensors depends on either transducer or BRE, as shown in Fig. 1.1. A BRE is a bio-molecule immobilized on the sensor surface to detect sensing elements. BRE can be classified into five primary types: nucleic acid (DNA/RNA), enzyme, cell, antibody/antigen, or bio-mimetic (micro-organism), which is usually attached to the transducer by a covalent bond. On the other hand, transducer-based

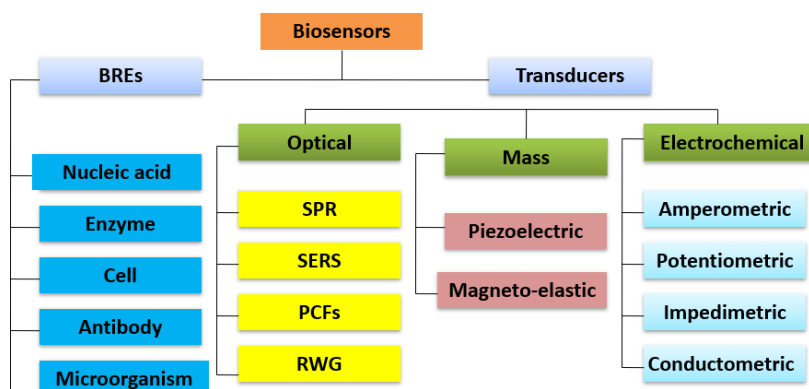


Figure 1.1: Classification of biosensors.

biosensors can be classified into three main areas such as electrochemical (amperometric, potentiometric, conductometric, impedimetric), optical (fluorescence, luminescence, interferometric), and mass change (magnetic-elastic, piezoelectric/acoustic). Though electrochemical biosensors have shown several advantages, it suffers limited temperature range, low sensitivity, poor response time, and requirements of a reference electrode. In contrast, mass-based biosensors use magneto-elastic materials and expose to the magnetic field, such as quartz crystal microbalance. However, mass-based biosensors have a complex structure, need bulky equipment, and are expensive.

On the other hand, optical biosensors are compact analytic devices that create a signal proportional to the absorption of a target bio-molecule [4]. Optical biosensors are biomolecules dominant detection systems which have enormous purposes in biomedical research, disease detection, health care, pharmaceuticals, water pollution detection, and the food industry. Optical biosensors show various advantages such as electromagnetic immunity, electrical isolation, distributed configuration, compact and lightweight, multi-analyte response, high sensitivity and figure-of-merit (FoM), no reference electrode, and fast response time. Moreover, optical biosensors can be either label-free or fluorescent labeled, depending on the detection protocol. In fluorescence-based biosensors, the target bio-molecules attach with tags like dyes. However, fluorescence-based detection is time-consuming due to sample preparation.

In label-free optical biosensing, the target bio-molecule is not distorted and recognized in its regular shape and size. This kind of detection is comparatively simple to achieve a kinetic and quantitative analysis of bio-molecular interaction.

There are enormous variations of optical biosensors based on their construction, such as optical waveguide interferometry, evanescent wave fluorescence, and surface plasmon resonance (SPR). These biosensors use an evanescent field on the surface to detect the interaction of BREs with the target bio-molecules [4]. In evanescent wave fluorescence biosensors, the fluorescent bio-molecules very close to the surface are excited. Although evanescent wave fluorescence biosensors are sensitive, rapid, and highly selective, these biosensors do not support a low limit of detection [5].

Optical waveguide interferometry biosensors combine measurement of phase difference, and evanescent wave for bio-molecule detection [6]. This excellent method is widely known as resonant waveguide gratings (RWG), suitable for detecting avian influenza virus [7]. However, these types of biosensors suffer low sensitivity and small penetration depth. Surface-enhanced Raman scattered (SERS) is another type of optical biosensor generally famous for selective cancer protein detection. However, their application is limited due to low sensitivity, and detection limit [8]. Various photonic-crystal-fibers (PCFs) based plasmonic biosensors are available nowadays, showing high wavelength and amplitude sensitivity [9]. Nevertheless, fabrication of PCFs based biosensors is difficult due to its complex geometry.

Surface plasmon polaritons (SPs) are mainly light waves engrossed on the surface due to the collective free electrons oscillation in the metal [10]. SPs are one of the best leading techniques in the recent biosensing industry, primarily proposed by Liedberg in 1982 [11]. Kretschmann and Rather demonstrated attenuated total reflectance (ATR) technique where the excitation of SPs depends on the drop of reflected light intensity (R) of the reflectivity spectrum [12]. Various research

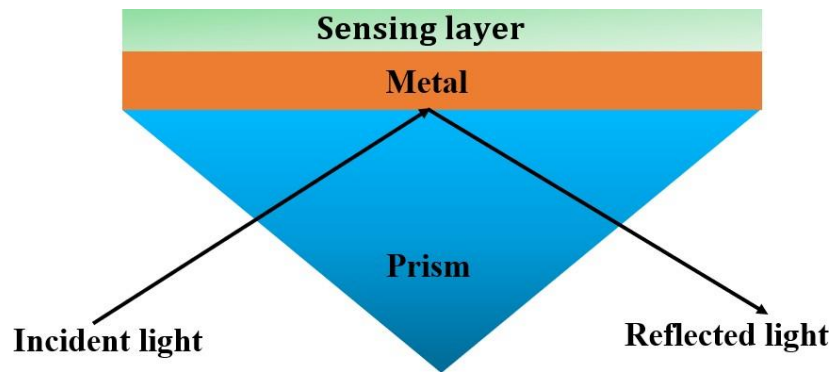


Figure 1.2: Basic Kretschmann configuration for creation of SPR.

groups have been devoted to proposing the excitement of SPs using diverse models. SPR-based sensors have shown significant attention in biological and chemical sensing with precise measurement accuracy, high sensitivity, and low detection limit. Moreover, SPR biosensing supports many applications like food safety, soil and environment monitoring, toxin detection, medical diagnostics, critical pathogen detection, solar cell, and drug screening.

Prism coupling-based Kretschmann configuration is widely used in SPR biosensors, as shown in Fig. 1.2. [12]. Typically, a thin metal layer is placed on top of a prism layer, and the other side of the metal layer is attached to the sensing layer. A transverse magnetic (TM) or p -polarized light is projected to the metal layer from the prism side. Therefore, SPs excite between metal and sensing layer interface. The resonance arises when the wave vector of SPs is the same as the wave vector of incident light. As a result, maximum power is transferred to the SPs. In angular interrogation method, the R is detected with respect of incident angle (ϑ_i). When the R value is minimum at a specific incident angle, it is recognized as the resonance angle (ϑ_r). The absorption of incident light in SPs is the main critical property, enabling sub-wavelength control of light [13]. On the other hand, the damping of electron oscillations in metal is another fundamental problem of SPs, which significantly widens the R -spectrum [14]. As a result, the losses of metal increase. This problem is more severe in the visible wavelength range. Therefore, SPR

biosensors must have low losses to increase the detection accuracy [15]. It is noted that the nature of the R -spectrum reveals the performance of an SPR biosensor. A high-performance biosensor must show large \mathcal{D}_r shifts and narrow R -spectrum.

Fundamentally, different dielectric materials show poor magnetic response, particularly in the visible wavelength region [16]. Also, insulator-metal-insulator based planar multi-layer configurations present comparatively nonmagnetic performance or a low magnetic response (μ_{eff}) [17, 18]. Though, metal-insulator-metal based configurations show magnetic responses through Fano resonances [19]. However, this structure is not promising for biosensing due to the creation of destructive interference by anti-phase dipole oscillations. Moreover, a split ring resonator (U-shaped) was proposed for improved magnetization, which shows the possibility of biosensing [20]. Nevertheless, the proposed structure is complex and could be limited due to the fabrication difficulty.

To achieve the maximum sensitivity with the purpose of detection, SPR-based sensors have been suggested where bio-molecules' weight and concentration are less than 8 kDa and 1 pM, respectively [21, 22]. Sensitivity can be increased using different configurations, such as metal grating and nano-structuring of different dielectric materials, which make the structures more complex. Thus, the R -the spectrum is widened due to the increase of the full width half maximum (FWHM). Consequently, FoM decreases, a critical performance parameter of an SPR biosensor [23]. SPR-based Kretschmann structures are a promising option for biosensing; though these biosensors generally show poor magnetic response, their magnetic properties have never been applied.

Varying metallic and dielectric layers properties are broadly branded as meta-material, which have been explored meticulously in the past because of their dielectric response [17]. To determine the dielectric properties of meta-material especially μ_{eff} , there are number of methods available [24–27]. However, these methods were not appropriate

for complex shaped and practical validation. Chen et al. showed different constitutive parameters of bi-anisotropic meta-material through scattering (S)-parameters for diverse wave polarization [28]. Likewise, Li et al. suggested a non-iterative technique by backward and forward transmission and reflection of S -parameters [29]. Besides, Kildishev proposed recovery of electromagnetic parameters of bi-anisotropic meta-material [30]. Using S -parameters to extract the effective constitutive parameters express all sides of the advantages of numeric and experimental measurement [31].

Usually, silver (Ag) is shown a narrow R -profile of SPR than gold (Au) which confirms enhanced sensor performances [32]. However, Ag is identified as unprotected from oxidation. Therefore, the sensor performances are decreased because the oxide layer creates the R -spectrum broader [33]. Different mechanisms have been used to reduce Ag oxidation, for example, a bimetallic Ag-Au layer or Ag is covered by a thin oxide layer as zinc-oxide (ZnO) or indium-tin-oxide (ITO) [34]. Unfortunately, these mechanisms are not perfect for reducing Ag oxidation. To circumvent the oxidation of Ag in SPR biosensors, the credible material would be graphene which has many unique properties. The particular band diagram of graphene offers a boundless research interest at present in biosensing [35].

Graphene monolayer thickness is 0.34 nm, where sp^2 carbon atoms are organized in a honeycomb lattice. Graphene offers high-level adsorption of bio-molecules as it has rich $\pi - \pi$ conjugation construction and large surface area. As a result, graphene is a suitable dielectric layer for SPR biosensing. Among the different properties of graphene, its two-dimensional (2-D) complex optical conductivity (σ) investigations in different parts of the electromagnetic spectrum are vital. In addition, σ depends on wavelength, temperature, relaxation time, and chemical potential. Also, chemical potential depends on carrier density and can change through gate voltage (V_g), chemical doping, and electric or magnetic field [36].

Last several years, diverse methods have been proposed to determine the σ of

graphene. Gusynin et al. proposed frequency-based σ by Kubo formula [37]. Wunsch et al. established polarization-based approaches to analyze the σ of graphene by the Dirac cone approximation [38]. However, this technique uses fixed chemical potential and random radian frequency separately. Stauber et al. proposed a method that depends on the Kubo formula to compute the σ of graphene through full density-of-states [39]. Nevertheless, the Dirac cone approximation is relatively tiny in the optical wavelength range. Moreover, Bruna et al. proposed an easy method to calculate the refractive index of graphene [40]. This model only uses wavelength for refractive index calculation. Consequently, the effects of temperature, relaxation time, or chemical potential are not used in the analysis. By contrast, monolayer graphene Fermi energy (E_f) can be changed through a V_g [41], which can be used to enhance the incident light absorption and then enhance the sensor performance such as the sensitivity and FoM of an SPR biosensor.

Nowadays, Diabetic is a common disease and vital health-related problem all over the world, especially in middle and low-income countries. Precise detection of blood sugar level (BSL) is critical because incorrect detection of BSL affects the therapy of diabetes patients. Naturally, the BSL detection devices have been registered as glucometers. Glucometers are mainly two types: reflection photometry or electrochemical [42]. Glucometers can have a maximum variation of measurement error of about $\sim 15\%$ from the real BSL at 95% times, conferring to supervisory authorities [43]. However, $\sim 15\%$ nonconformity of the test results of glucometers must be unexpected, particularly when a person's condition is serious in BSL who desires fast and proper medicine. Besides, the electrochemical glucometers use chemical enzymes in the strips sensitive to environmental conditions such as humidity and temperature.

The SPR-based biosensor has been proposed to detect BSL, which shows high measurement accuracy and resolution [44]. However, an Au-coated SPR glucose sensor detects chemical noise in the detection process and suffers poor absorption of the incident light. Most recently, an Au-coronium SPR sensor revealed a decent sensitivity in BSL detection [45], though it shows measurement inaccuracy for the

detection of the BSL. To enhance the sensitivity of the SPR sensors, some research groups have suggested graphene layers as a 2-D material [21, 46, 47]. Moreover, the graphene monolayer has a limited band-gap in the visible wavelength and engrosses only $\sim 2.3\%$ of the incident light [48].

Monolayer graphene's weak absorption can seriously limit its application [49]. To enhance the performance of an SPR biosensor, some research groups have suggested using multi-layer graphene on an SPR biosensor [50, 51]. Nevertheless, graphene multi-layers create extra damping in SPs because the imaginary value of the refractive index of graphene is large. Also, using multi-layer graphene broadens the R -spectrum, and hence detection accuracy is decreased [52]. Various models have been proposed to increase the light-graphene interaction, like graphene photonic crystals (GPCs). To make a GPCs structure, various stacked layers of graphene monolayer are separated by dielectrics, and these types of structures have been explored in both theory, and experiment [53, 54]. Graphene monolayer in GPCs can enhance the photon absorption by Bragg fluctuation as well as enhances the light-graphene interaction [49]. GPCs are very suitable for a vast sense area due to fast response time and ultrahigh sensitivity [55]. Also, the electromagnetic waves propagation in GPCs can be controlled by photonic band gap (PGB) [56]. SPs can be excited in GPCs though the SPs mode is scattered, which can be controlled by doping [57]. It is motivating to note that GPCs show properties of meta-materials like Tamm plasmon polaritons (TPs), critical coupling, and negative refraction [58–60].

TPs are principally surface mode that excites the metal and distribute the Bragg reflector (DBR) interface [61]. TPs are stimulated by TM or transverse electric (TE) polarized light, and there is no need for dispersion regulation like SPs [62]. Also, the R -spectrum of TPs is narrower than SPs [63]. When a noble metal layer is deposited on a prism and PCs are used, a hybrid TPs-SPs mode is excited [64]. However, these hybrid modes are excited on interfaces like TPs on the metal and GPCs and SPs on the metal and sensing layer interfaces. As a result, an anti-crossing effect is observed on their dispersion relation [64]. The anti-crossing effect alters

the dispersion properties of the hybrid TPs-SPs plasmonic mode and decreases the absorption losses of SPR. Therefore, the R -spectrum becomes narrower compared to traditional SPR.

Recently, TPs-based refractive index and temperature sensors proposed by different research groups [63, 65, 66]. Moreover, graphene-porous silicon PCs demonstrated that FoM and sensitivity are controlled by varying parameters like incident angles, porosity, and silicon layers [67]. Also, asymmetric graphene-DBR was used to create TPs mode, and the effect of TM-polarization or TE-polarization on sensor performances was investigated [68]. Additionally, a refractive index sensor contains GPCs proposed with defect layer [63]. However, the proposed refractive index sensor is polarization and phase insensitive. Alternatively, a terahertz (THz) refractive index sensor of graphene-DBR was proposed where sensor performances are phase and polarization-dependent [69]. In references, [63, 67–69] both of these types of sensors operated in the THz region. However, using THz frequency has some limitations, such as difficulty detecting the complex molecules due to non-ionizing behavior and low photonic energy radiation [70, 71].

Hemoglobin (Hb) is an essential part of blood in red blood cells (RBC). The oxygen supplies in the tissues depend on Hb levels, and variations of Hb levels cause various diseases [72, 73]. The blood refractive index changes every 0.001 refractive index unit (RIU) for 6.1025 g/L Hb level. Determine Hb level from RBC, heparin-based method widely applied where pre-processing is essential [74]. However, heparin-based determination suffers measurement error. A whispering gallery-based method was proposed to detect the Hb level. Nevertheless, the sensitivity of this sensor is low [75]. Recently, a graphene-based SPR sensor has been proposed for Hb detection [74]. Nonetheless, there is no information on detection accuracy, and sensitivity fluctuates when the Hb level increases.

Recently, severe-acute-respiratory-syndrome coronavirus 2 (SARS-CoV-2) is a dangerous biological pathogen responsible for coronavirus disease 2019 (COVID-19).

COVID-19 has triggered an unprecedented health problem worldwide due to the high death rate. Several research groups have proposed to detect SARS-CoV-2 in real-time with high efficiency [76–82]. The reverse transcriptase quantitative polymerase chain reaction (RT-qPCR) technique is branded as the gold standard for sensing several critical viruses, such as SARS-CoV-2, human immunodeficiency virus, and cytomegalovirus [76].

RT-qPCR is highly sensitive and selective for SARS-CoV-2 identification [77]. However, its application is limited due to significant false-negative cases ($\sim 15\%$), long sample processing time, costly instruments, the necessity of skilled human resources, and uninterrupted power supply over a long period [78, 79]. On the contrary, colorimetric-based loop-mediated isothermal amplification (LAMP) techniques are suggested for identifying SARS-CoV-2 to resolve the limitations of an RT-qPCR technique [79]. LAMP techniques show a high nucleic-acid amplification efficiency but are time-consuming and tedious as they use electrophoresis for detection. Also, a chest computer tomography (CT) scan can be used to detect SARS-CoV-2 [81]. However, such a technique cannot be used for asymptomatic patients, early-stage detection, and measuring the mass density of virus [83].

Plasmonics-based optical biosensors have been proposed to detect many life-threatening pathogens, such as dengue virus envelope protein, thyroglobulin, and SARS-CoV-2 [77, 84–88]. A toroidal plasmonic meta-sensor was suggested to detect the SARS-CoV-2 spike (S)-protein using THz wavelength, confirming the detection limit of only ~ 4.2 fM [87]. Nevertheless, the plasmonic meta-sensor suffers from insensitivity to S-protein concentration between 20 fM and 50 fM and low quality factor. Moreover, plasmonic photo-thermal effect and localized SPR (LSPR) have been suggested to detect SARS-CoV-2 by nucleic acid hybridization techniques [78]. However, thermo-plasmonic heat cannot be the difference between two similar gene sequences, and also this sensor shows low detection accuracy. Furthermore, a plasmonic sensor has been proposed for SARS-CoV-2, S-protein detection by a phase interrogation technique

[77]. Nevertheless, its performance is imperfect due to the complex measurement techniques required for phase variation.

TM surface waves propagate at the interface between the dielectric and metal in SPR-based biosensors. Such SPR biosensors show a wider R -spectrum due to the scatter and absorption losses in the noble metal [89]. As a result, the metal-based optical biosensor is limited to further development. As an alternative, graphene can be used instead of noble metal. However, the absorption of monolayer graphene is 2.3%, which is good enough for a 0.34 nm thickness layer. Nevertheless, achieving a competent light-matter interaction this absorption is not sufficient for optical sensing [90]. As a substitute, an increasing number of graphene layers on the metal surface enhanced the sensitivity of an SPR sensor. However, increasing the number of graphene layers widen the FWHM of the R -profile [91]. On the other hand, graphene plasmons (GPs) have shown adjustable electromagnetic properties, comparatively low loss, and intense light absorption [92]. As a result, GPs have shown more research interest in different areas of photonics and plasmonics devices from mid-infrared (MIR) to THz wavelength region [93, 94].

When $\hbar\omega < 1.667 \times E_f$, graphene shows metallic response with positive imaginary part of σ that supports TM mode in graphene or GPs ensuring high light confinement [95]. However, TM mode in graphene can reach up to MIR range whereas TE up to visible range [96]. TM modes in graphene have been observed experimentally in graphene micro-ribbon arrays, infrared nano-imaging, nanoscopy, and sub-wavelength gratings from THz to infrared wavelength range [97–99]. Kretschmann-based angular interrogation method is usually used to excite the SPs. The ϑ_r shifting property must be high to enhance the sensor performance. Therefore, a Kretschmann-based sensor arrangement's sensitivity is low, around 200 degree/RIU [100]. It is possible to increase the sensitivity by reducing the refractive index of the prism material. However, this method reduces the detection accuracy [100].

To mitigate this problem, some research groups have proposed various Kretschmann-modified structures. Such as metal nano-grooves plasmonic sensor developed where slit widths vary to decrease the reflected light intensity [101]. However, this sensor depends on geometric limitations like space of nano-line, periodicity of nano-line, and the height of the nano-lines in the nano-grating. Moreover, Kretschmann-based nano-cavities in the metal have been proposed for robust field enhancement [102]. Nonetheless, this method requires precise control of resonance. Furthermore, nano-prism-based Kretschmann configuration has projected at normal incidence for sensing [103]. Though this technique presents good sensitivity, its detection accuracy is poor due to increased interface volume as SPs spread deeper inside the sensing medium.

The primary intention of this research work offered in this thesis is to determine a novel method to enhance sensor performances using the properties of graphene in SPR sensors. We will show the findings by theoretical and computational analysis, establishing the observation's feasibility. First, we propose an SPR-based sensor that will create magnetism in visible wavelength and will be used to detect sensing elements when replacing the conventional R -profiles. We will propose a monolayer graphene optical property that can be controlled by applying suitable V_g that essentially increases the sensor performances. In this thesis, we will discuss the GPCs-based TPs and SPs hybrid mode for Hb detection, where an anti-crossing effect is observed between TPs and SPs. Moreover, we aim to detect critical biological pathogens, such as SARS-CoV-2, S-protein concentration where graphene layers are functionalized with angiotensin converting enzyme 2 (ACE2) antibodies will help efficient adsorption of the SARS-CoV-2, S-protein. Lastly, we will describe the graphene TM mode that can be created in the visible spectrum by applying a suitable V_g and appropriate thickness of ZnO. As a result, there is no necessity to use noble metals in SPR biosensing.

The rest of the thesis is prepared as follows:

Chapter 2 presents a Kretschmann configuration-based SPR sensor that can make a robust magnetic response in the visible wavelength region in the presence of a sensing element. Therefore, this structure's magnetic response can enhance the sensor performance. We use the analytical model to determine the μ_{eff} and R by S -parameters retrieval method. We also discuss the sensor structure and simulation approaches. In addition, a possible experimental setup of the proposed detection technique is discussed. We present the FoM of the proposed technique using the magnetic resonance increases expressively compared to the conventional techniques used in an SPR-based sensor.

Chapter 3 proposes an SPR glucose sensor where a V_g controls the optical property of graphene. We change the monolayer graphene E_f by using a suitable V_g to increase the absorption of the incident light and, thus, increase the sensitivity and FoM of the proposed sensor. We define the theoretical models to determine the optical properties of monolayer graphene and the sensor performance when V_g is present. We discuss the simulation methods that we followed to solve the Maxwell equations by finite difference time domain (FDTD) method. We calculate and describe the sensor performances and precision of BSL detection for different V_g . We also describe the detection accuracy by using the linear regression model. Furthermore, we investigate the effect of temperature on the proposed sensor and BSL.

Chapter 4 describes the accurate detection of ultra low-level SARS-CoV-2, S-protein concentration. We propose a sensor exposing graphene SP to detect the SARS-CoV-2, S-protein. The graphene layer is functionalized with ACE2 antibodies, which can help effective adsorption of the SARS-CoV-2, S-protein. We illustrate and discuss the proposed sensor arrangement and optimize the layer thicknesses. Then, we present the optical properties of different materials, theoretical analysis of sensor performance parameters, and simulation methods. We also present and discuss the SARS-CoV-2, S-protein detection approach by the change of ϑ_r , analysis of the binding between ACE2 and S-protein, and the calculated sensor performances.

We use the Langmuir model to determine the binding kinetics between ACE2 and S-protein and compute the equilibrium dissociation constant.

Chapter 5 describes the GPCs-based TP and SP hybrid mode for Hb level detection. We use the in-plane anisotropic property of GPCs; the proposed sensor represents polarization-dependent performances. We optimize the Ag thickness and number of a unit cell of GPCs based on R minimum and FWHM. Also, the energy exchanges between TP and SP modes are determined by Fourier mode spectral analysis (FMSA). We also present the anti-crossing effect between TP and SP for different polarization angles applying transfer matrix method (TMM). Furthermore, Barer theoretical model is used to determine Hb's optical properties in the blood. The sensor performances, especially the change of ϑ_r and FWHM for both the TP mode and SP mode, are calculated using the TMM-based angular interrogation method. Additionally, double dips method (DDM) is used to compute the sensitivity and FoM.

Chapter 6 presents graphene TM mode created in the visible spectrum by applying a suitable V_g and appropriate thickness of ZnO. We propose a dual-channel graphene TM mode-based refractive index sensor, a promising alternative to the traditional Kretschmann arrangement. We apply the Kubo formula to determine graphene conductivity and, more particularly, permittivity. We modify the conventional Kretschmann arrangement and set dual channels for refractive index sensing. We also use graphene nanostrips in the first graphene layer, which scatter the incoming light to the next graphene layer. For sensor performance calculation, we use the TMM-based technique.

Chapter 7 summarizes the findings and concludes.

CHAPTER 2

OPTICAL MAGNETISM IN SPR-BASED SENSOR FOR ENHANCED PERFORMANCES

Surface plasmon resonance (SPR) based structures are finding important applications in sensing biological as well as inorganic samples. In SPR techniques, an angle-resolved reflection (R) profile of the incident light from a metal-dielectric interface is measured and the resonance characteristics are extracted for the identification of the target sample. However, the performance, and hence, the applicability of these structures suffers when the weight and concentration of the target samples are small. Here, we show that SPR based sensors can create strong magnetism at optical frequency, which can be used for the detection of target samples instead of using the conventional R profiles, as the magnetic resonance varies depending on the refractive index of the target sample. Using scattering parameters retrieval method, we computationally find out the effective permeability (μ_{eff}) of a SPR sensor with a structure based on Kretschmann configuration, and use it to calculate the performance of the sensor. A comparison with the conventional technique that

uses R profile to detect a target sample shows a significant increase in the sensor performance when μ_{eff} is used instead.

2.1 Introduction

In the last few years, nano-structures have been studied and developed for magnetic responses. In particular, enhancing magnetic responses of dielectric layered structures at visible wavelength range has drawn significant interest due to their promising applications in sensors and exploitation of the non-linear properties that they offer [104–106]. Naturally, the magnetic response of most dielectric materials is weak, especially in the optical frequency range [16]. Additionally, planar multi-layer dielectric structures also show a relatively non-magnetic behavior with a very small magnetic permeability (μ_{eff}) [17, 18, 107]. However, multi-layer dielectric structures are promising in enhancing μ_{eff} due to their immense capability of being engineered in geometry and layer thicknesses. Recently, significant magnetic responses have been shown in metal-insulator-metal structures by exciting Fano resonances and in planar dielectric-metal multi-layer structures, where dielectric layers are isolated by air and silver layers [19]. Although the significant magnetism obtained from these structures makes these structures promising for sensing applications, they are not favorable for sensing due to creating multiple Fano resonances through anti-phase dipole oscillations, and hence, forming destructive interference, and also due to the complexity in the structures. A U-shaped split ring resonator designed by metal-dielectric multi-layer structure has also been proposed for enhanced magnetization, which has potential for sensing applications as well [20]. However, applications of these structures could be limited due to the complexity in the fabrication of the practical devices.

The property of evanescent electromagnetic fields of surface plasmon polaritons (SPPs) in a planar metal-dielectric structure is used in many sensing techniques.

However, the applications of surface plasmon resonance (SPR) based sensors become limited while detecting small molecular weight (<8 kDa) and low concentration (<1 pM) analytes, which is often the case for several critical biological samples [108]. Recently, several SPR sensors have been proposed that show hyper sensitivity (S) so that molecules with less than 8 kDa weight and 1 pM concentration can be detected [21, 22, 109]. Although S is increased in the hyper sensitive structures by making the structures complex, e.g., by adding additional layers, the angle-resolved reflectivity (R) profile is significantly broadened. The increase of full-width at half-maximum (FWHM) of the R profile causes the figure-of-merit (FoM) of the structure to decrease, which is the most critical performance parameter for such SPR sensors [23]. Additionally, several hybrid SPR sensors [48, 110] and SPR sensors with additional complexity by including black phosphorus, metamaterials, silicon, and MoS₂ nano-structures have shown to enhance S and FoM [111–114]. Recently, the addition of graphene and BaTiO₃ layers in SPR sensor has shown that the resonance angle can be shifted significantly with a small change of refractive index of the target sample [46]. Caballero *et al.* proposed magneto-optical SPR sensor, where the detection is based on the calculations of the transverse magneto optical Kerr effect [115]. However, these hybrid SPR sensors often include complex arrangements of nano-structures, and need complicated and expensive manufacturing techniques.

SPR sensors based on Kretschmann configuration are the best choice for many sensing applications because of their simple structural arrangements. In SPR sensors, the presence of a biomolecule or any other target molecule in the sensing layer changes the SPR electromagnetic fields. The plasmonic characteristics and applications of SPR sensors have been explored well. However, SPR sensors usually show weak magnetic property and their magnetic properties have never been used for sensing. Optical magnetism in the optical frequency range using insulator metal insulator (IMI) Kretschmann plasmonic structure has not been explored till now. Similar to SPR resonances, strong magnetic resonances, also known as magnetic plasmons, can be excited in a multi-layer structure [116]. The concept is based on

designing IMI planar multi-layer structures that support localized surface plasmons (LSPs), which act as magnetic dipoles and thus create strong optical magnetism. Thus, the enhanced localization of light by LSPs increases the magnetic response of the IMI planar multi-layer structure [117].

In this chapter, we show that a SPR sensor based on Kretschmann configuration can create strong magnetic response in optical frequency range in the presence of a target sample, and thus, magnetic property of these structures can be used to increase the performance in sensing the target sample. Using finite difference time domain (FDTD) simulations and scattering parameters (S -parameters) retrieval method, we calculate angle-resolved μ_{eff} and R profiles of a SPR sensor that has a structure based on Kretschmann configuration. We show that the FoM of the sensor based on the magnetic resonance increases significantly compared to that of a conventional purely SPR based sensor. Exploitation of the magnetic property of the simple Kretschmann configuration has the potential of obviating the need of a much more complex sensor structure while achieving high sensor performance.

The rest of the chapter is organized as follows: In Sec. 2.2, we describe the theoretical models that we used to calculate μ_{eff} and R using S -parameters retrieval method. In Sec. 2.3, we discuss the Kretschmann configuration based SPR sensor structure investigated in this chapter and the FDTD simulation approach. In Sec. 2.4, we discuss the possibility of the experimental setup of the Kretschmann configuration based SPR sensor. In Sec. 2.5, we present and discuss the calculated magnetic response of the sensor, and also the S and the FoM of the sensor calculated from μ_{eff} and R profiles. In Sec. 2.6, we draw conclusions on the findings.

2.2 Theoretical Modeling

The electromagnetic response of a structure with a complex μ_{eff} can be determined through systematic Drude-Lorentz representation [118] or S -parameters retrieval

techniques [119–122]. Often, the Drude-Lorentz analytical model is not precise, especially, if the structure is a planar multi-layer. Alternatively, the S -parameters retrieval technique depends on the reflection (S_{11}) and transmission (S_{21}) coefficients assuming a real index of the medium, and gives more precise results for μ_{eff} [119]. The coefficients S_{11} and S_{21} are computed from amplitude and phase of the peak fields as recorded on the detection planes. The S -parameters retrieval technique assumes that the detection planes are far away from the metal-sample layer interface so that the fields can be assumed to be propagating like a plane wave. Practically, the distance of the detection plane for the reflected waves from the metal-sample layer interface and the distance of the detection plane for the transmitted waves from the metal-sample layer interface must be much greater than the wavelength of the incident light. It is also essential to recompense for the phase that gathers as the fields spread through the background medium from the source to the multi-layer structure, and from the multi-layer structure to the detection planes. Thus, using the S -parameters retrieval technique, μ_{eff} can be calculated by the following equations [119]

$$S_{11} = \frac{i}{2} \frac{1}{z} - z \sin(n_{\text{eff}} k_0 z), \quad (2.1a)$$

$$S_{21} = \frac{1}{\cos(n_{\text{eff}} k_0 d) - \frac{i}{2} (z + \frac{1}{z}) \sin(n_{\text{eff}} k_0 d)}, \quad (2.1b)$$

$$n_{\text{eff}} = \frac{1}{k_0 d} \cos^{-1} \frac{1}{2S_{21}} (1 - S_{11}^2 + S_{21}^2), \quad (2.1c)$$

$$z = \pm \frac{\sqrt{(1 + S_{11})^2 - S_{21}^2}}{(1 - S_{11})^2 - S_{21}^2}, \quad (2.1d)$$

$$\epsilon_{\text{eff}} = \frac{n_{\text{eff}}}{z}, \quad (2.1e)$$

$$\mu_{\text{eff}} = n_{\text{eff}} z, \quad (2.1f)$$

where n_{eff} is the effective refractive index, ϵ_{eff} is the effective permittivity, z is the normalized impedance, d is the total thickness of the multi-layer structure, i.e., the sum of the thicknesses of the different layers, and $k_0 = 2\pi/\lambda$, where λ is the

wavelength of the incident light. To determine the effective constitutive parameters precisely, we follow the condition $k_0 d < 1$ as $d < \lambda$ [119]. The reflectivity R can be determined using S -parameters retrieval method as

$$R = |r_p|^2, \quad (2.2)$$

where r_p is the reflection coefficient for p-polarized incident light.

We will show that μ_{eff} of the multi-layer structure at resonance can be used to detect a target sample instead of using R at resonance. Practically, μ_{eff} can be precisely measured by several off-the-shelf devices, such as by a Ferromaster, which is a handy instrument capable of measuring μ_{eff} precisely [123]. The magnetic resonance angle is identified as the angle at which μ_{eff} reaches maximum while varying the incidence angle of light. The S of the multi-layer structure can be calculated as a change in the incidence angle for per unit change in the refractive index (n_s) of the sample, where the change in the angle can be due to the resonance for μ_{eff} as proposed in this work or conventional SPR excitation. The FoM depends inversely on the broadening or the FWHM of the response profiles. Thus, we can write the S and FoM considering μ_{eff} or R at resonance as

$$S_{\mu,R} = \frac{\Delta\vartheta_{\mu,R}}{\Delta n_s}, \quad (2.3)$$

$$\text{FoM}_{\mu,R} = \frac{S_{\mu,R}}{\text{FWHM}}, \quad (2.4)$$

where $\Delta\vartheta$ and Δn_s are the changes in the incidence angles and the refractive index of the target sample, respectively. The subscripts μ and R represent whether the change in the angle is due to magnetic resonance or SPR, respectively.

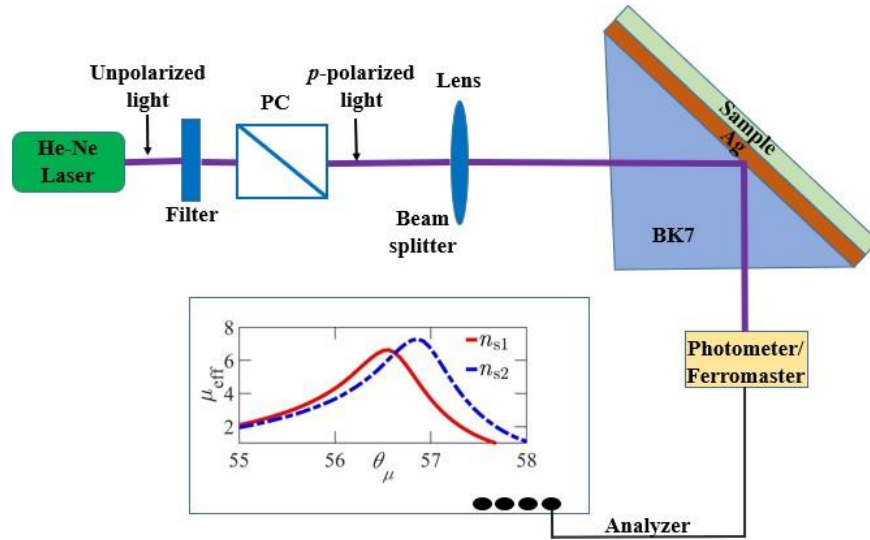


Figure 2.1: Schematic illustration of a feasible experimental setup for the proposed technique of the Kretschmann configuration based SPR sensor.

2.3 Sensor Structure and Simulation Setup

The SPR Kretschmann configuration sensor structure consists of three different layers, as schematically shown in Fig. 2.1. The first layer is a semi-infinite prism of glass material BK7. The exciting light is incident on the metal layer through the semi-infinite prism and also the reflected light is collected from the semi-infinite prism. The second layer is metal (Ag), which has a thickness of 45 nm. The third layer is the sample layer, which has a thickness of 50 nm. We assume that the incident light has a wavelength of 633 nm, which is often used in SPR based systems for excitation [124, 125]. The refractive indices of different sensor layers are frequency dependent. The refractive index of BK7 has been calculated using the approach described in Ref. 126 and found to be 1.515 at 633 nm. The refractive index of Ag has been calculated using the Drude-Lorentz model [127].

We take the refractive index of the sample layer as a parameter and vary from 1.3 to 1.9. There are several organic samples with a refractive index in this range. While different proteins and biomarkers have refractive indices in the range of 1.3-1.45 such as thyroglobulin-RI 1.45 and human fibrinogen (Fb) protein molecules-RI 1.39

[85, 128]. However, a lot of films having hopeful properties of sensing/bio-sensing having RI range 1.5 to 1.9 like Benzene (C_6H_6)-RI 1.5, Potassium hydrogen phthalate ($C_8H_5KO_4$)-RI 1.7, air-dried herring DNA-RI 1.685, tetrahydrofuran (THF) clathrate-RI 1.8 and Carbon di-sulfide (CS_2)-RI 1.74 whereas CS_2 are inorganic material [47, 129].

To find out the dynamics of the incident light with the sensor in the presence of the target sample, we carry out two-dimensional full-field FDTD simulations. The simulation domain is $7 \mu\text{m}$ in the direction of the layer interfaces, i.e., in the y -direction, and $8.5 \mu\text{m}$ in the direction perpendicular to the interfaces, i.e., in the x -direction. We use a non-uniform meshing scheme for the computational domain to optimize the computational efficiency and accuracy of FDTD solutions. We use the perfectly matched layer boundary condition at the edges of the simulation domain in the direction perpendicular to the layer interfaces. We use Bloch boundary condition in the direction of the interfaces. The incident light has a transverse magnetic polarization and the incidence angle varies from 54° to 64° . The detection planes for the reflected and transmitted light are at $\sim 7\lambda$ from the metal-sample interface, as shown in Fig. 2.1.

2.4 Feasible Experimental Setup

We discuss the possibility of practical execution of the proposed method. The complete experimental setup for the proposed method is not much dissimilar from that for SPR based Kretschmann configuration. The experimental Kretschmann configuration setup is used in this study to sense the optical magnetism in visible wavelength. The feasible setup of the structure is shown in Fig. 2.1. A He–Ne laser of $<4 \text{ mW}$ at 633 nm is used as the light source. A filter basically neutral-density (ND) is used for modifying the intensity of incident light. Glan-Taylor prism which is the most common types of present polarizing prism used to isolate the p-polarized light

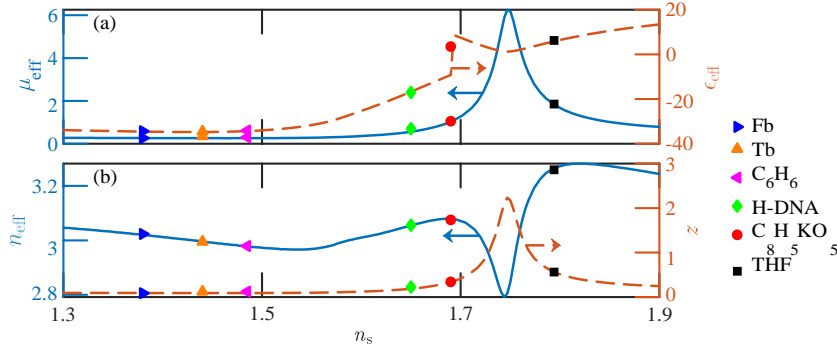


Figure 2.2: Effective constitutive parameters (a) μ_{eff} and ϵ_{eff} , and (b) n_{eff} and z for the Kretschmann based SPR sensor when n_s varying from 1.3 to 1.9.

from the s-polarized light. A convex lens is used so that light rays pass through it becomes closer together and eventually focus on a point other side of the lens. The sensor is associated by index matching gel to the BK7 prism and then place on a rotation stage to change the incidence angle in the ATR condition. The reflected light is recorded by the photometer (measures the intensity of light) and optical magnetism is recorded by Ferromaster. Finally, the reflected light intensity or optical magnetism is analyzed through digital oscilloscope.

2.5 Results and Discussions

Figure 2.2 illustrates μ_{eff} , ϵ_{eff} , n_{eff} , and z of the sensor based on Kretschmann configuration that we study in this work as described in the previous section. We vary the refractive index n_s of the sample layer from 1.3 to 1.9. In Fig. 2.2(a), we find that $\mu_{\text{eff}} < 1$ and $\epsilon_{\text{eff}} < 0$ when $n_s \lesssim 1.69$. Therefore, the sensor structure is non-magnetic when $n_s \lesssim 1.69$. We note that the response of the structure is non-magnetic, i.e., $\mu_{\text{eff}} \leq 1$, when $z \cdot n_{\text{eff}} < 1$, as shown in Fig. 2.2(b) [31]. However, the sensor structure becomes magnetic, i.e., $\mu_{\text{eff}} > 1$, when $n_s > 1.69$. The sensor structure shows a magnetic resonance and μ_{eff} reaches maximum at $n_s \approx 1.75$. At magnetic resonance, n_{eff} is minimum and $z \cdot n_{\text{eff}} > 1$, as shown in Fig. 2.2(b), and therefore, the magnetic field becomes strong to create optical magnetism. Also, we note that the magnetic

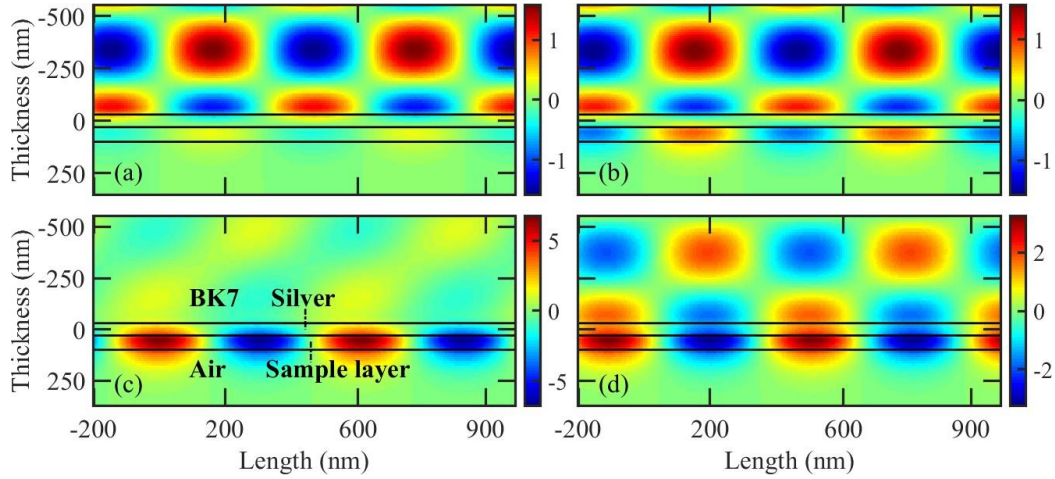


Figure 2.3: Magnetic field profiles polarized in the z -direction for 633 nm incident wavelength when (a) $n_s = 1.30$, (b) $n_s = 1.546$, (c) $n_s = 1.75$ and (d) $n_s = 1.82$.

response of the structure is Lorentzian, which verifies the optical magnetism as has also been observed before for planar multi-layer structures [130, 131].

Dual mode SPPs are excited at the metal-dielectric interface when the structure is non-magnetic, as shown in Figs. 2.3(a) and 2.3(b). Figs. 2.3(a) and 2.3(b) show magnetic field profiles when $n_s = 1.3$ and $n_s = 1.546$, respectively. When $n_s \approx n_{\text{prism}}$, strong SPPs are excited. However, we find that the response of the conventional multi-layer planar structure based on Kretschmann configuration is non-magnetic when $n_s \lesssim 1.69$, due to the excitation of dual mode SPPs. By contrast, single mode SPPs are excited when $n_s > 1.69$, and as a result, the structure becomes magnetic. In Fig. 2.3(c), we note the excitation of single mode SPPs when $n_s = 1.75$. The excited single mode SPPs at $n_s = 1.75$ are similar to LSPs, and hence, confine the electromagnetic fields more strongly at the metal-sample layer interface. When $n_s = 1.75$, n_{eff} is minimum due to the maximum power confinement in the metal film. When n_s varies from 1.75 to 1.82, strong LSPs are excited as shown in Fig. 2.3(d). For sensing purpose, both SPPs and LSPs are similar from the detection point-of-view. However, the excitation of LSPs support stronger light confinement, and as a result, can enhance the sensor performance, especially, the FoM [132].

We investigate the effective constitutive parameters of conventional Kretschmann based SPR bio-sensor for computing S_{11} and S_{21} coefficients. Variation of sample layer RI has great impact on effective constitutive parameters. Moreover, the different value of effective constitutive parameters depends on SPPs excitation which is shown in Figure 2.3 (a) to 2.3(d). μ_{eff} value is less than 1 in the specific lower sample layer RI, where dual modes SPPs are excited. These dual modes are viewed on each metal dielectric interface as shown in Figure 2.3(a) and 2.3(b). We show that lower sample layer RI range where the dual modes SPPs are excited, the conventional multi-layer planar Kretschmann structure is non-magnetic. As long as, $z.n_{\text{eff}} = 1$ holds, the response of μ_{eff} is totally electric [31]. It was already shown that momentous magnetic response in planar dielectric-metal if the sample layer was contained high RI films which support physically powerful displacement currents at optical wavelengths [19]. LSPs are strongly excited in 1.75 sample layer RI range. In this situation, LSPs power are highest which confirms the incident photon energy is fully transfer to plasmon. Furthermore, the electromagnetic fields of LSPs are more concentrated at the metal surface as shown in Figure 2.3(c) and 2.3(d).

The excited LSPs at the metal-prism and metal-sample layer interfaces of the sensor structure interact with each other through the fields that penetrate into the metal. Magnetic dipoles are created due to anti-phase electric dipole oscillations at the top and bottom of the metal layer. Although the anti-symmetric resonance is also observed when $n_s > 1.80$, the magnetic resonance weakens and μ_{eff} decreases due to interactions among magnetic dipoles, and therefore, due to the phase retardation of the scattered field with respect to the the incident field.

In Fig. 2.4(a), we show μ_{eff} as a function of the incidence angle (ϑ_μ) when $n_s = 1.70$ and 1.71. We note that μ_{eff} has a resonance at $\vartheta_\mu = 56.56^\circ$ and reaches a maximum value of ~ 6.63 when $n_s = 1.70$, whereas, μ_{eff} has a resonance at $\vartheta_\mu = 56.86^\circ$ and reaches a maximum value of ~ 7.29 when $n_s = 1.71$. Fig. 2.4(b) shows R profiles against incidence angles (ϑ_R) of the excitation light when $n_s = 1.70$ and 1.71. The R profiles are commonly used in conventional sensors for the calculation of S and FoM.

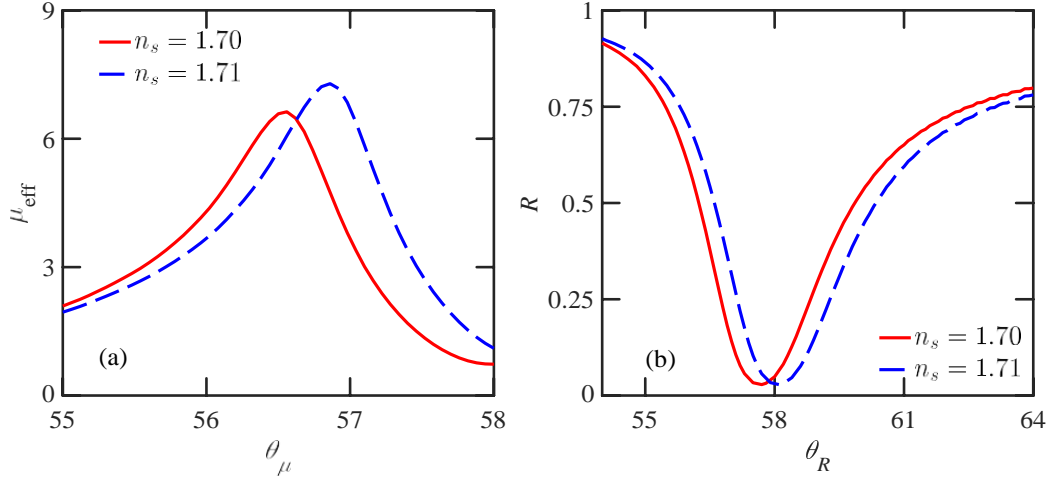


Figure 2.4: (a) μ_{eff} and (b) R as functions of resonant incident angles for $n_s = 1.70$ and 1.71 at 633 nm incident wavelength.

We note that the resonance angles are slightly different for μ_{eff} and R in Figs. 2.4(a) and 2.4(b). This is because when the resonance occurs, the phase between the incident and reflected light alters. S-parameters retrieval method computes μ_{eff} at resonance that depends not only on the multi-layer thicknesses but also on the distance between the source and the metal-sample layer interface, and also on the distance between the metal-sample layer interface and the reflection and transmission profile detection planes. By contrast, the calculation of R profile depends only on the multi-layer thickness.

In this chapter, our proposal is to make use of μ_{eff} properties instead of determining R at resonance. To be specific, we propose to use the μ_{eff} which value and position is changed by varying the sample layer RI. The maximum μ_{eff} at resonance, the S as well as the FoM of magnetic resonance curve is methodically examined by S-parameters retrieval technique at 633 nm incident wavelength. We show that not only the μ_{eff} but also the ϑ_R is changed due to varying the sample layer RI. Moreover, μ_{eff} curve represents narrow line width (FWHM) that is very much sensitive to the variation of RI of sample layer. Hence, we can using this concept for sensing performance parameters calculation and enhancement.

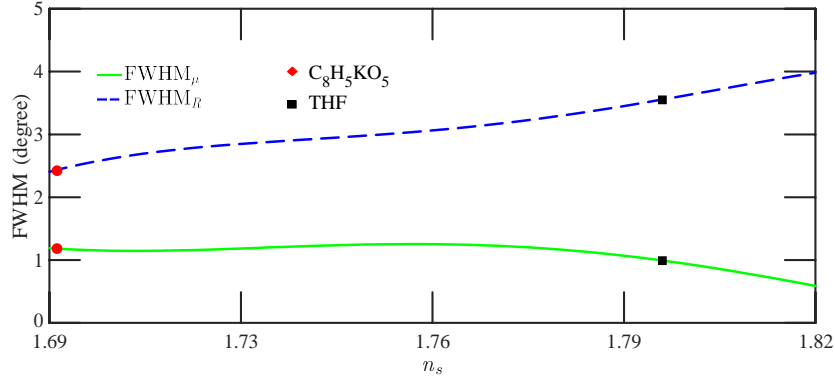


Figure 2.5: Variation of FWHM for μ_{eff} and R profiles, respectively as a function of specific n_s .

The detection accuracy of a SPR sensor is influenced by the FWHM of μ_{eff} or R profiles. A narrow FWHM of the angle-resolved μ_{eff} and R profiles indicates a high signal-to-noise ratio and precision in the measurement of resonance angles [133]. The FWHM of μ_{eff} profiles shown in Fig. 2.4(a) are 1.17° and 1.18° when $n_s = 1.70$ and 1.71 , respectively. On the contrary, the FWHM of R profiles shown in Fig. 2.4(b) are 2.42° and 2.52° when $n_s = 1.70$ and 1.71 , respectively. The increase of FWHM for R from that for μ_{eff} is attributed to the faster damping of SPPs than LSPs. The FWHM values of μ_{eff} and R profiles are plotted in Fig. 2.5 when n_s varies from 1.70 to 1.82. We note that the FWHM for R is more than a factor of two greater than that for μ_{eff} . This is because the confinement of light at SPR is comparatively lower than that at the magnetic resonance. A better confinement supports lower FWHM value. As n_s increases, FWHM for μ_{eff} decreases while that for R increases.

In Fig. 2.6(a), we show the calculated S from both μ_{eff} and R profiles. The calculated S from μ_{eff} profile is smaller than that from R profile. This is due to low angle shifting property of magnetic resonance. The maximum S calculated using μ_{eff} is $30^\circ/\text{RIU}$ when $n_s = 1.75$. When $n_s > 1.75$, S gradually decreases due to the excitation of anti-symmetric LSP modes. As a result, angle shifting property is reduced. On the other hand, the calculated S from R profile is $47^\circ/\text{RIU}$ when $n_s = 1.75$ and $54^\circ/\text{RIU}$ at the peak when $n_s = 1.78$.

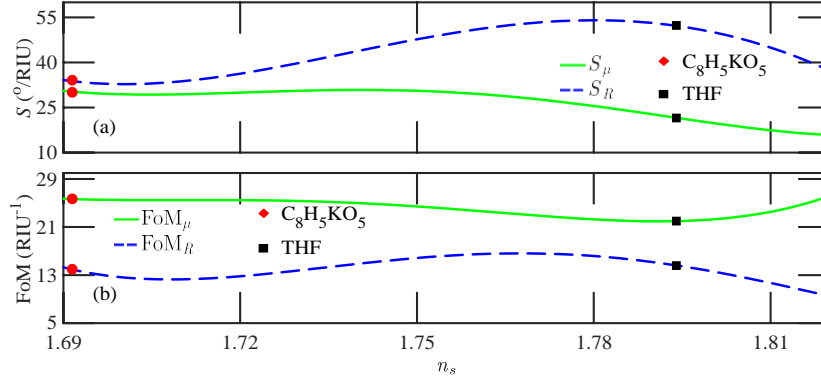


Figure 2.6: Variation of (a) S and (b) FoM against n_s . The subscripts μ and R are used when the parameters are calculated using μ_{eff} and R profiles, respectively.

Table 2.1: Comparison of FoM with previously reported sensors.

Wavelength (nm)	Enhancement strategy	FoM (RIU ⁻¹)	Reference
633	MoS ₂ nano-sheet	3.44	[137]
633	Graphene/Ag/Cr	9.691	[138]
633	MoS ₂ /graphene/MoS ₂	11.15	[21]
633	Au/graphene/MoS ₂	13.13	[139]
630	Au/graphene	14.16	[140]
632	ZiO/Au/MoS ₂ /graphene	15.11	[48]
653	Au/KCL	16.5	[141]
633	This work (using R)	16	
633	This work (using μ_{eff})	24.50	

The change in FoM due to the variation of n_s is shown in Fig. 2.6(b). Since the accuracy of detection of a sensor depends on FWHM of the response profile, the most applicable parameter to judge the performance of this kind of devices is FoM. FoM is the mostly used measure for the performance of SPR based sensors [134–136]. When n_s varies from 1.70 to 1.75, FoM does not vary much and remains ~ 24.5 RIU⁻¹ when calculated using μ_{eff} profile. Both S and FoM are maximum when $n_s = 1.75$. When $n_s > 1.75$, FWHM of μ_{eff} increases, and therefore, FoM decreases. Conversely, FoM ≈ 16 RIU⁻¹ at $n_s = 1.75$, when calculated using R profile. However, the maximum FoM of 17.5 RIU⁻¹ is observed at $n_s > 1.75$, when calculated using R profile.

In Table 2.1, we present a comparison of FoM of our work with several recently reported sensors based on SPR. Ref. 137 shows unnecessary MX₂ layers increment,

thus increased energy loss and reduced S. Ref. 139 shows poor detection accuracy. In Ref. 140, FoM analyze is based on wavelength and highest FoM is found at NIR wavelength. Ref. 48 shows increase in reflectivity for increasing number of graphene and MoS₂ layers. Moreover, most of the recently reported SPR sensors are based on complex hetero-structures with different two dimensional materials. As a result, the fabrication complexity and the cost of these sensors are significantly increased. On the other hand, the Kretschmann based structure is very simple and using optical magnetism the FoM of our proposed method is significantly greater than that of the techniques in Table 2.1.

It is important to note that the prospect of achieving optical magnetism at visible wavelength by IMI planar Kretschmann sensor has newly been a subject of enormous concern. In this work, we have determined magnetic resonance at a specific n_s of the target sample. We hope this magnetic resonance can be created in low n_s using different 2-D dielectric layer such as graphene, MoS₂ on metal surface. Optimization and nano-structuring of metal/dielectric thickness and refractive index, we can creates magnetic resonance at different n_s . Moreover, we can shift this magnetic resonance at low n_s applying small incident wavelength like 545 nm.

2.6 Conclusion

We show that strong magnetic resonance is created in SPR sensors based on Kretschmann configuration. The magnetic response μ_{eff} of the structure can be approximately an order of magnitude greater at resonance than that when out of resonance, which shows promises of the magnetic property of these structures in sensing applications. Thus using μ_{eff} profiles for sensing could lead to a novel approach for detection of different critical organic and inorganic samples. Our calculations based on S-parameters retrieval method show that the sensor FoM can be greatly increased

using the optical magnetism compared to that obtained using the conventional technique in state-of-the-art sensors, which often employ much more complex structures. We believe that the increased sensor performance using optical magnetism resonance in the presence of a target sample from a very simple planar layered structure can lead this approach to applications of sensing of variety of organic and inorganic materials.

CHAPTER 3

GATE-CONTROLLED GRAPHENE SPR GLUCOSE SENSOR

We propose a surface plasmon resonance (SPR) glucose sensor where a graphene mono-layer is used with controllable optical property by applying a gate voltage. We show that the gate voltage to the graphene mono-layer can increase the light absorption, and hence, the sensitivity of the proposed glucose sensor significantly. We find that the sensitivity and figure-of-merit of the proposed sensor increase by 21.48% and 49.57% when a 20-V gate voltage is applied to the graphene mono-layer compared to that when there is no gate voltage applied to the graphene mono-layer. We present a linear regression analysis for detecting the blood sugar level (BSL) using the proposed sensor that shows a highly reliable performance of the proposed sensor. We also present the effects of temperature on the proposed sensor performances. We find that the error in the detection of BSL remains within 4.75% on average and within 7.40% in the worst-case scenario when temperature varies by ± 10 °C from a reference 25 °C. Comparisons of the proposed sensor with several state-of-the-art sensors show a significantly enhanced behavior, as well as the error induced due to the change in temperature is much smaller than that of 15%, which is used as an allowable error limit for off-the-shelf glucose meters.

3.1 Introduction

Diabetes is a common disease that affected approximately 463 million people in 2019 and may affect 700 million by 2045 [142]. Unrestrained diabetes creates many health problems, including damage to blood vessels and nerves, loss of kidney function and vision, stroke, heart attack, lower limb seizures, brain dysfunction, and early mortality [143]. Diabetes is a threat all over the world and a leading health problem for low- and middle-income countries [144]. The treatment of diabetes patients crucially depends on the fast and accurate measurement of the blood sugar level (BSL), especially when patients suffer from deficient BSL, i.e., in hypo and hyperglycemia conditions.

Usually, the BSL detection devices—commonly known as glucometers—use reflection photometry or electrochemical techniques [42]. Although the photometry technique offers high precision, its use in glucometers is limited due to the time-consuming sample preparation, requirement of regular calibration, and optical interference that affects results. By contrast, an electrochemical technique, although not as precise as photometry technique [145], is usually preferred for offering high sensitivity (S), low-cost, easy maintenance, and good reproducibility. Current off-the-shelf glucometers commonly use test strips containing glucose oxidase (GO) enzyme that reacts to blood sugar. When an electrical potential is applied across the strip, an electrical current is generated with a magnitude that depends on the BSL. In practice, glucometers must have a readout deviation of $\leq 15\%$ from the actual BSL at 95% times, according to regulatory authorities [43]. Crucially, $\sim 15\%$ deviation of the test results with electrochemical glucometers could be detrimental, especially when a person is on the borderline in the blood sugar map or critically ill who needs immediate and appropriate medication. Additionally, the chemical enzyme used in the test strips of electrochemical glucometers is sensitive to environmental factors such as the temperature and humidity. The test strips that are exposed to dry and hot

weather during packaging and shipping may have altered chemistry and reactivity of enzymes so much to affect the test results significantly [146].

Optical biosensors have shown promises in applications related to food security, biological substances monitoring, biomedical research, and disease detection [147–150]. However, the work on optical biosensors for glucose detection is still scarce. The detection of glucose or BSL using a spectral analysis of the reflected light profile and glucose-1-dehydrogenase, hexokinase, and GO enzymes based immobilization has been demonstrated [151, 152]. However, these optical biosensors require long detection time. Recently, diverse optical sensing techniques using photonic crystal fibers (PCFs), interferometers, resonant cavities, and mid-infrared photo-acoustics have been proposed to detect the BSL [153]. In particular, PCF-based glucose sensors offer high design flexibility and sensitivity, and large refractive index variation [153, 154]. Nevertheless, PCF-based sensors are not suitable for everyday glucometers for their intricate fabrication complexity [155].

During the last few decades, optical biosensors based on surface plasmon resonance (SPR) have attracted a significant interest for diagnosis of diseases. SPR biosensors do not require labels to detect the sample. Additionally, SPR biosensors offer advantages over other label-free biosensing techniques in real-time monitoring of biomolecule interactions, affinity, specificity, and kinetics during the bindings of biomolecules [21, 156, 157]. SPR sensors such as gold (Au)-coated dielectric materials have been proposed for the detection of glucose in blood, offering high accuracy and resolution [44]. However, such Au-coated SPR sensors suffer from chemical noise in the measurement and poor absorption of the incident light. Recently, an Au-chromium (Cr) nano-laminated SPR sensor has shown good performance in glucose detection [45], although it suffers from a limited detection range of the BSL.

To increase the sensitivity of SPR-based sensors, several research groups have proposed the use of graphene layers [21, 46, 47, 140, 158–160]. In practice, the excitation

of surface plasmon polaritons (SPPs) in graphene is difficult due to the momentum mismatch between the incident light and graphene plasmons. To date, several schemes have been exploited to excite SPPs in graphene, including employing prism coupling [53], sub-wavelength silicon grating [99], and resonant optical antennas [161]. A graphene mono-layer has zero band gap in the visible wavelength range and absorbs only $\sim 2.3\%$ of the incident light [48]. Therefore, multiple graphene layers and transition-metal-dichalcogenides (TMDC) or nano-structures on graphene layers are often used to increase the sensitivity and figure-of-merit (FoM) of biosensors [21, 126, 162, 163]. However, the increase of graphene layers broadens the full-width at half-maximum (FWHM) of the absorption profile, and the use of TMDC or nano-structures makes biosensor structures complex and costly [162].

In this chapter, we propose a gate-controlled graphene SPR glucose sensor. We show that an applied V_g increases the light absorption in the proposed glucose sensor, and hence, improves the sensor performance. To determine the sensor performance parameters, we use a transfer matrix method (TMM) based angular interrogation technique. We calculate mono-layer graphene conductivity using the Kubo formula for different applied V_g at 633 nm incident wavelength. To determine the measurement accuracy of BSL, we use a linear regression model. Our proposed gate-controlled graphene SPR glucose sensor offers significant improvement in the detection of sensitivity and FoM compared to that of state-of-the-art SPR biosensors. Furthermore, our proposed glucose sensor shows a detection error $\ll 15\%$ that is used as a tolerable performance for state-of-the-art glucose meters.

The rest of the chapter is organized as follows: In Sec. 3.2, we present the proposed sensor configuration. In Sec. 3.3, we describe the theoretical models that we used to calculate the graphene optical properties and the sensor performance when V_g is applied. We discuss the simulation approaches that we followed to solve the Maxwell equations using finite difference time domain (FDTD) technique in Sec. 3.4. We present and discuss the calculated sensor performances and measurement accuracy of BSL for different V_g in Sec. 3.5. Additionally, in Sec. 3.5, we analyze the effect

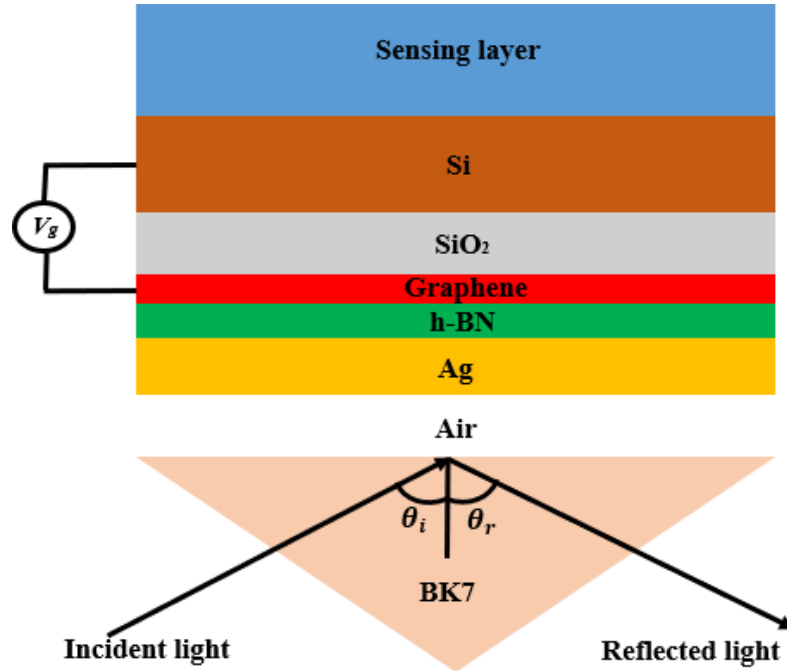


Figure 3.1: Schematic illustration of the proposed gate-controlled graphene SPR glucose sensor.

of temperature on the detection of BSL. In Sec. 3.6, we draw conclusions on the findings.

3.2 Sensor Configuration

The proposed gate-controlled graphene SPR glucose sensor consists of eight layers, as shown in Fig. 3.1. The first layer is a semi-infinite prism made of boro-silicate (BK7) glass material. The light is incident on the multi-layer sensor structure through the prism, and the reflected light intensity is recorded from the prism as well. A silver (Ag) layer follows the prism with an air gap between them. The air gap helps to increase the resonance dip of the reflection (R) profile [164]. The thicknesses of the air gap and Ag are chosen following the analysis presented in Fig. 3.2. Figure 3.2(a) shows the R profile of the proposed sensor as a function of the incidence angle (ϑ) of

light for different thicknesses (d_{air}) of the air gap. The minimum value of R decreases as d_{air} decreases. In this work, $d_{\text{air}} = 40$ nm is chosen as an even smaller air gap will complicate the fabrication of the plano-convex singlet lens to create the air gap [165]. Figure 3.2(b) shows R against ϑ for different thicknesses (d_{Ag}) of Ag. We note that the minimum R occurs at $d_{\text{Ag}} = 45$ nm. Therefore, d_{Ag} was chosen as 45 nm in this work.

An ultra-thin hexagonal boron nitride (h-BN) layer separates graphene from Ag. The h-BN layer has a thickness of 1 nm, which maximizes light absorption by the sensor [166]. The presence of h-BN between graphene and Ag increases the lifetime of the excited SPPs in the graphene layer [167, 168]. The used graphene is mono-layer, i.e., the thickness is 0.34 nm. An increase in the number of graphene layer widens the R profile. In the visible and near-infrared frequencies, the permittivity (ϵ) of graphene mono-layer is controllable by an applied V_g . Thin layers of silicon dioxide (SiO_2) and silicon (Si) are added on the top of graphene for stronger absorption of the incident light [169]. Figure 3.2(c) shows that R decreases as the SiO_2 thickness (d_{SiO_2}) decreases. In this work, $d_{\text{SiO}_2} = 8$ nm is chosen since the SiO_2 layer works as an insulating layer between the graphene and Si layer. The gate voltage V_g is applied between the graphene and Si layer to control the electron density (n) and E_f of graphene [169, 170]. The thickness of Si layer is chosen as 50 nm to achieve high electric field [171]. The sensing medium, i.e., blood sample, is placed on the Si layer. In this work, a fixed 100-nm-thick sensing layer is assumed.

Practically, a thermal vapor deposition technique can be used to deposit Ag on the top of BK7 substrate [159]. The graphene layer can be deposited on h-BN by dissolving atomic carbon in vacuum using high temperature [159]. Different dielectric materials can be grown on top of each other using evaporation techniques [172].

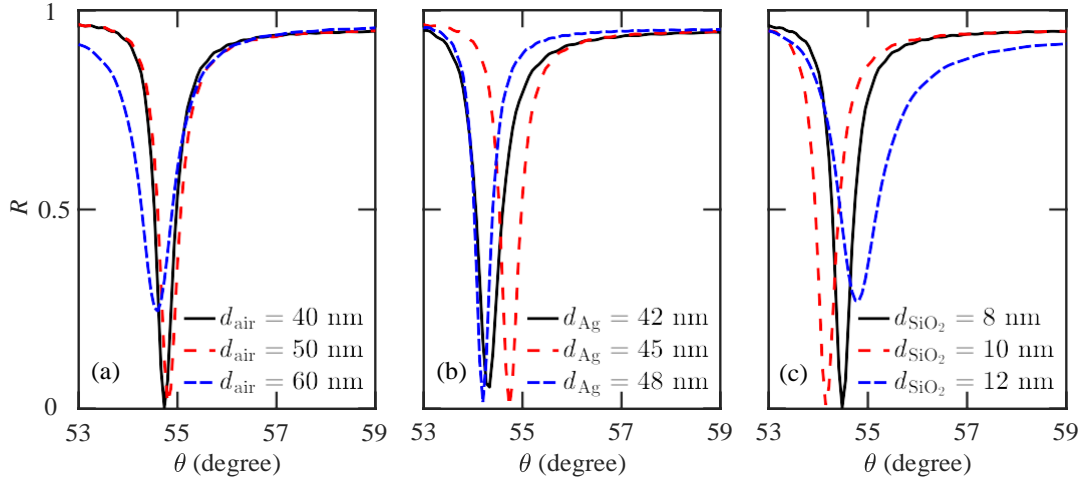


Figure 3.2: R vs. ϑ of the proposed sensor for different thicknesses of (a) air gap, (b) Ag, and (c) SiO_2 . In these studies, $n_s = 1.3323$.

3.3 Theoretical Modeling

3.3.1 Optical Properties

The response of the proposed sensor to an incident light will depend on the complex refractive indices of the materials in different layers. The response of the sensor will also depend on the wavelength of the incident light when a material has dispersive optical property. In this work, we investigate the sensor performance for an incident wavelength of 633 nm, which is often used in experiments for SPR-based techniques [173]. We follow an approach described in Ref. [46] to calculate the wavelength-dependent refractive index of BK7 prism. The refractive index of Ag is calculated using the Drude-Lorentz model [174], while the refractive indices of h-BN, SiO_2 , and Si are obtained from the published literature [175–177]. The refractive indices and thicknesses for different layers of the proposed structure are given in Table 3.1.

The complex refractive index of graphene will depend on several operating parameters, especially on the applied control voltage across it. Therefore, the calculation of graphene refractive index requires a special treatment. The complex permittivity

Table 3.1: Refractive indices and thicknesses of different layers of the proposed glucose sensor. The refractive indices are for a 633-nm incident light.

Material	Refractive index	Thickness (nm)
BK7	1.515	semi-infinite
Air	1.00	40
Ag	Real: 0.055 Imag: 4.285	45
h-BN	1.670	1
Graphene	V_g -dependent	0.34
SiO ₂	1.460	8
Si	3.881	50
Blood sample	Concentration-dependent	100

of a two-dimensional (2-D) mono-layer graphene sheet can be given by [178]

$$\epsilon(\omega) = 1 + i \frac{\sigma}{\omega \epsilon_0 t}, \quad (3.1)$$

where ϵ_0 is the permittivity of free space, ω is the angular frequency of the incident wave, σ is the conductivity, and t is the thickness of a graphene mono-layer. If ω and t are fixed, the permittivity of graphene basically depends on σ , which can be calculated using the so-called Kubo formula [179]

$$\sigma = i \frac{e^2 k_B T}{\pi \hbar^2 (\omega + i\tau^{-1})} \frac{E_f}{k_B T} + \frac{2 \ln \frac{\exp \left(\frac{E_f}{k_B T} \right) + 1}{2} + \frac{E_f}{\hbar (\omega + i\tau^{-1})}}{4\pi \hbar \ln \frac{\exp \left(\frac{E_f}{k_B T} \right) + 1}{2} + \frac{E_f}{\hbar (\omega + i\tau^{-1})}}, \quad (3.2)$$

where k_B is the Boltzmann constant, \hbar is the reduced Planck constant, e is the charge of an electron, and τ is the relaxation time of carriers in graphene that are excited due to the absorption of incident light. The first term on the right hand side of Eq. (3.2) is the conductivity that originates from intra-band carrier transitions due to light absorption, whereas the second term is the conductivity that originates from the inter-band carrier transitions.

The carrier relaxation time τ depends on E_f and Fermi velocity (V_f) by the following relation [41]

$$\tau = \frac{\mu E_f}{eV_f^2}, \quad (3.3)$$

where $V_f = 10^6$ m/s and E_f is related to n as $E_f = \hbar V_f (\pi n)^{1/2}$ [180]. Now, when there is a gate voltage applied between the graphene and Si layer of the proposed structure as shown in Fig. 3.1, n can be calculated using a parallel-plate capacitor model as [180]

$$n = \epsilon_0 \epsilon_d \frac{V_g}{ed}, \quad (3.4)$$

where ϵ_d and d are the dielectric constant and the thickness of insulating SiO₂ layer, respectively. We note that E_f , and in turn, τ can be changed by V_g . Thus, V_g can be used to change the optical behavior of graphene. The carrier relaxation time also depends on mobility μ , which is related to n and temperature (T) given by [181]

$$\mu(n, T) = \frac{\mu_0}{1 + (n/n_{\text{ref}})^\alpha} \times \frac{1}{1 + (T/T_{\text{ref}} - 1)^\beta}, \quad (3.5)$$

where $\mu_0 = 230000$ cm²V⁻¹s⁻¹, $n_{\text{ref}} = 1.1 \times 10^{13}$ cm⁻², $T_{\text{ref}} = 300$ K, $\alpha = 2.2$, and $\beta = 3$, respectively [181, 182]. In this work, we assume that the sensor is at room temperature, i.e., $T = 300$ K.

The optical property of blood, i.e., the refractive index of sample (n_s) will depend on the concentration of glucose mixed in it, and can be calculated as [153]

$$n_s = 0.000119 \times C + 1.33231, \quad (3.6)$$

where C is the density of glucose solution. A 10% (w/v) glucose solution is 10 g (w) glucose dissolved in 100 ml (v) water. The sugar level in blood sample (D) can be calculated by $D = C/M$ mg/dl, where M is the molar mass of glucose, which is 180.156 g/mol. We have calculated n_s using Eq. (3.6) for different BSLs, as shown in Fig. 3.3 [183]. The normal sugar level in blood is between 50 mg/dl to 139 mg/dl [184], which correspond to n_s from 1.3513 to 1.3864. A person is pre-diabetic if the

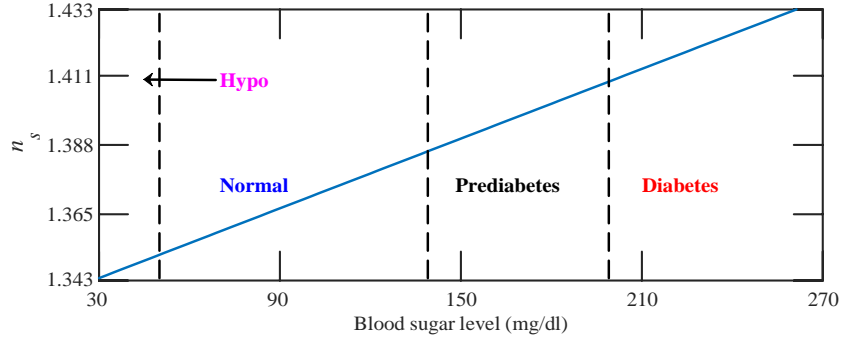


Figure 3.3: Refractive index of the blood sample (n_s) as a function of blood sugar level.

BSL is between 140 mg/dl and 199 mg/dl, and diabetic if $BSL \geq 200$ [184]. A BSL of < 50 mg/dL is considered extremely low and alarming for human body [185]. In this work, we have chosen BSL from 30 mg/dl to 270 mg/dl to cover the entire BSL map that could be important to understand the performance of the proposed sensor.

3.3.2 Response to the Incident Light

To calculate the SPR dynamics of the proposed gate-controlled glucose sensor, we have solved 2-D full-field vectorial Maxwell's equations using the FDTD technique. The incidence angle of light has been varied to determine the reflection profile. To calculate the reflection profile, we have used TMM and considered the proposed structure an N -layer system, as shown in Fig. 3.1. For the incident transverse magnetic (TM) light, we can write [186]

$$R = |r_p|^2, \quad (3.7)$$

where r_p is the reflection coefficient for the TM-polarized incident light. We have calculated S of the proposed glucose sensor by [187]

$$S = \frac{\Delta\theta_r}{\Delta n_s}, \quad (3.8)$$

where $\Delta\vartheta_r$ is the change in resonance angle (ϑ_r) due to a change in the sample index Δn_s . FoM can be calculated by [188]

$$\text{FoM} = \frac{S}{\text{FWHM}}. \quad (3.9)$$

3.4 Simulation Approach

In this work, 2-D FDTD simulations have been carried out to determine the dynamics of the incident light with the sensor. The simulation domain is 2000 nm in the y -direction, i.e., in the direction of the layer interfaces, and 6000 nm in the x -direction, i.e., in the direction perpendicular to the layer interfaces. A non-uniform meshing scheme has been employed in the simulation region to optimize the computational efficiency and precision of FDTD solutions by limiting the overall error caused by meshing to only $< 0.05\%$. Additionally, a finer meshing is used in a smaller $600 \text{ nm} \times 300 \text{ nm}$ region on the x - y plane centering the graphene and h-BN interface. In this fine meshing region, mesh-grids $\Delta x = 0.1 \text{ nm}$ and $\Delta y = 0.2 \text{ nm}$ have been chosen. The perfectly-matched layer (PML) boundary condition was used at the edges of the simulation region in the x -direction and Bloch boundary condition was used in the y -direction. The incident light has a 633-nm wavelength with TM polarization. The incidence angle has been varied from 45° to 70° to calculate the R profile. The incident light source is located at 3500 nm from the Air-Ag interface, whereas the detection plane of the reflected light is located at 3800 nm from the same interface.

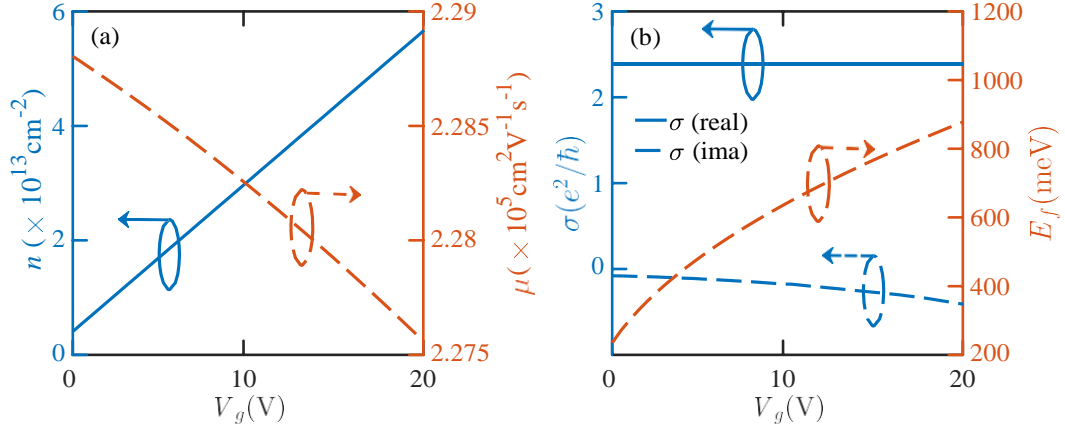


Figure 3.4: (a) n and μ and (b) σ and E_f of a graphene mono-layer as functions of V_g . We assume $\epsilon_0 = 8.85 \times 10^{-12} \text{ Fm}^{-1}$, $\epsilon_g = 3.9$, $d = 8 \text{ nm}$, and $e = 1.6021 \times 10^{-19} \text{ C}$.

3.5 Results and Discussion

3.5.1 Sensor Performance

To determine the performance of the proposed gate-controlled graphene SPR glucose sensor, we have assumed a pure graphene mono-layer in the sensor. The graphene mono-layer has $n = 1.08 \times 10^{13} \text{ cm}^{-2}$, $E_f = 38.34 \text{ meV}$, and $\mu = 23 \times 10^4 \text{ cm}^2 \text{ V}^{-1} \text{ s}^{-1}$ when there is no applied V_g to it. We have varied V_g so that graphene parameters change, and so do the sensor performances. The results are presented for $V_g \leq 20 \text{ V}$, as thermally generated intrinsic carriers from graphene with $V_g > 20 \text{ V}$ may cause inaccurate results and a permanent fault in the structure [170, 189]. Figure 3.4 shows the properties of a graphene mono-layer as V_g varies from zero to 20 V. In Fig. 3.4(a), we find that n increases and μ decreases with the increase of V_g . In Fig. 3.4(b), we find that E_f increases as V_g increases since E_f is directly related to n . We have also calculated τ as V_g varies and found that τ increases as V_g increases. In particular, we find $\tau = 8.74, 11.42, 14.50, 17.05, \text{ and } 19.97 \text{ ps}$ when $V_g = 0, 5, 10, 15, \text{ and } 20 \text{ V}$, respectively.

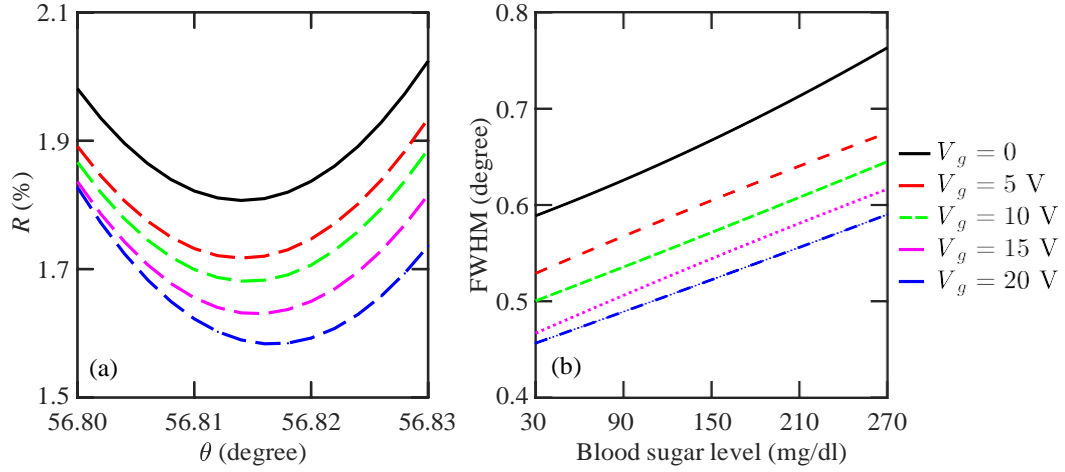


Figure 3.5: (a) R as a function of ϑ and (b) FWHM of the R profile as a function of the BSL of the proposed gate-controlled graphene SPR glucose sensor for different V_g . To calculate R profile, we assume $n_s = 1.3625$, which corresponds to a BSL of 78.60 mg/dl.

Generally, the conductivity of graphene depends on both intra- and inter-band absorption of the incident light. When the incident light wavelength is 633 nm, the incident photon energy $E_p > 2E_f$, and therefore, strong inter-band absorption occurs. However, E_f can be increased by applying V_g and the inter-band transitions with $E_p < 2E_f$ can be blocked due to Pauli blocking [190]. When $E_p < 2E_f$, intra-band absorption dominates, and graphene optical properties mainly depend on τ . Therefore, graphene optical properties can be changed by controlling V_g when $E_p < 2E_f$ [178]. In this work, the proposed sensor has been designed for $E_p < 2E_f$ to control the graphene optical properties by controlling V_g .

Figure 3.4(b) shows both real and imaginary parts of σ of a graphene mono-layer as functions of V_g . We note that the real part of σ does not vary as V_g increases. By contrast, the imaginary part of σ gradually decreases as V_g increases from zero to 20 V. Mono-layer graphene supports TM plasmons from terahertz (THz) to mid-infrared (MIR) wavelength range, although transverse electric (TE) plasmons can be excited up to visible wavelength. When V_g increases, E_f increases as well. Therefore, TM plasmons of mono-layer graphene can be obtained at 633 nm wavelength. A

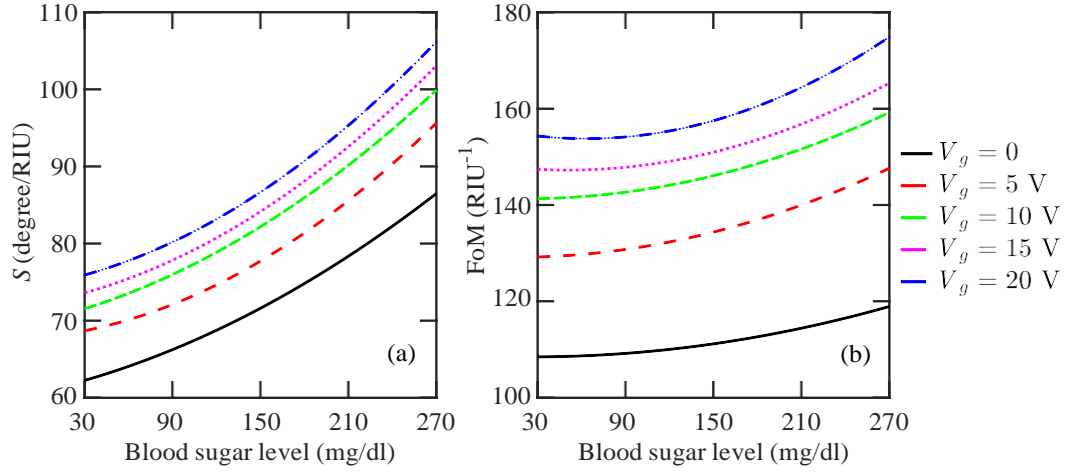


Figure 3.6: (a) S and (b) FoM as functions of BSL of the proposed glucose sensor for different V_g .

similar trend is observed for intra-band absorption from THz to MIR range [95, 191]. As a result, the incident light is strongly absorbed in the graphene mono-layer of our designed sensor. The complex refractive index of a graphene mono-layer has been calculated from σ , as given in Eq. (3.1), to be used in FDTD simulations.

Figure 3.5(a) shows R as a function of ϑ for five different values of V_g . Here, the sample has a BSL = 78.60 mg/dl, which corresponds to $n_s = 1.3625$. Since the light absorption by graphene increases with V_g , R decreases with V_g . The absorption of incident light increases by 16.88% when V_g increases from zero to 20 V. We note that ϑ_r increases with V_g . The changes of ϑ_r and R with V_g have a significant impact on the sensor performance parameters.

Figure 3.5(b) shows the FWHM of R profile of the proposed glucose sensor for different V_g when the BSL varies from 30 mg/dl to 270 mg/dl. We note that FWHM of R increases as the BSL increases. The excited SPPs decay at a faster rate when BSL increases as n_s increases with BSL. As a result, the FWHM of the R profile increases. By contrast, FWHM of the R profile decreases as V_g increases. A smaller FWHM will decrease the spectral noise and increase the signal-to-noise ratio (SNR)

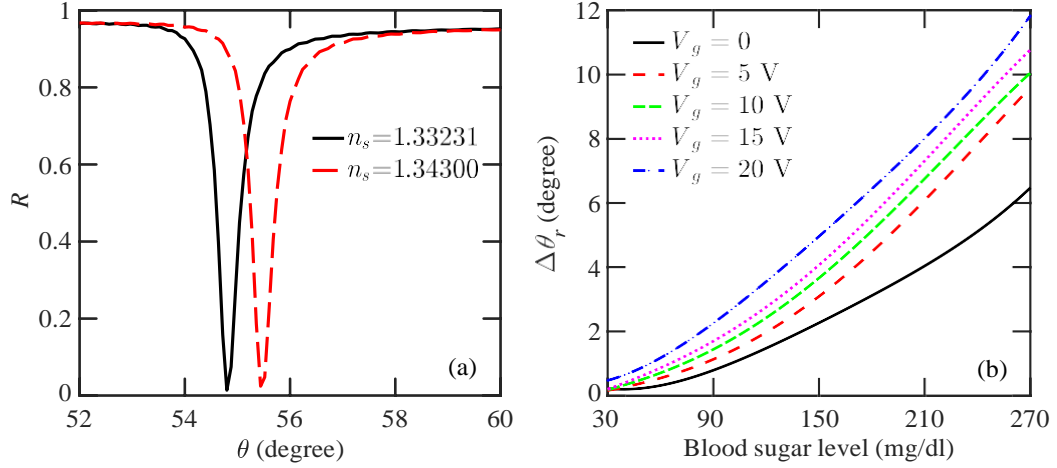


Figure 3.7: (a) R profile as a function of ϑ and (b) $\Delta\vartheta_r$ as functions of BSL and V_g for the proposed glucose sensor.

of the detected signal. When V_g increases, the graphene mono-layer strongly confines the incident light, and we find that the FWHM of the R profile decreases.

Figure 3.6(a) shows S of the proposed gate-controlled graphene SPR glucose sensor as a function of the BSL. We note that S increases as BSL increases and reaches 108 degree/RIU for $V_g = 20$ V and BSL is 270 mg/dl. We also note that S increases as V_g increases. Notably, S increases by 21.48% when V_g increases from zero to 20 V for a BSL of 270 mg/dl. As S depends on the change of ϑ_r and a greater V_g shows a greater change in ϑ_r , we find that S increases as V_g increases. In Fig. 3.6(b), we show FoM as a function of the BSL for different gate voltages. We note that FoM increases with the increase of both BSL and V_g . When $V_g = 20$ V, the maximum FoM is 178 RIU^{-1} at 270 mg/dl BSL. We note that FoM increases by 49.57% when V_g increases from zero to 20 V in the range of BSL considered in this work. As the negative value of imaginary σ increases with the increase of V_g , a mono-layer graphene absorbs more light as V_g increases. Therefore, FoM increases as V_g increases.

The change in ϑ_r , i.e., $\Delta\vartheta_r$, in the R profile with the change in BSL represents the selectivity of an SPR sensor [84]. Figure 3.7(a) shows R as a function of ϑ for two different n_s when $V_g = 0$. The first resonance is observed at 54.80° when $n_s = 1.3323$,

Table 3.2: Performance comparison of our proposed sensor with several recently proposed graphene-based sensors.

Sensor Configuration	n_s	S (degree/RIU)	FoM (RIU ⁻¹)
SF10/ZnO/Au/MoS ₂ /graphene/sample [48]	1.330–1.450	101.58	15.11
SF10/Au/WS ₂ /graphene/sample [162]	1.400	95.71	25.19
BK7/Ag/graphene /sample [192]	1.330–1.370	91.76	52.31
SF10/Cr/Ag/graphene /affinity/sample [138]	1.432	61.54	8.90
This work	1.343–1.433	108.00	178.00

which corresponds to zero BSL. The second resonance is observed at 55.24° when $n_s = 1.3430$, which corresponds to 30 mg/dl BSL. In Fig. 3.7(a), $\Delta\vartheta_r = 0.44^\circ$ when $V_g = 0$. By contrast, Fig. 3.7(b) shows $\Delta\vartheta_r$ with the change of BSL at different V_g . We find that the sensor becomes more selective when BSL and V_g increase. The increase of $\Delta\vartheta_r$ with BSL implies that the proposed sensor has affinity toward glucose.

We find that the calculated S and FoM of the proposed sensor are much greater than that of the state-of-the-art optical sensors in the detection of BSL. In Table 3.2, we compare S and FoM of our proposed glucose sensor with several recently proposed sensors that use graphene in the structure. The wavelength of the incident light is 633 nm in all cases presented in Table 3.2. Also, only a graphene mono-layer is used in all cases, except in Ref. [48], where 13 layers of graphene are used. In this work, the S and FoM have been calculated for the sensing layer refractive indices 1.343–1.433, which correspond to 30–270 mg/dl BSL. The maximum S and FoM of the proposed sensor are obtained when the sensing layer index is 1.433. In Table 3.2, the S and FoM of the proposed sensor are compared with that of the sensors, which report results with a sensing layer index close to 1.433.

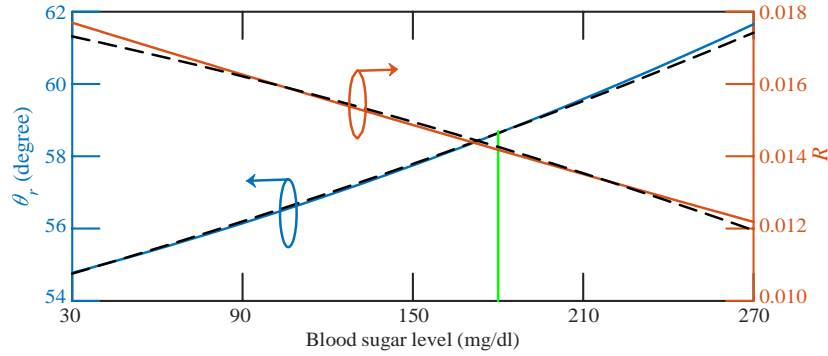


Figure 3.8: Simulation results of ϑ_r and R vs. BSL (dashed lines), and regression lines of ϑ_r and R vs. BSL (solid lines). The solid green line determines 180 mg/dl BSL, when measured $\vartheta_r = 58.8^\circ$ or $R = 0.01425$. We assume $V_g = 20$ V.

3.5.2 Detection Accuracy

Accuracy is a key performance parameter for a sensor in the detection of the BSL. The parameters R and ϑ_r can be used individually or simultaneously in the proposed sensor to detect and measure the BSL precisely. The determination of the BSL using ϑ_r and R simultaneously will be more precise, however, with an increase in the complexity of the measurement technique. Figure 3.8 shows the dependence of R and ϑ_r on BSL when $V_g = 20$ V. Figure 3.8 also shows linear regression lines drawn for the relations ϑ_r vs. BSL and R vs. BSL. The regression lines $y = a + bx$ have been determined for both ϑ_r vs. BSL and R vs. BSL relations, where a is the intercept on the y -axis, b is the slope, x is the BSL, and y is either ϑ_r or R , respectively [193]. We find that the BSL estimated by ϑ_r provides a better accuracy than that estimated by R as the regression line for ϑ_r fits better with the simulated values. Notably, the coefficient of determination (R^2) is 96.50% for the linear regression line for ϑ_r , while 94.11% for the linear regression line for R . The linear regression lines can be used as a reference to detect the BSL for the proposed sensor. For example, when measured $\vartheta_r = 58.80^\circ$, we can decide that the BSL is 180 mg/dl using the reference regression line for ϑ_r .

3.5.3 Effects of Temperature

The accuracy of a glucose sensor depends on many factors, including the strip manufacturing process, chemical stability of enzyme, sample collection method, sample amount, and most importantly the temperature at which the measurement takes place. We have analyzed the effects of temperature on the detection of BSL by the proposed sensor. In the analysis, we have assumed $T = 25\text{ }^{\circ}\text{C}$ as a reference temperature and varied it by a maximum $\Delta T = \pm 10\text{ }^{\circ}\text{C}$.

Optical properties of layers of the proposed sensor, except for the Ag layer, do not significantly depend on temperature, especially at the incident 633 nm wavelength and in the temperature range around $25\text{ }^{\circ}\text{C}$. In particular, the change of the refractive indices of BK7, h-BN, SiO_2 , and Si due to the change in temperature is negligible in the visible wavelength range [194–197]. Therefore, in the range $T = 15\text{--}35\text{ }^{\circ}\text{C}$, the change in optical properties of most layers of the proposed sensor is negligible.

The temperature dependence of the optical property of graphene is a little more complicated due to its unique properties. The effect of temperature on the optical property of graphene will depend on μ and τ , and hence, σ . Since the temperature dependence of the optical property of graphene is not well-studied and not available in the literature, we have calculated it in this work. In Fig. 3.9, we show μ vs. temperature, and τ vs. temperature for a graphene mono-layer calculated using Eq. (3.5). We find that both μ and τ do not vary with temperature when V_g remains fixed. We note that the work function and E_f of a graphene mono-layer do not depend on temperature as well [198]. As a result, σ , and hence, the optical property of a graphene mono-layer does not change with temperature for the cases considered in this work.

Therefore, the temperature-sensitive performance of the proposed sensor will depend only on the temperature-dependent optical property of Ag. We use the Drude-Lorentz model to calculate the temperature-dependent optical property of Ag, i.e.,

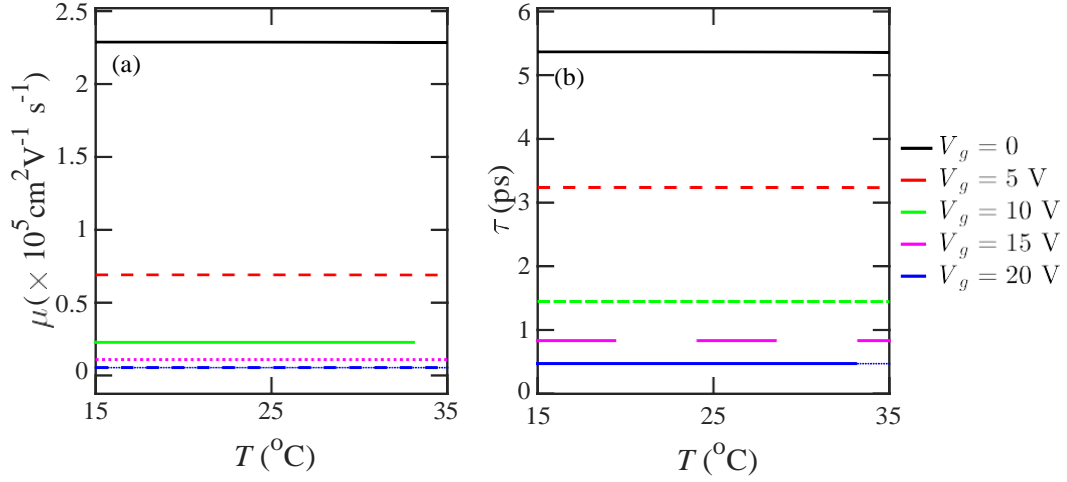


Figure 3.9: Effects of T on graphene (a) μ , and (b) τ for five different V_g .

the effect of temperature on the dielectric constant of Ag. The expression of ϵ of Ag is given by [174]

$$\epsilon = 1 - \frac{\omega_p^2}{\omega(\omega + i\omega_c)}, \quad (3.10)$$

where ω_p and ω_c are the plasma and collision frequencies, respectively. The collision or scattering frequency ω_c depends on temperature and can be written as [199]

$$\omega_c = \omega_{ce} + \omega_{cp}, \quad (3.11)$$

where ω_{ce} and ω_{cp} are the electron–electron and electron–phonon scattering frequencies in Ag. The temperature dependence of ω_{ce} can be described by the Lawrence model [200]

$$\omega_{ce} = \frac{\pi^3 \Gamma \Delta}{12 \hbar E_f} (k_B T)^2 + \frac{\hbar \omega}{2\pi} 2^{\#}, \quad (3.12)$$

where Δ is the fractional scattering and Γ is the Fermi-surface average of the scattering probability. We assume $\Delta = 0.75$ and $\Gamma = 0.55$ [200]. The temperature dependence of ω_{cp} can be described using the Holstein's model [201]

$$\omega_{cp} = \omega_0 \left[\frac{2}{5} + \frac{4T^5}{\Theta_D^5} \int_0^{\Theta_D/T} \frac{z^4}{e^z - 1} dz \right] 2^{\#}, \quad (3.13)$$

where Θ_D is the Debye temperature, Z is the quasi-particle weight, and ω_0 is a constant [202]. We have used $\Theta_D = 227.3$ K, $Z = 0.8$, and $\omega_0 = 0.05$ [202]. Lastly, ω_p has been calculated using [203]

$$\omega_p = \sqrt{\frac{4\pi N e^2}{m}}, \quad (3.14)$$

where m is the effective mass of an electron and N is the density of conduction electrons.

The optical property of the blood sample also depends on temperature. The temperature-dependent n_s can be obtained using [204]

$$n_s = 1.3356 + (1.5333 \times 10^{-3}) \times C - (9.0 \times 10^{-5}) \times C^2 - (1.2647 \times 10^{-4}) \times (T - 273.15) - (4.0 \times 10^{-8}) \times (T - 273.15)^2. \quad (3.15)$$

To determine the temperature-dependent measurement error for the proposed sensor, we have considered two cases: (i) First, we have assumed that only the sensor temperature varies while the sample temperature remains fixed and (ii) Second, we have assumed that the sensor and sample temperatures are equal and vary simultaneously. While the first case signifies the temperature-sensitive performance of the proposed sensor, the second case helps us know the performance in an actual condition. Figure 3.10 shows ϑ_r vs. BSL for three different temperatures of the sensor. The sample temperature is kept fixed at 15 °C, 25 °C, and 35 °C in Figs. 3.10(a), 3.10(b), and 3.10(c), respectively. We find that while ϑ_r increases when the sensor temperature decreases, ϑ_r decreases when the sensor temperature increases.

The percentage error in the detection of BSL is calculated using the following equation

$$\%Error = \frac{BSL_{25^\circ C} - BSL_{T_{diff}^\circ C}}{BSL_{25^\circ C}} \times 100, \quad (3.16)$$

where T_{diff} °C is the temperature at which the BSL is calculated. The maximum and average calculated %Error for the cases presented in Fig. 3.10 are given in Table 3.3.

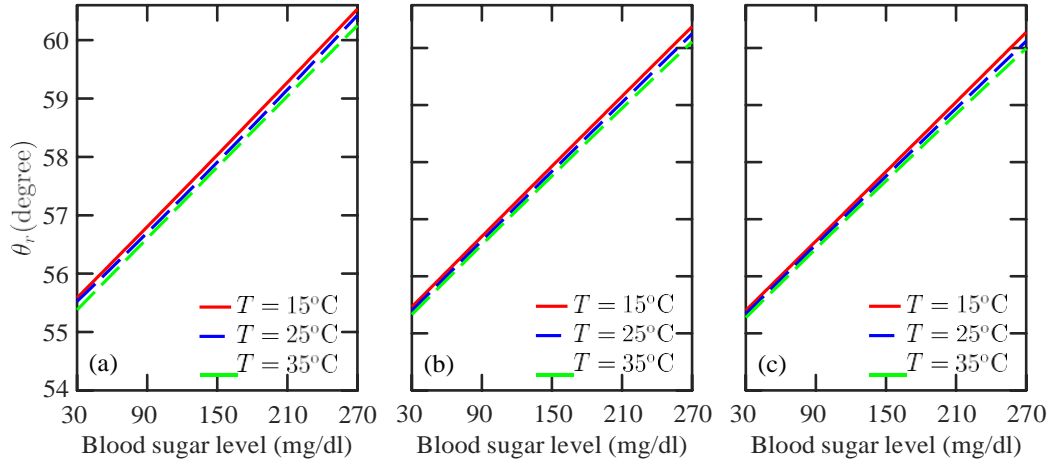


Figure 3.10: ϑ_r vs. BSL of the proposed sensor for different sensor temperature. We assume that the sample temperature remains fixed at (a) 15°C , (b) 25°C , and (c) 35°C .

We note that the maximum error is 7.12% when the sensor temperature varies by 10°C and the sample temperature is 15°C . We also note that the average error of our proposed sensor remains $< 4\%$ for a $\Delta T = \pm 10^\circ\text{C}$.

Next, we present results when both the sensor and sample layer have the same temperature. Figure 3.11 shows the effects of temperature on ϑ_r of the proposed glucose sensor as the temperature of the sensor and sample layer change simultaneously. We note that the effects of temperature become more pronounced as the glucose

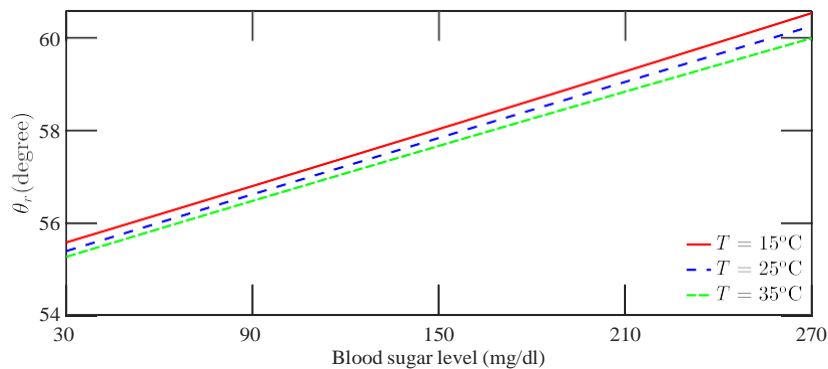


Figure 3.11: ϑ_r vs. blood sugar level for different temperatures (T) of the sensor and sample layer. The sensor and sample layer temperatures are equal and they vary simultaneously.

Table 3.3: Maximum measurement error and average error of detected BSL when sensor T is varying from 25°C for different n_s temperature.

Sample temperature ($^\circ\text{C}$)	Sensor temperature variation ($\Delta T, ^\circ\text{C}$)	Maximum %Error	Average %Error
15	10	7.12	3.70
	5	3.56	2.05
	-5	-3.52	-1.72
	-10	-7.06	-3.51
25	10	4.70	2.97
	5	3.72	1.70
	-5	-3.24	-1.70
	-10	-3.86	-2.55
35	10	3.40	2.90
	5	3.32	1.74
	-5	-3.46	-1.81
	-10	-4.02	-2.61

level increases. We find a maximum error of 7.40% when the temperature varies by -10°C , i.e., when $T = 15^\circ\text{C}$. In Table 3.4, we show the error in the detection of the BSL due to temperature changes of the sensor and the sample. Notably, the absolute value of the average error remains $<5\%$.

Table 3.4: Maximum and average %Error of the calculated BSL when both the sensor and sample temperatures vary.

ΔT ($^\circ\text{C}$)	Maximum %Error	Average %Error
10	6.44	3.66
5	3.68	2.34
-5	-4.08	-2.26
-10	-7.40	-4.75

3.6 Conclusion

We have proposed a label-free graphene SPR sensor that shows a tunable optical property with the applied gate voltage. The proposed glucose sensor offers enhanced performances compared to state-of-the-art graphene-based optical sensors. The proposed sensor performances increase as the applied gate voltage increases. The sensor

can detect and measure the BSL with high precision either using the resonance angle or the reflection profile. Since our proposed sensor detects BSL without using labels and does not require chemical enzymes, the environmental factors do not have any lasting effect on the performance, except for the temperature-induced index variation of metal at the moment of detection. However, the change in temperature by ± 10 °C around room temperature affects the detection accuracy by only < 5%.

CHAPTER 4

GRAPHENE SP SENSOR FOR ULTRA-LOW-LEVEL SARS-COV-2 DETECTION

The precise detection of the ultra low-level severe acute respiratory syndrome coronavirus 2 (SARS-CoV-2) is critically important at this moment. The detection mechanism should be sensitive, low-cost, portable, fast, and easy to operate to tackle the pandemic. This work proposes a sensor exploiting graphene surface plasmon resonance to detect the SARS-CoV-2. The graphene layer functionalized with angiotensin-converting enzyme 2 (ACE2) antibodies will help efficient adsorption of the SARS-CoV-2. In addition to the graphene layer, ultra-thin layers of novel two-dimensional materials tungsten disulfide (WS_2), potassium niobate ($KNbO_3$), and black phosphorus (BP) or blue phosphorus (BlueP) used in the proposed sensor will increase the light absorption so that an ultra-low SARS-CoV-2 concentration can be detected. The analysis presented in this work shows that the proposed sensor will detect as small as ~ 1 fM SARS-CoV-2. The proposed sensor also shows a minimum sensitivity of 201 degree/RIU, a figure-of-merit of 140 RIU^{-1} , and strong binding kinetics of the SARS-CoV-2 to the sensor surface.

4.1 Introduction

Severe acute respiratory syndrome coronavirus 2 (SARS-CoV-2) is an important biological pathogen responsible for coronavirus disease 2019 (COVID 19). Recently, COVID 19 has caused an unprecedented health problem worldwide due to the high progression rate of fatality. SARS-CoV-2 is a positive-sense single-stranded ribonucleic acid (RNA) virus [205]. Several research groups have proposed and demonstrated efficient, cost-effective, and real-time detection techniques for the SARS-CoV-2 virus [76–82]. Culture-based techniques that detect nucleic acid or proteins and serological-based techniques that detect the created antibodies are commonly used for virus diagnosis [206]. Recent advances in molecular technology have led to the development of nucleic acid-dependent amplification techniques for virus detection, e.g., the reverse transcriptase quantitative polymerase chain reaction (RT-qPCR) technique. RT-qPCR is known as the gold standard for detecting several critical viruses, such as SARS-CoV-2, human immunodeficiency virus (HIV), and cytomegalovirus (CMV) [76].

RT-qPCR is highly sensitive and selective for SARS-CoV-2 detection [77]. Nevertheless, its application is limited due to significant false-negative cases (~15%), long processing time, costly instruments, and the requirement of skilled human resources and uninterrupted power supply over a long period [78, 79]. Conversely, colorimetric-based loop-mediated isothermal amplification (LAMP) techniques have been proposed for SARS-CoV-2 detection to overcome the limitations of an RT-qPCR technique [79]. LAMP techniques show a high nucleic-acid amplification efficiency but are time-consuming and tedious as they use electrophoresis for detection. Additionally, the decision regarding the color change of reaction vessels by human eyes is potentially a subjective issue and may significantly impact the test results [80].

A chest computer tomography (CT) scan can also be used to detect the SARS-CoV-2

[81]. However, such a technique cannot be used for asymptomatic patients, early-stage detection, and the measurement of the mass density of virus [83]. Serological tests, e.g., enzyme-linked immunosorbent assay (ELISA), can also be used for SARS-CoV-2 diagnosis [82]. Serological methods have shown high efficiency and are low-cost, but they suffer from low sensitivity (S) and producing false-negative reports [77].

In the last few years, optical sensors based on plasmonics have attracted momentous attention in virus detection due to their simplicity, flexibility, label-free operation principle, and short response time [76]. Plasmonics-based optical sensors have been proposed to detect many critical pathogens, such as dengue virus envelope (E)-protein, thyroglobulin, HIV-1, and SARS-CoV-2 [77, 84–88]. In particular, a toroidal plasmonic metasensor has recently been proposed for the detection of SARS-CoV-2 spike (S)-protein using terahertz (THz) wavelength signal, demonstrating a limit of detection (LoD) of only ~ 4.2 fM [87]. However, the plasmonic metasensor suffers from the insensitivity to S-protein concentration between 20 and 50 fM and low quality-factor (Q-factor). More recently, a surface plasmon resonance (SPR) based method has been proposed to examine the affinity of SARS-CoV-2 S-protein to angiotensin-converting enzyme 2 (ACE2) [207]. Additionally, plasmonic photothermal effect and localize surface plasmon resonance (LSPR) have been proposed to detect selected sequences of SARS-CoV-2 by nucleic acid hybridization techniques [78]. However, thermo-plasmonic heat cannot discriminate between two similar gene sequences, and a sensor employing this effect shows low detection accuracy. Furthermore, a near-infrared (NIR) plasmonic sensor has been suggested for SARS-CoV-2 S-protein detection using a phase interrogation technique [77]. Although an NIR plasmonic sensor shows high sensitivity, its performance is limited due to the complex technique required for phase variation measurement.

Recently, graphene surface plasmon (SP) has drawn significant interest for application in sensing due to two-dimensional (2-D) graphene's promising properties such

as high π -conjugation structure, shallow thickness and mass, and high mechanical strength [208]. In SPR sensors, the sample bio-molecules should be efficiently adsorbed by the sensor surface to increase the sensitivity [209]. Therefore, bio-molecular recognition elements (BREs) are often placed on top of SPR-based sensors to functionalize the metal film for enhanced bio-molecule adsorption. Since graphene surfaces can be modified by introducing different BRE functional groups, such as epoxy, hydroxyl, ketone, and carboxyl in their basal plane, graphene-based sensors show high bio-molecule adsorption capability [210]. Recently, apart from graphene, a few other 2-D materials, such as molybdenum disulfide (MoS_2) and blue phosphorus (BlueP), have been shown to significantly improve sensor sensitivity when used in simple metal-based SPR sensors [211]. Moreover, SPR biosensor based on bimetallic film such as gold (Au)-silver (Ag) using BlueP has shown good sensitivity [212] but limited performance in detecting ultra-low concentrations of biological molecules. However, using different 2-D materials like tungsten disulfide (WS_2), potassium niobate (KNbO_3), and black phosphorus (BP) in addition to graphene in a silver (Ag) based SPR biosensor is still unexplored, although they have optical properties promising for an SPR sensor.

This work proposes a graphene SPR sensor for ultra low-level SARS-CoV-2 detection. The proposed sensor will work on the Kretschmann configuration, thus being simple. The graphene layer is functionalized by ACE2 for efficient adsorption of the SARS-CoV-2 S-protein sample [88]. The proposed sensor uses thin layers of novel 2-D materials, particularly WS_2 , KNbO_3 , and BP or BlueP, between graphene and Ag layers to increase the light absorption, and hence, the sensor's sensitivity. The optical and electronic properties of 2-D hetero-structures highly depend on the number of 2-D material layers and the stacking patterns. Due to their excellent sensitivity enhancement effects, such as BlueP/BP, KNbO_3 , and WS_2 , we believe our proposed 2-D material-based plasmonic biosensor will find applications in practical biosensing [213].

This chapter discusses a theoretical work based on detailed analytical and numerical calculations. We apply the finite difference time domain (FDTD) technique to characterize the sensor response to an incident light. We also use a transfer matrix method (TMM) based angular interrogation technique to determine the sensor performance parameters. SARS-CoV-2 S-proteins are detected by calculating the change in resonance angle. We use the Langmuir model to calculate the equilibrium dissociation constant (K_D) to determine the binding kinetics between ACE2 and S-protein [84]. The proposed sensor shows potential to detect ultra-low SARS-CoV-2 concentration of only ~ 1 fM, which is critical for the early detection of this deadly virus. The proposed graphene SPR sensor also shows a high detection sensitivity, figure-of-merit (FoM), selectivity, and resolution while detecting the SARS-CoV-2 compared to that of the state-of-the-art SPR sensors. Furthermore, the proposed sensor offers a significantly small K_D , showing enhanced binding of SARS-CoV-2 on the sensor surface.

The rest of this chapter is prepared as follows: Sec. 4.2 illustrates and discusses the proposed sensor configuration and optimization of layer thicknesses. Then, Sec. 4.3 presents the optical properties of different materials, theoretical analysis of sensor performance parameters, and simulation methods. Next, we present and discuss the SARS-CoV-2 detection approach, analysis on binding between ACE2 and S-protein, and the calculated sensor performances in Sec. 4.4. Finally, in Sec. 4.5, we conclude the proposed sensor results.

4.2 Proposed Sensor

4.2.1 Configuration

The proposed graphene SPR sensor is designed based on the Kretschmann configuration, as shown in Fig. 4.1. The incident light on the metal–dielectric interface

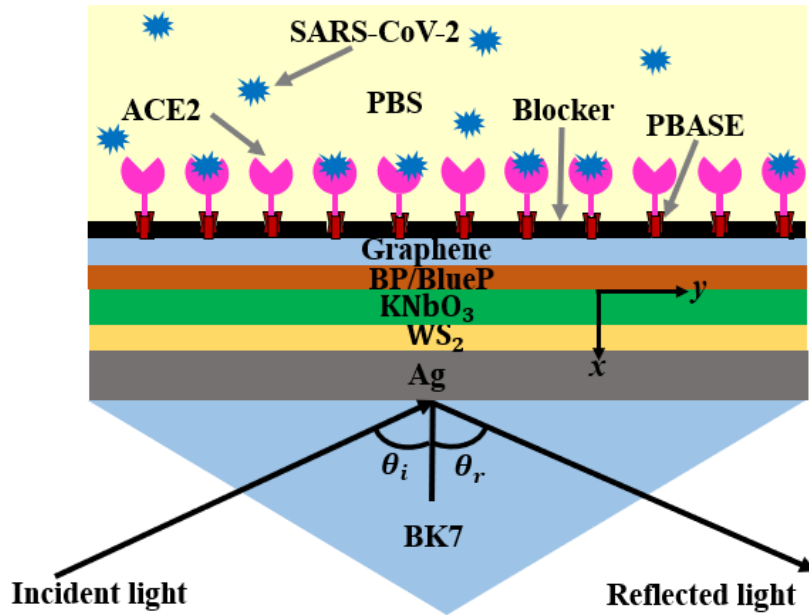


Figure 4.1: Schematic illustration of the proposed graphene SPR sensor for the SARS-CoV-2 S-protein detection.

at the resonance angle (ϑ_r) excites SPR, significantly absorbing the incident light. The ϑ_r for SPR changes based on the refractive index of the dielectric material, i.e., the sample layer. The sample layer refractive index varies due to the presence of SARS-CoV-2. Therefore, SARS-CoV-2 can be detected by measuring the change in ϑ_r . The SARS-CoV-2 will be placed on the top surface of the proposed sensor structure, which is a graphene layer. In practice, we will need binding molecules to immobilize antibodies on the graphene surface to capture the SARS-CoV-2. We use 1-pyrenebutyric acid N-hydroxy-succinimide ester (PBASE) that permits the binding of functional groups to graphene without disrupting the carbon atomic structure [214] and acts as an interfacing molecule and a probe linker [88]. PBASE contains an aromatic pyrenyl group, which physically interacts with graphene through π - π interaction. PBASE also contains a succinimidyl ester group, which covalently reacts with the amino group on the antibody by an amide bond [215].

SARS-CoV-2 consists of four fundamental physical proteins, such as S, E, matrix,

and nuclei-capsid proteins [216]. S-protein is immunogenic and shows amino acid sequence variation, permitting the specific detection of SARS-CoV-2 [216]. Hence, this work uses S-protein as the sensing element to identify the SARS-CoV-2 [88]. The S-protein contains protrusions that only bind to certain receptors on the host cell, such as ACE2, dipeptidyl peptidase-4, amino-peptidase N, and carcinoembryonic antigen-related cell adhesion molecule 1 [217]. Recent research results have confirmed that ACE2 is an effective receptor for SARS-CoV-2 S-protein, with SARS-CoV-2 grasping ACE2 cells primarily by endocytosis [218]. Therefore, thiol tethered DNA is used in this work as an ACE2 layer for receiving and detecting SARS-CoV-2 [219].

In this work, ACE2 antibodies are placed throughout the top surface of the sensor with 50 nm separations between the neighboring ACE2 antibodies. ACE2 height and width are assumed to be 3 nm and 2.1 nm, respectively [85]. To block the free space between ACE2 antibodies, we use ethanolamine as a blocker [220]. Each ethanolamine blocker is 3.5-nm long and separated from neighboring blockers by 50 nm. The ethanolamine blockers support keeping the ACE2 antibodies static in their places and prevent the adsorption of non-specific elements on the graphene surface [221]. The SARS-CoV-2 sample can be collected from human nasopharyngeal swabs and preserved in phosphate buffer saline (PBS) solution [222]. The PBS solution containing the SARS-CoV-2 S-proteins makes the sensing layer, which can flow over the sensor surface through a flow channel as an analyte [221]. In this work, the PBS sensing layer volume is set to 100 μL and 200 μL to investigate the sensor performances. We note that the PBS is neutral to SARS-CoV-2 S-protein and often used for analyzing proteins [223].

The proposed graphene SPR sensor is built on a semi-infinite borosilicate crown-glass 7 (BK7) prism material, as shown as the bottom layer in Fig. 4.1. The light is incident on the multi-layer structure from the prism side, and the reflected light is recorded on the same side. The incident light excites surface plasmon polaritons (SPPs) at the metal–dielectric, i.e., metal–multi-layer interface. The excitation of plasmonic modes is sensitive to the thickness of the metal layer. In this work, we use

a 46-nm-thick Ag layer as this thickness produces a peak in the SPP excitation [91]. For SPR, Ag is preferred to other metals, such as Au or copper (Cu), as it shows dense plasmonic interaction with light at low loss [224]. The scattering cross-section of Ag is greater than other metal choices [225]. Besides, Ag offers a narrower SPR spectrum than other metals, which is essential for plasmonic biosensors.

The multi-layer 2-D structure interfaces with the metal layer with WS_2 . To date, MoS_2 has been commonly used for such planar plasmonic structures. MoS_2 and WS_2 belong to the same family of chemical characteristics. However, WS_2 is more stable than MoS_2 , especially at high temperatures [226]. Additionally, WS_2 effectively absorbs more light than MoS_2 or other transition metal dichalcogenide (TMD) materials [124, 227]. Therefore, when interfaced with Ag, WS_2 helps decrease the incident light's reflection.

In the proposed structure, a $KNbO_3$ layer follows the WS_2 layer. $KNbO_3$ has a high optical permittivity that enhances the density of electric flux within the sensor [228]. Additionally, the imaginary part of the refractive index of $KNbO_3$ is zero. Hence, $KNbO_3$ increases light confinement without incurring losses. The layer that follows $KNbO_3$ is a phosphorene family material BP or BlueP. The BP or BlueP layer is sandwiched between $KNbO_3$ and graphene. The sensitivity of the proposed sensor increases significantly as BP and BlueP have a high real part of the refractive index, and hence enhance light confinement [111].

Using several 2-D materials in the proposed structure will increase the fabrication complexity slightly. However, the fabrication of various 2-D materials is usually cheap nowadays. In addition, the significant performance enhancement from the proposed sensor justifies for using different 2-D materials at a reasonable cost increase.

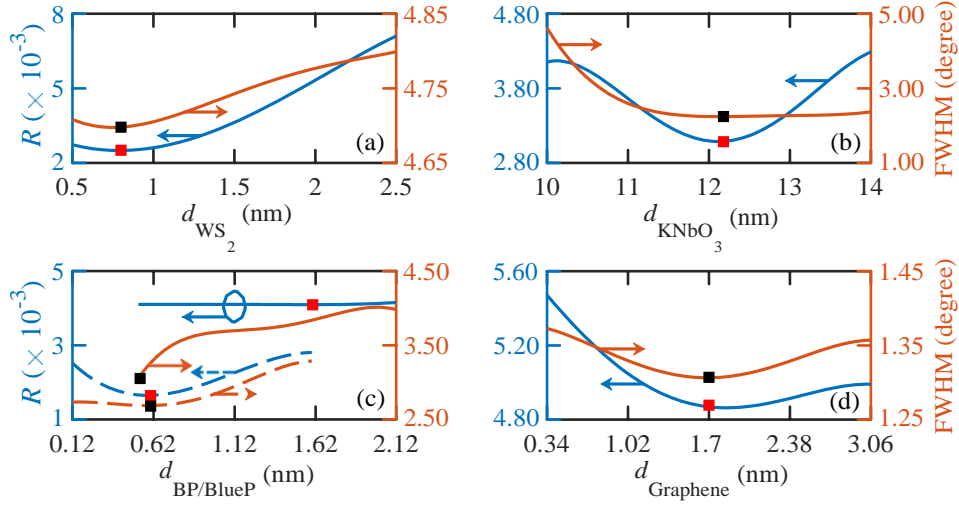


Figure 4.2: Reflectance (R) of plasmonic structure in Kretschmann configuration against layer thicknesses of (a) WS_2 , (b) KNbO_3 , (c) BP (solid) and BlueP (dashed), and (d) Graphene.

4.2.2 Optimization of Layer Thicknesses

The proposed graphene SPR sensor has several layers, with each having an essential effect on the overall performance. However, to get the best response from the proposed sensor, appropriate optimization of layer thicknesses is critical. Here, we have optimized the layer thicknesses of the proposed sensor using the approach discussed in Refs. [229] and [137]. In particular, we examine the effect of each layer thickness on the reflected light intensity (R) profile as a function of the incidence angle (ϑ_i). The optimization of layer thicknesses depends on the minimum reflected light intensity (R_{\min}) and full-width at half-maximum (FWHM) of the R -profile. While the light absorption is maximum on the sensor surface at R_{\min} , the FWHM represents the loss in the metal layer. Therefore, both R_{\min} and FWHM are crucial for the sensitivity enhancement of a sensor, and an optimized layer thickness should produce both R_{\min} and FWHM as small as possible.

The layer thicknesses are optimized sequentially. First, the layer thickness of WS_2 is optimized, and then that of KNbO_3 , BP, and graphene. To optimize the layer thicknesses, we change each layer thickness while the thicknesses of all other layers

are fixed. We optimize the WS_2 layer thickness from calculations, as shown in Figure 4.2(a). We find that when $\text{WS}_2 = 0.8$ nm, then both R_{\min} and FWHM show minimum values. Furthermore, the increase of the WS_2 thickness (d_{WS_2}) broadens the FWHM of R -profiles as R_{\min} value increases. Therefore, we set $d_{\text{WS}_2} = 0.8$ nm for the proposed sensor structure. Subsequently, we calculate the effects of KNbO_3 keeping d_{WS_2} at the optimized value. We determine R_{\min} and FWHM values when the thickness of KNbO_3 (d_{KNbO_3}) is varied from 10 nm to 14 nm, as shown in Figure 4.2(b). In this case, both R_{\min} and FWHM are minimum when $d_{\text{KNbO}_3} = 12.2$ nm.

Following a similar procedure, we optimize d_{BP} and d_{BlueP} when d_{Ag} , d_{WS_2} , and d_{KNbO_3} are at their optimized values. We show the change in R and FWHM with d_{BP} and d_{BlueP} in Fig. 4.2(c). We note that, initially, R decreases very minutely with d_{BP} and is minimum at $d_{\text{BP}} = 1.59$ nm. However, R increases when $d_{\text{BP}} > 1.59$ nm. By contrast, FWHM always increases with d_{BP} and is minimum when $d_{\text{BP}} = 0.53$ nm, which is BP mono-layer thickness. We find that when d_{BP} increases from 0.53 nm to 1.59 nm, R_{\min} decreases by 0.52% whereas FWHM increases by 16.66%. A narrow FWHM of the R -profile is required for high signal-to-noise ratio (SNR) and accuracy of ϑ_r detection [230]. Therefore, $d_{\text{BP}} = 0.53$ nm is set for the proposed structure. We note that R decreases initially with d_{BlueP} and is minimum at $d_{\text{BlueP}} = 0.615$ nm. However, R increases when $d_{\text{BlueP}} > 0.615$ nm. The thickness of a BlueP single layer is 0.123 nm [231]. Therefore, 0.615 nm represents five layers of BlueP. On the other hand, FWHM decreases slightly and becomes minimum at $d_{\text{BlueP}} = 0.615$ nm. Therefore, we set $d_{\text{BlueP}} = 0.615$ nm for the proposed structure.

The change of graphene layer thickness changes the wave-vector of SPs, which eventually changes ϑ_r . In Fig. 4.2(d), we show that as d_{Graphene} increases, both R and FWHM decrease since the confinement of the incident light at the metal–dielectric interface enhances [46]. When d_{Graphene} increases from mono-layer, i.e., 0.34 nm to five layers, i.e., 1.70 nm, R decreases by 12.93% as the absorption of incident light increased. However, R_{\min} and FWHM both increase when $d_{\text{Graphene}} > 1.70$ nm [46]. Therefore, we use $d_{\text{Graphene}} = 1.70$ nm in the proposed sensor.

Table 4.1: Refractive indices and thicknesses of the proposed sensor layers.

Material	Refractive index	Thickness (nm)	Reference
BK7	1.515	semi-infinite	[46]
Ag	Real: 0.055 Imag: 4.285	46	[174]
WS ₂	Real: 4.90 Imag: 0.3124	0.8	[232]
KNbO ₃	2.165	12.20	[233]
BP	Real: 3.50 Imag: 0.01	0.53	[234]
BlueP	Real: 2.1666 Imag: 0.1005	0.615	[235]
Graphene	Real: 3.0 Imag: 1.1419	1.70	[40]
PBASE	1.74	1.13	[221]
Blocker	1.4539	3.23	[220]
ACE2	1.13	2.10	[219]
Sensing layer	1.3348	100	[223]

4.3 Modeling and Simulation

4.3.1 Optical Properties

Optical properties of the layer materials of the proposed graphene SPR sensor are dispersive. Therefore, the response of the sensor depends on the incident light's wavelength. Here, the proposed sensor has been designed for an incident wavelength of 633 nm, which is frequently used in experiments [173]. The wavelength-dependent refractive index of the BK7 prism layer is determined using the expression presented in Ref. [46]. Furthermore, we have calculated the refractive index of Ag using the Drude-Lorentz model [174].

The wavelength-dependent refractive index of WS₂ has been calculated using [232]

$$n_{\text{WS}_2} = \frac{1}{2} \left[N + \frac{\delta}{\alpha} \pm \sqrt{\left(N + \frac{\delta}{\alpha} \right)^2 - 4n_0^2 n_{\text{sub}}^2} \right] \quad (4.1)$$

where $N = n_0^2 + n_{\text{sub}}^2$, n_0 and n_{sub} are the refractive indices of air and substrate, respectively. The parameter δ is the fractional change of the complex reflection ratio, and α is defined as

$$\alpha = 4ik_0 d_{\text{WS}} \frac{n_0 n_{\text{sub}}^2 \cos \vartheta_i \sin^2 \vartheta_i}{(n_0^2 - n_{\text{sub}}^2) [n_{\text{sub}}^2 - n_0^2 + N \cos(2\vartheta_i)]} \quad (4.2)$$

where $k_0 = 2\pi/\lambda$ and λ is the operating wavelength. The refractive index of KNbO₃ depends on λ according to the following expression [233]

$$n_{\text{KNbO}_3} = \frac{4.4222 + \frac{0.09972}{\lambda^2 - 0.05496} - 0.01976\lambda^2}{\lambda^2 - 0.05496} \quad (4.3)$$

We have used the refractive index of BP, as reported in Ref. [234]. Furthermore, the refractive index of graphene has been calculated by [40]

$$n_{\text{Graphene}} = 3 + i \frac{C_G}{3} \lambda, \quad (4.4)$$

where C_G is a constant with a value of $5.44 \mu\text{m}^{-1}$ [236]. The calculated refractive indices for BK7, Ag, WS₂, KNbO₃, BP, and graphene are given in Table 4.1. On the other hand, the indices of PBASE, ACE2, blocker, and PBS solution of the proposed sensor are obtained from literature and also given in Table 4.1.

The index of the sensing layer (n_s) varies when SARS-CoV-2 S-protein binds to ACE2 antibodies in the PBS layer according to [237]

$$n_s = n + \beta D, \quad (4.5)$$

where n is the index of the PBS solution, β is the index progress coefficient with a value of $\sim 0.186 \text{ cm}^3/\text{gm}$ for PBS [238, 239], and D is the mass density of S-protein in gram per deciliter. We calculate D using the following expression [91]

$$D = C \times M, \quad (4.6)$$

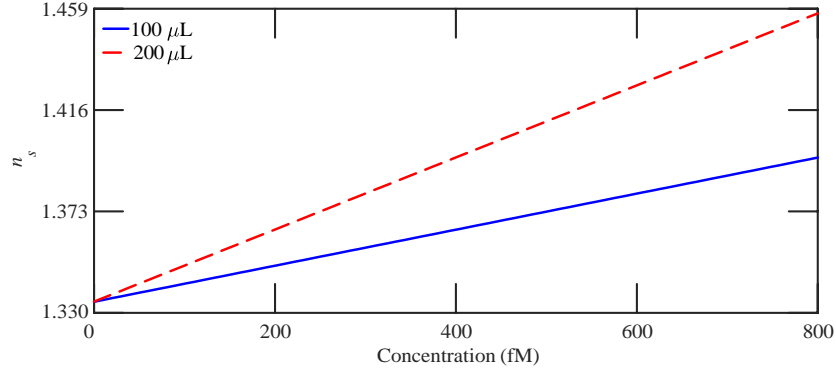


Figure 4.3: Sensing layer refractive index (n_s) vs. SARS-CoV-2 S-protein concentration for 100- μL and 200- μL PBS solutions.

where C is the S-protein molar concentration in the PBS solution, and M is the S-protein molecular weight, which is 180 kDa or $180 \times 2.5875 \times 10^{-19}$ gm [218, 240]. We can write $1 \text{ fM} = 1 \times 10^{-15} \text{ gm} \times 411.04 \text{ gm/L}$, or $= 4.1104 \times 10^{-12} \text{ gm/dL}$. Also, 1 fM dissolved in $100 \mu\text{L}$ PBS solution is equivalent to $4.1104 \times 10^{-12} \times 100 \times 10^{-6} \text{ gm/dL}$. Therefore, $D = 4.1104 \times 10^{-12} \times 100 \times 10^{-6} / 10^{-15} \text{ gm/dL} \simeq 0.041104 \text{ gm/dL}$ for $100 \mu\text{L}$ PBS solution. Then $n_s = 0.041104 \times 0.00186 + 1.3348 \simeq 1.33485$ for 1 fM S-protein concentration in $100 \mu\text{L}$ PBS saline. A similar procedure is applied for $200 \mu\text{L}$ PBS solution to determine the n_s for S-protein concentration.

In this work, we consider $100\text{-}\mu\text{L}$ and $200\text{-}\mu\text{L}$ PBS in the sensing layer separately, where the molar mass of PBS is 411.04 gm/L . We vary the SARS-CoV-2 S-protein concentration from zero to 800 fM in the PBS solution. The sensing layer refractive index n_s , due to the inclusion of the SARS-CoV-2 S-protein, is calculated using Eqs. (4.5) and (4.6) and presented in Fig. 4.3. When the S-protein concentration is zero, the refractive index of the sensing layer is 1.3348 , which increases linearly as the S-protein concentration increases. We note that $200\text{-}\mu\text{L}$ PBS shows a higher n_s than that of $100\text{-}\mu\text{L}$ PBS as the mass density of S-protein increases with the PBS solution volume.

4.3.2 Calculation of the Reflection Profile

To find the R -profile of the proposed sensor due to SPR, we solve 2-D full-field Maxwell's equations using the FDTD method. In the numerical analysis, we vary ϑ_i . We consider the proposed structure, as shown in Fig. 4.1, an N -layer system and apply the TMM with the actual layer thicknesses of the sensor structure [46]. The R of the N -layer system for a transverse magnetic (TM)-polarized incident wave is given by [186]

$$R = \frac{(M_{11} + M_{12}q_N)q_1 - (M_{21} + M_{22}q_N)}{(M_{11} + M_{12}q_N)q_1 + (M_{21} + M_{22}q_N)} \quad (4.7)$$

where M is the characteristic matrix of the N -layer structure and M_{ij} is given by

$$M_{ij} = \prod_{k=2}^N M_k \quad (4.8)$$

In Eq. (8), i, j are positive integers, and

$$M_k = \begin{pmatrix} \cos \theta_k & -i \sin \theta_k / q_k \\ -iq_k \sin \theta_k & \cos \theta_k \end{pmatrix}, \quad (4.9a)$$

$$q_k = \frac{(\epsilon_k - n_1^2 \sin^2 \vartheta_i)^{1/2}}{\epsilon_k}, \quad (4.9b)$$

$$\theta_k = d_k \frac{2\pi}{\lambda} (\epsilon_k - n_1^2 \sin^2 \vartheta_i)^{1/2}, \quad (4.9c)$$

where n_1 is the prism index, d_k is the thickness of the k -th layer, ϵ_k is the dielectric constant of the k -th layer, and k is an integer varying from 2 to $N - 1$.

4.3.3 Sensor Performance Parameters

The sensitivity (S) and FoM are the main performance parameters of SPR based sensors. These parameters are determined using the R -profile. The sensitivity is defined as the ratio of $\Delta\vartheta_r$ and Δn_s [187]

$$S = \frac{\Delta\vartheta_r}{\Delta n_s}, \quad (4.10)$$

where $\Delta\vartheta_r$ is the change in resonance angle ϑ_r for Δn_s change in n_s . On the other hand, FoM is defined as [188]

$$\text{FoM} = \frac{S}{\Delta\vartheta_{i,(1/2)}}, \quad (4.11)$$

where $\Delta\vartheta_{i,(1/2)}$ is the full-width of ϑ_i at the half-maximum points on the R -profile.

4.3.4 Simulation Method

In this work, we use 2-D FDTD simulations to calculate the interaction of the incident light with the sensor structure. The simulation area is 1600 nm in the x -direction and 1000 nm in the y -direction. We apply a non-uniform meshing technique with ultra-fine mesh grids in the FDTD simulations to limit the overall error to $< 0.05\%$. Furthermore, the simulation boundaries in the x -direction are terminated by perfectly matched layers (PML), while Bloch boundaries terminate those in the y -direction.

The incident light has a 633-nm wavelength and TM polarization. The incidence angle ϑ_i must be greater than the critical angle (ϑ_c) for total internal reflection. The total light absorption of the sensor is $A = 1 - T - R$, where T is the transmission coefficient. Here, as the incident light will experience an attenuated total reflection, $T = 0$. Therefore, we can write, $A = 1 - R$. When SPs are excited at the resonance incident angle, R drops sharply. In this work, we vary ϑ_i from 55° to 85° , with a

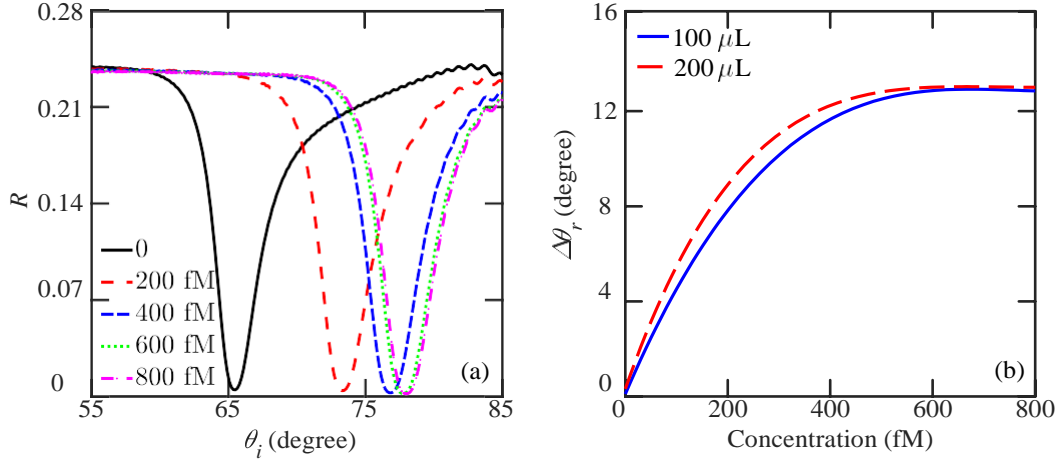


Figure 4.4: (a) R -profile of the proposed graphene SPR sensor for different SARS-CoV-2 S-protein concentrations as a function of ϑ_i . In this case, SARS-CoV-2 S-proteins are added to 100- μL PBS solution. (b) $\Delta\vartheta_r$ against SARS-CoV-2 S-protein concentration for 100- μL and 200- μL PBS solution.

step size of 0.099° to calculate the R -profile for mass level S-protein concentrations. Additionally, for ultra low-level SARS-CoV-2 detection, we vary ϑ_i from 65.30° to 65.60° , with a step size of 0.00149° . The incident light source is located at 750 nm from the BK7–Ag interface, whereas the reflected light intensity is recorded at 775 nm from the same interface.

4.4 Results and Discussion

4.4.1 Detection Approach and Limit of Detection

As the concentration of the SARS-CoV-2 S-protein in PBS changes, the sensing layer experiences a difference in the refractive index. Consequently, the index variation alters the SP wave-vector, which eventually changes ϑ_r . Figure 4.4(a) shows R -profiles of the proposed sensor as a function of ϑ_i for different SARS-CoV-2 S-protein concentrations. We note that when the sensing layer contains only the PBS, without any SARS-CoV-2 S-protein, ϑ_r is 65.44° . The change of R -profile depends on the

refractive indices of the buffer layer, such as the PBS, and the target molecule, such as the S-protein concentration. We note that when the S-protein concentration is 1 fM, ϑ_r shifts to 65.445° and 65.450° for 100- μL or 200- μL PBS, respectively. Thus, the change in ϑ_r , i.e., $\Delta\vartheta_r$, is 0.005° and 0.01° when 1 fM SARS-CoV-2 S-protein is present in 100- μL and 200- μL PBS, respectively, as shown in Figure 4.4(b). While ϑ_r changes significantly with the S-protein concentration, R_{\min} decreases slightly due to the enhanced absorption of the incident light.

Figure 4.4(b) shows $\Delta\vartheta_r = \vartheta_{r(\text{PBS+ACE2+S-protein})} - \vartheta_{r(\text{PBS+ACE2})}$ calculated from the R -profiles as the S-protein concentration varies for 100- and 200- μL PBS solutions. We note that $\Delta\vartheta_r$ increases significantly with the S-protein concentration. However, $\Delta\vartheta_r$ does not vary noticeably when S-protein concentration is ≥ 600 fM in 100- μL PBS solution, as shown in Fig. 4.4(b). Similarly, $\Delta\vartheta_r$ shows a saturating behavior when the S-protein concentration is ≥ 500 fM in 200- μL PBS solution. Therefore, the maximum ϑ_r shifts are $\Delta\vartheta_{r(\text{max})} = 12.56^\circ$ and 12.72° for 100- μL or 200- μL PBS solutions, respectively.

To detect the SARS-CoV-2 S-protein, $\Delta\vartheta_r$ values are used. As S-proteins incrementally adsorb to the sensor surface, ϑ_r keeps on shifting to greater values until it reaches the maximum value [241]. S-proteins are detected when $\Delta\vartheta_r > 0$. Now, LoD is determined from the minimum S-protein concentration for which a non-zero $\Delta\vartheta_r$ is registered. The proposed sensor shows $\Delta\vartheta_r > 0$ even when the SARS-CoV-2 S-protein concentration is only 1 fM, enabling the proposed sensor detect as low as 1 fM SARS-Cov-2 S-protein. The LoD of a sensor is an essential parameter, especially when detecting a critical pathogen like SARS-CoV-2. In Table 4.2, we compare the LoD of the proposed sensor with some recently proposed sensors that use plasmonic techniques to detect the SARS-CoV-2 S-protein. The proposed sensor shows a much smaller LoD than that reported by these state-of-the-art sensors. We note that the plasmonic metasensor of Ref. [87] shows an LoD of ~ 4.2 fM, relatively close to that obtained from the proposed sensor. However, the metasensor operates in the THz

Table 4.2: Comparisons of LoD of the proposed sensor with different recently proposed sensors for SARS-CoV-2 S-protein detection.

Sensor device	Assay components	LoD
MRT-PCR [242]	SARS-CoV-2	5 μM
dd-PCR [243]	SARS-CoV-2	0.00187 ng
RT-LAMP [244]	SARS-CoV-2	0.025 $\mu\text{g}/\mu\text{l}$
FET biosensor [88]	SARS-CoV-2	1 fg/ml
Meta-sensor [87]	Au-NPs, SARS-CoV-2	~ 4.2 fM
PPT biosensor [78]	Au-NPs, SARS-CoV-2	0.22 pM
NIR biosensor [77]	SARS-CoV-2	~ 301.67 nM
LSPR biosensor [245]	Au-nano-spikes	~ 0.5 pM
This work	SARS-CoV-2	1 fM

range, and therefore, is bulky. The metasensor also does not work for the entire range of the S-protein concentration.

4.4.2 Sensor Resolution and Binding Affinity

In Fig. 4.5(a), we show the proposed sensor's resolution (SR) as a function of the S-protein concentration. The resolution of a sensor can be determined by [246]

$$\text{SR} = \Delta n_s \frac{\Delta \vartheta_{r(\min)}}{\Delta \vartheta_{r(\max)}}, \quad (4.12)$$

where $\Delta \vartheta_{r(\min)}$ is the minimum spectrum resolution, and $\Delta \vartheta_{r(\max)}$ is the maximum ϑ_r shift, respectively. We note that the maximum SR is 0.25×10^{-5} RIU when S-protein concentration is 800 fM for 100- μL PBS solution. When S-protein concentration is 1 fM, the SR is 0.015×10^{-5} RIU and 0.016×10^{-5} RIU for 100- μL and 200- μL and PBS solutions, respectively. The SR of the proposed sensor signifies its ability to detect SARS-CoV-2 S-protein in minute index variations such as on the order of 10^{-5} RIU, which is significant compared to the recently reported SR values in literature [246–248].

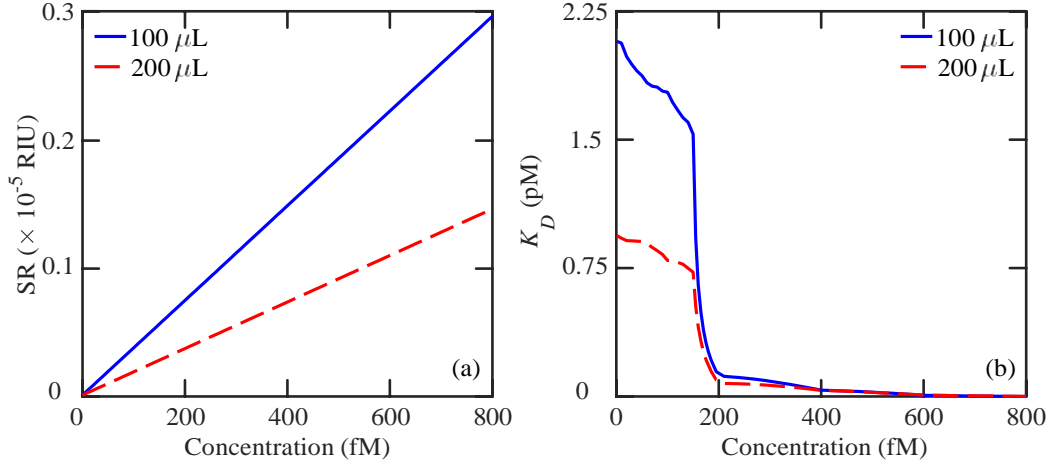


Figure 4.5: (a) SR and (b) K_D as a function of S-protein concentration of the proposed graphene SPR sensor for 100- μ L and 200- μ L PBS solutions.

In an SPR sensor, typically a flow channel is used to inject aqueous solution to the sensor surface [249]. In our proposed sensor, the PBS solution containing SARS-CoV-2 can be injected into the channel to detect the S-protein where ACE2 is immobilized on the graphene surface. S-proteins must bind to ACE2 antibodies so that the gathering of proteins on the sensor surface changes the refractive index of the sensing layer. The binding between the immobilized ACE2 and S-protein is denoted by the association constant (K_A) or the dissociation constant (K_D), where $K_D = 1/K_A$. We can derive an expression for K_D using the Langmuir model [84]

$$K_D = C \frac{\Delta\vartheta_{r(\max)}}{\Delta\vartheta_r} - 1 \quad (4.13)$$

Langmuir model is a ligand binding model to justify the affinity of analyte-antibody bindings [250]. Generally, the K_D value for proteins on an SPR sensor is < 10 nM [251]. The K_D value should be as small as possible because a smaller K_D value represents a greater binding affinity of the sensor to its target element. Figure 4.5(b) shows K_D of the proposed sensor as a function of the S-protein concentration. We note that the binding affinity between ACE2 and S-protein increases with the S-protein concentration. The K_D value is smaller with the 200- μ L PBS solution

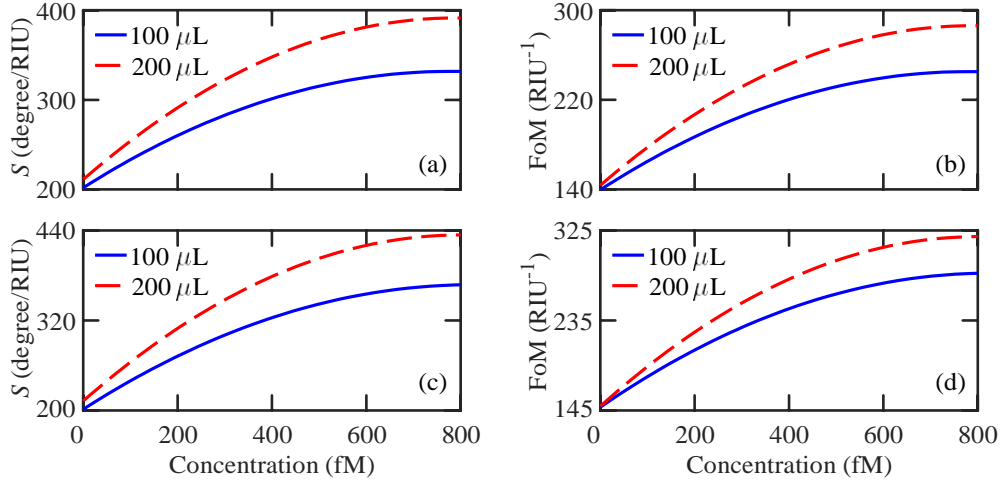


Figure 4.6: (a) S and (b) FoM using BP and (c) S and (d) FoM using BlueP as a function of S-protein concentration of the proposed graphene SPR sensor for 100- μL and 200- μL PBS solutions.

than that with the 100- μL PBS solution due to the increasing number of S-proteins in greater PBS volume enhancing the chances of binding between ACE2 and S-proteins. We note that the proposed sensor shows a smaller K_D value compared to recent reports on k_D values in literature [251].

4.4.3 Sensing Performance

The selectivity of the proposed graphene SPR SARS-CoV-2 sensor can be determined from the change in ϑ_r as the S-protein concentration changes [84]. In Fig. 4.4(b), we have shown the $\Delta\vartheta_r$ for different S-protein concentrations for two different PBS solutions. When the S-protein concentration is $\gtrsim 1$ fM, $\Delta\vartheta_r$ increases with the S-protein concentration. Furthermore, $\Delta\vartheta_r$ is more significant for the 200- μL PBS solution. Therefore, the proposed SARS-CoV-2 sensor has an affinity toward S-proteins [91]. As $\Delta\vartheta_r$ sensitively changes with the S-protein concentration, the proposed sensor is highly selective of SARS-CoV-2. The proposed SARS-CoV-2 sensor shows comparatively greater selectivity compared to recent reports in literature [84, 160, 252].

Figure 4.6(a) shows the sensitivity of the proposed graphene SPR sensor as a function of the SARS-CoV-2 S-protein concentration. As the sensitivity depends on the change of ϑ_r and increasing S-protein concentration shows a greater variation of ϑ_r , we find that the sensitivity increases as S-protein concentration increases. Also, the 200- μL PBS solution shows a greater sensitivity than that of the 100- μL PBS solution because the S-protein number increases with PBS solution volume, which increases $\Delta\vartheta_r$. When the S-protein concentration is 1 fM, $S = 201$ degree/RIU and 210 degree/RIU for 100- μL and 200- μL PBS solutions, respectively. Furthermore, the proposed sensor shows the maximum sensitivity of 371 degree/RIU when the S-protein concentration is 800 fM for 200- μL PBS solution.

The FoM of the proposed sensor has been presented in Fig. 4.6(b) as a function of the S-protein concentration. We note that FoM increases with the increase of S-protein concentration. When the S-protein concentration is 800 fM, the FoM is maximum with values of 233 RIU^{-1} and 275 RIU^{-1} for 100- μL and 200- μL PBS solutions, respectively. Moreover, 1 fM S-protein concentration shows 140 RIU^{-1} and 148 RIU^{-1} FoM for 100- μL and 200- μL PBS solutions, respectively. As the increasing S-protein concentration raises the n_s value, ϑ_r increases. Moreover, as the FoM is directly related to the sensitivity according to Eq. (4.11), it increases when the sensitivity increases.

Figure 4.6(c) shows the sensitivity of the proposed graphene SPR sensor as a function of the SARS-CoV-2 S-protein concentration using BlueP instead of BP. The sensitivity increases as S-protein concentration increases. The sensitivity with BlueP is comparable to that with BP at the ultra-low-level concentration of the S-protein. However, when the S-protein concentration increases, the sensor with BlueP shows greater sensitivity than the sensor with BP. When the S-protein concentration is 800 fM, the sensitivity is 365 degree/RIU and 435 degree/RIU for 100- μL and 200- μL PBS solution, respectively, for the sensor with BlueP, $\sim 10\%$ greater than the sensor with BP.

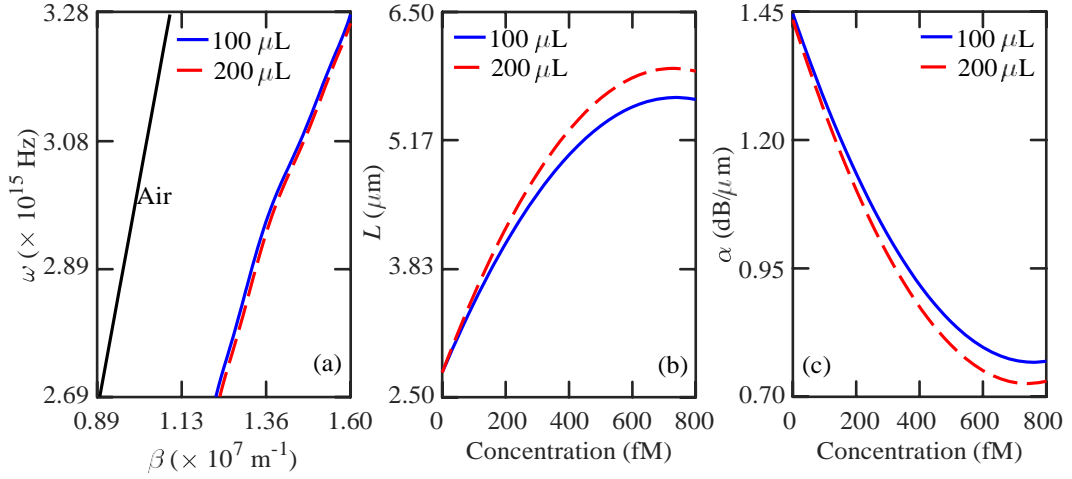


Figure 4.7: (a) Dispersion relations of the proposed sensor when S-protein concentration is 1 fM using BP. The most left straight line is the light line, (b) Propagation length, and (c) Propagation loss of the proposed sensor as a function of SARS-CoV-2 S-protein concentration for 100 μ L and 200 μ L PBS solutions.

Figure 4.6(d) shows the FoM as a function of the SARS-CoV-2 S-protein concentration using BlueP instead of BP. BlueP shows greater FoM than BP for ultra-low-level and mass-level S-protein concentrations. For example, when the S-protein concentration is 1 fM, FoMs are 152 RIU $^{-1}$ and 153 RIU $^{-1}$ FoM for 100- μ L and 200- μ L PBS solutions for the sensor with BP, \approx 4% greater than the sensor with BP. Furthermore, when the S-protein concentration is 800 fM, FoMs are 282 RIU $^{-1}$ and 318 RIU $^{-1}$ for 100- μ L and 200- μ L PBS solutions for the sensor with BlueP, >15% greater than the sensor with BP. The enhancement in FoM with the BlueP can be attributed to the narrower R spectrum than BP.

As the proposed sensor has several layers of different refractive indices, calculating the dispersion relation is numerically challenging. In this work, we analyze the dispersion relations using the radiative mode [253]. The in-plane wave-vector can be given by [253]

$$\beta = \frac{\omega \sqrt{\epsilon_{\text{prism}}}}{c} \sin \vartheta_r, \quad (4.14)$$

where ϵ_{prism} is the dielectric constant of the prism, ω is the angular wavelength, and c is the speed of light in vacuum. Figure 4.7(a) shows the dispersion relations of the

proposed sensor. We compute the reflectivity of the proposed sensor as a function of frequency and ϑ_i . Frequency is varied from 4.2827×10^{14} Hz to 5.2138×10^{14} Hz and ϑ_i is varied from 55° to 85° . We find that the dispersion curve moves away from the air light line. We note that after 630 nm wavelength ($\omega = 2.9 \times 10^{15}$ Hz), dispersion relations for both 100 μL and 200 μL move farther from the light line.

On the other hand, SPPs suffer damping in metal, decreasing the propagation length significantly [14]. Mainly, damping depends on the dielectric constant of metal at the oscillation frequency of SPPs. Losses may also occur due to the coupling of SPPs to radiation modes. Propagation loss also depends on the sensing layer's dielectric constant [254]. The propagation length can be defined by [255]

$$L = \frac{1}{\Delta\vartheta} \frac{1}{n_{i,(1/2)} \frac{\omega}{c} \cos\vartheta_r}, \quad (4.15)$$

where n_p is the refractive index of the prism. Also, the propagation loss can be calculated by [255]

$$\alpha = [-10\log(1/e)]/L \approx 4.343/L. \quad (4.16)$$

Figure 4.7(b) shows that the propagation length increases with SARS-CoV-2 S protein concentrations. Also, the 200 μm PBS solution shows a greater propagation length than the 100 μm PBS solution since the sensing layer's refractive index increases with concentration, enhancing the light confinement. Our proposed sensor shows a small propagation length $<10 \mu\text{m}$, which is short-range SPPs. As a result, the propagation loss decreases, as shown in Fig. 4.7(c). Moreover, when propagation length increases from 2.62 μm to 5.84 μm , the propagation loss decreases from 1.44 dB/ μm to 0.72 dB/ μm for 200 μm PBS solution. Compared to existing literature, our proposed sensor performs better in propagation length and loss [255].

We note that the proposed sensor's sensitivity and FoM performances are significantly better compared to that of the state-of-the-art optical sensors. We compare the sensitivity and FoM of the proposed graphene SPR sensor in Table 4.3 with

Table 4.3: Performance comparison of our proposed sensor with different recently proposed sensors.

Sensor configuration	S (degree/RIU)	FoM (RIU ⁻¹)
Graphene/2-D materials [256]	98	88.89
Graphene/ZnO/BaTiO ₃ [257]	157	71
Graphene/PtSe ₂ [258]	154	–
Graphene/PtSe ₂ [259]	162	15
Graphene/WSe ₂ [260]	164	–
This work (BP/BlueP)	210/210	148/153

some recently reported sensors. We have compared the minimum sensitivity and FoM achievable from the proposed sensor at the LoD with those reported in literature, as given in Table 4.3. We note that we have considered sensors that use similar 2-D materials. The compared sensors also operate at 633 nm incident wavelength and report results for a sample of index ~ 1.3349 , which is the n_s at 1 fM S-protein concentration for 200- μ L PBS solution in this work.

4.5 Conclusion

Tackling the COVID 19 pandemic requires rapid, low-cost and sensitive detection of ultra low-level SARS-CoV-2. The sensor proposed in this work will detect SARS-CoV-2 in real-time without requiring any label or complicated sample preparation. The proposed sensor works using the principle of SPR angle shift. The angle shifts obtained from the proposed sensor are significant when the SARS-CoV-2 concentration changes even at the femtomolar level, demonstrating suitability for sensitive detection of ultra-low concentration. Furthermore, the proposed sensor can detect as small as 1 fM SARS-Cov-2 sample, making it suitable for early detection of COVID 19. The obtained LoD is much smaller than the presently available techniques. The analysis of the proposed sensor presented here is computational. An experimental justification of these results is important, which is out of the scope of this work. However, such auspicious findings of this work confirm that the proposed sensor

is appropriate for SARS-CoV-2 S-protein detection and may find applications in detecting other biochemical and biological analytes.

CHAPTER 5

ANISOTROPIC GPCS-BASED TP AND SP HYBRID MODES FOR HEMOGLOBIN DETECTION

We propose graphene-photonic-crystals (GPCs) based Tamm plasmons (TPs) and surface plasmons (SPs) hybrid mode for the detection of hemoglobin (Hb) level. The in-plane anisotropic property of GPCs, the proposed sensor shows polarization-dependent performances. The reflection profile shows two visible reflectivity minimum which is determined by transfer matrix based angular interrogation method. These reflection minimums are basically excitation of TPs and SPs hybrid mode. The TPs resonance mode offer high figure-of-merit (FoM) to detect the Hb as compared to the SPs resonance mode. We also observe the energy transfer from TPs mode to SPs mode by using Fourier mode spectral analysis, which essentially enhances the sensitivity. Increasing the sensitivity without grating-based sensor structure, we propose double-dips method where the maximum sensitivity is 314.5 degree/RIU and FoM is 1746 RIU⁻¹ (TPs-based) and 486 RIU⁻¹ (SPs-based), respectively when Hb level is 189 g/L. The proposed GPCs based sensor offers possible applications for the detection of bio-molecules with high sensitivity and FoM.

5.1 Introduction

In surface plasmon resonance (SPR), transverse magnetic (TM) surface wave is propagated between dielectric and metal interface. Such SPR resonances show wider reflected light intensity (R)-profile due to scatter and absorption losses in the noble metal [89]. Therefore, these types of optical sensor limit for further development. Instead, the light absorption of mono-layer graphene is 2.3% which is good enough for a 0.34 nm layer thickness. However, to reach a competent light matter interaction this is not sufficient for optical sensing and optical modulation [90]. As an alternative, increasing graphene layers on the metal film enhanced the sensitivity of the SPR sensors. Nevertheless, the full-width-at-half-maximum (FWHM) of the R -profile widen when increasing the number of graphene layers [162]. As a result, wider R -profile of graphene limits its applications as a two-dimensional (2-D) material in the plasmonic sensors [49].

Different research groups have been proposed graphene-photonic-crystals (GPCs) based sensor structure to increase the light-graphene interaction [63, 89, 261–265]. GPCs generally known as an artificial periodic array structure which is formed by graphene and dielectrics as well photonic-crystals (PCs) is a form of photonics device created through intermittent preparation of various dielectric layers with dissimilar refractive index [266]. Also, several layers of dielectrics on graphene mono-layer is stacked and these types of structures have been explored both theory and experiment [53, 54]. Graphene mono-layer in GPCs can enhance the photon absorption by Bragg fluctuation as well as enhances the light-graphene interaction [49]. GPCs are very suitable for a vast area of sensing due to fast response time and ultrahigh sensitivity [55]. Also, the electro-magnetic waves propagation in GPCs can control by photonic band-gap (PGB) [56].

GPCs based structures have vast applications area such as optical modulator, polarizer, filter, and biosensor [267]. On the other hand, surface plasmons (SPs) can be excited in GPCs with high degree of photon absorption [267] though problem

of scatter SPs mode in GPCs is observed which can be controlled by doping [57]. Moreover, GPCs show properties of hyperbolic meta-materials such as Tamm plasmons (TPs), critical coupling and negative refraction [58–60]. TPs are basically surface mode that excites at the metal and distribute Bragg reflector (DBR) based interface [61]. The optical field of TPs decay in the DBR alone with the metal layer [61]. TPs can stimulate directly by TM or transverse electric (TE) polarized light and there is no need of dispersion regulation like SPs [62]. Also, the *R*-profile of TPs is comparatively very thin than SPs [63]. Moreover, TPs have low absorption loss and high quality factor which is very appropriate for optical modulation and detection [268, 269]. Moreover, high quality factor improves the detection accuracy and signal-to-noise ratio.

When metal layer is deposited on a prism material and GPCs is used, a hybrid TPs-SPs mode are excited [64]. However, these hybrid modes are excited on different interfaces on metal and GPCs (TPs) and on metal and sensing layer interface (SPs). As a result, anti-crossing effect is observed on their dispersion relation [64]. The anti-crossing effect alters the dispersion properties of the hybrid TPs-SPs plasmonic mode and decreases the absorption losses of SPR. Therefore, the *R*-profile of TPs and SPs become narrower compared with the traditional SPR. Actually, the anti-crossing effect shows a coupling state between TPs and SPs and exchanges energy from TPs mode to SPs mode [270].

Recently, different research groups have been proposed TPs based refractive index and temperature sensor [63, 65, 66]. A graphene-porous silicon PCs is proposed where figure-of-merit (FoM) and sensitivity control by varying different parameters like incident angles, porosity's, and thicknesses of silicon layers [67]. Also, asymmetric graphene-DBR is used to create TPs mode and the effect of TM-polarization and TE-polarization on sensor performances are investigated [68]. Moreover, a different refractive index sensor contains GPCs is proposed with defect layer [63]. However, the propose refractive index sensor is polarization and phase in-sensitive. Alternatively, a terahertz (THz) refractive index sensor of graphene-DBR is proposed

where sensor performances are phase and polarization dependent [69]. In references [63, 67–69] both of these types of sensors operated in THz region. However, using THz frequency has some limitations such as difficult to detect the complex molecules due to non-ionizing behavior and low photonic energy radiation [70, 71]. Besides, to improve the performances of optical sensor in the optical wavelength region, TPs mode can be combined with SPs mode [271].

Hemoglobin (Hb) is very important part of blood and found in the red blood cell (RBC). The oxygen supplies in the tissue depend on Hb levels and variations of Hb levels causes various diseases [72, 73]. Normal blood Hb levels are 120 g/L to 160 g/L for female and 140 g/L to 180 g/L for male [75]. Moreover, blood Hb level increases 6.1025 g/L when change of refractive index is 0.001 refractive index unit (RIU). Determine Hb level from RBC, heparin has been widely applied where pre-processing is essential [74]. However, heparin-based detection suffers measurement error. A whispering gallery-based method is used to detect the Hb level. Nonetheless, the sensitivity of this sensor is low [75]. Recently, a graphene based SPR sensor have been proposed for Hg detection [74]. Nevertheless, there are no information of detection accuracy and also sensitivity is fluctuated when Hb level is increased.

In this chapter, we propose a GPCs based TPs and SPs hybrid mode for Hb detection in visible wavelength region. We have optimized the silver (Ag) thickness and number of unit cell (N) of GPCs based on R minimum and FWHM. Also, the energy transfers from TPs mode to SPs mode is determined by Fourier mode spectral analysis (FMSA). We also show the anti-crossing effect between TPs and SPs for different polarization angle (φ) using transfer matrix method (TMM). Moreover, the optical properties of Hb in blood is calculated by Barer analytical model. The sensor performances especially the change of resonance angle ($\Delta\vartheta_r$) and FWHM for both the TPs mode and SPs mode are calculated using TMM based angular interrogation method. In addition, double-dips method (DDM) is applied to determine the sensitivity (S) and FoM. The proposed sensor shows energy exchanges from TPs mode to SPs mode which ultimately improves the sensitivity for Hb detection. Moreover, we

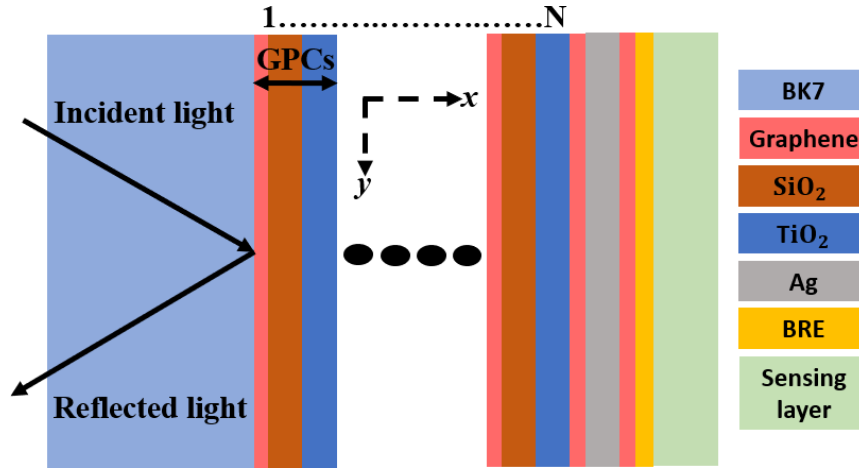


Figure 5.1: Schematic of the proposed anisotropic GPCs based TPs and SPs hybrid mode Hb detection sensor.

show the effect of TPs resonance on sensing and found that TPs have momentous impact on sensing particularly the high FoM.

The rest of this chapter is arranged as follows: In Section 5.2, we present and discuss the GPCs based sensor structure and optimization. Moreover, we discuss the anti-crossing effect between TPs mode and SPs mode and also the simulation approaches. For simulation models, we followed to solve the Maxwell equations using finite difference time domain (FDTD) technique. In Section 5.3, we express the analytical models that we applied to investigate the optical properties of different materials. Moreover, determination of R -profile, TPs resonance mode identification and energy transfer from TPs to SPs are discussed here. In addition, we present the proposed GPCs based sensor performance parameters in Section 5.3. We show and discuss the calculated sensor performances in Section 5.4. Besides, in Section 5.5, we present the conclusions on the findings.

5.2 Proposed Sensor

5.2.1 Configuration

The schematic of the proposed anisotropic GPCs based TPs and SPs hybrid mode Hb detection sensor is shown in Fig. 5.1. We use BK7 as a prism material. On the top of the prism, graphene-based PCs are stacked. Single GPC is formed by graphene/SiO₂/TiO₂, respectively. This GPC like structure is also similar to the DBR structure [272]. The thickness of graphene, SiO₂, and TiO₂ are 1.02 nm, 110 nm, and 70 nm, separately. The thickness of SiO₂, and TiO₂ are calculated by $d_s = \lambda/4n_s$ and $d_t = \lambda/4n_t$, respectively where λ is the operating wavelength, n_s is refractive index of SiO₂ and n_t is refractive index of TiO₂ [63].

Moreover, total thickness of single unit GPC is 181.02 nm. Graphene mono-layer thickness (t_g) is 0.34 nm. Here, we take $3t_g$ graphene layer. The SiO₂ and TiO₂ layers are chosen for wide PGB due to big differences of refractive index of SiO₂ and TiO₂ [89]. We also consider GPCs is a periodic structure where total number of periods is N . We have set $N = 9$ (optimized) as these periods support minimum R value. On the top of the last period, we have set another graphene layer whose thickness is also $3t_g$ as a termination layer. Termination layer supports the transfer of surface mode dispersion by the photonic bands from one graphene layer to the other and reduce the scatter of SPs mode [273]. Furthermore, graphene termination layer avoids the oxidation of silver (Ag) layer [274]. Followed by graphene termination layer, we set Ag layer and thickness of Ag (d_{Ag}) is 60 nm (optimized). The d_{Ag} controls the strength of interaction between TPs mode and SPs mode in the sensing layer and therefore, play important role in the mode coupling [66].

As Hb is a bio-marker of several diseases, then fast and sensitive Hb detection is very important. To detect Hb in human blood, we use a bio-recognition element (BRE) such as antibody enzyme complex (AEC) [275]. The BRE will be located on the top of the sensor surface which is another graphene layer on Ag. The thickness of this

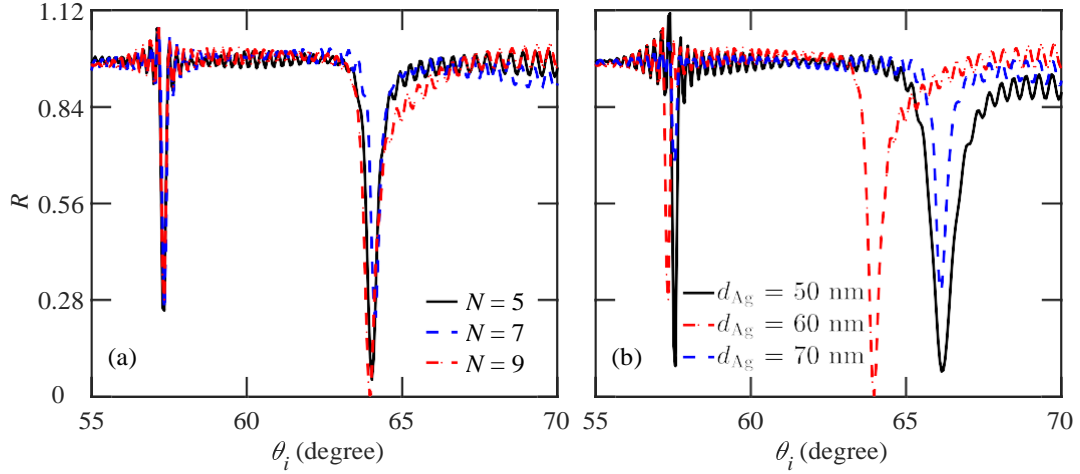


Figure 5.2: R -profile of the GPCs based proposed sensor as a function of ϑ_i when $n_{Hb} = 1.32919$ (a) Varying the number of GPCs unit N , and (b) Different thicknesses of Ag layer.

graphene layer is also $3t_g$ nm. Moreover, this graphene layer reduces the chance of Ag oxidation. Practically, we will need binding Hb to immobilize antibodies on the graphene surface. As graphene has such rich π - π structure which can immobilize the antibodies like AEC. On the other hand, AEC is an auspicious sensing element due to its capability to capture specific bio-molecules where its catalytic action produces signals. The thickness of anti-body layer such as AEC is 20 nm.

Nowadays, AECs have been made-up by genetic fusion, protein ligation, or chemical conjugation [276–278]. These techniques have some limitations such as genetic fusion suffers insoluble aggregates, chemical conjugation shows creation of unfavorable disulfide bonds, and protein ligation method exhibits several lysine residues on their surfaces. As a result, we use AECs which will be fabricated by Spy-Catcher (SC) or Spy-Tag (ST) system [279]. SC or ST can be created by immuno-globulin collagen adhesion domain-2 (CnaB2) of the fibronectin adhesion protein (FbaB) through streptococcus pyogenes [275]. The human blood serum contains the Hb as a sensing element which can flow on the top of the sensor surface by a flow channel [221].

5.2.2 Optimization of Sensor Structure

The proposed GPCs based Hb detection sensor has several layers. However, metal such as Ag and number of unit cell (N) have critical effect on the overall sensor performance. Nevertheless, to get the best response from the proposed sensor, suitable optimization of sensor structural parameters are crucial. We have optimized d_{Ag} of the proposed sensor using the approach discussed in Ref. [229]. In particular, we examine the effect of d_{Ag} and variation of N of the R -profile as a function of the incidence angle (ϑ_i). The optimization of d_{Ag} and N depend on the minimum reflected light intensity (R_{min}) and FWHM of the R -profile. While the light absorption is maximum on the sensor surface at R_{min} , the FWHM represents the loss in the metal layer. Therefore, both R_{min} and FWHM are crucial for the sensitivity enhancement of a sensor, and an optimized layer thickness and N should produce both R_{min} and FWHM as small as possible. Moreover, we consider both of the two resonance such as TPs mode and SPs mode when optimizing d_{Ag} and N .

To optimize the N , we vary the N while the other sensor structural parameters such as layers thicknesses are fixed. Here, we use sensing layer refractive index ($n_{Hb} = 1.32919$) and $d_{Ag} = 60$ nm. We optimize N from calculations, as shown in Fig. 5.2(a). We find that when $N = 9$, then both R_{min} and FWHM show minimum values for SPs. However, TPs show minimum value when $N = 5$. Furthermore, when $N = 7$, the R value is not minimum for both of these two resonances. We note that increasing N from 5 to 9, R_{min} of TPs increase from 0.2498 to 0.2818 i.e., absorption of incident light decreases. As well as R_{min} of SPs decreases 0.0490 to 0.00288 i.e., absorption of incident light increases. We note that when $N = 9$, we get the R_{min} value for SPs resonance mode. Therefore, we are not increasing the number of N of the proposed sensor.

Next, we optimize the d_{Ag} , we change d_{Ag} while the other layers thicknesses are fixed and number of unit cell is $N = 9$. We optimize d_{Ag} from calculations, as shown in Fig. 5.2(b). We find that when $d_{Ag} = 60$ nm, then both R_{min} and FWHM show

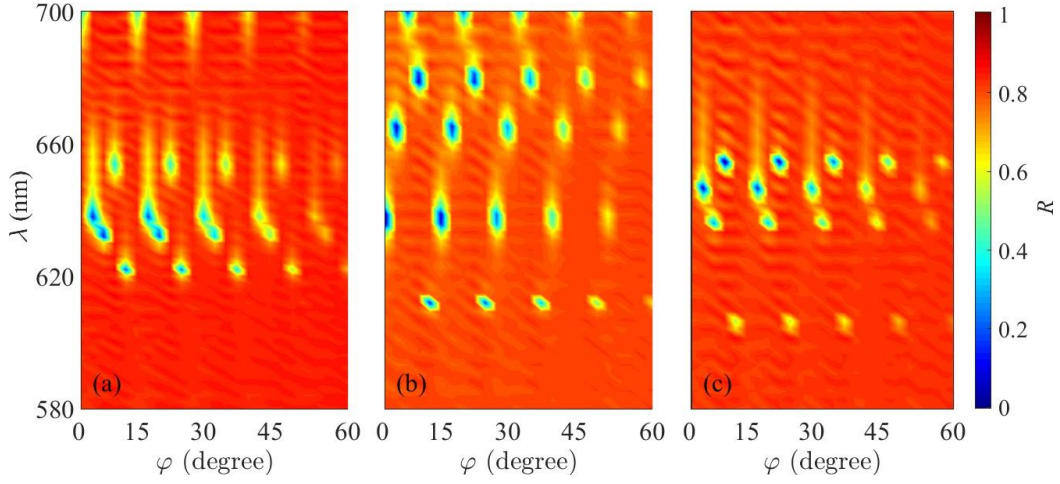


Figure 5.3: R -profile of the GPCs based proposed sensor as a function of polarization angle when $n_{\text{Hb}} = 1.32919$ (a) $d_{\text{Ag}} = 50$ nm, (b) $d_{\text{Ag}} = 60$ nm, and (c) $d_{\text{Ag}} = 70$ nm.

minimum values for SPs. However, TPs show minimum value when $d_{\text{Ag}} = 50$ nm. Increasing d_{Ag} from 50 nm to 60 nm, the FWHM is thinner for both SPs and TPs mode. Furthermore, when $d_{\text{Ag}} = 70$ nm, the R value is not minimum for both of these two resonances. We note that increasing d_{Ag} from 50 nm to 60 nm, R_{min} of TPs increase from 0.088 to 0.2818 i.e., absorption of incident light decreases in TPs resonance. As well as R_{min} of SPs decreases 0.076 to 0.00288 i.e., absorption of incident light increases in SPs resonance.

5.2.3 Anti-crossing Effect

Using the anti-crossing effect, the energy band can be altered and splitting between the TPs and SPs part as the hybrid mode corresponds to their coupling strengths [280]. The change of gap positions between the SPs and TPs mode showing by the R minimum and hence, the broadening or thinning of the R -profile indicates the alterations of the coupling strength. Coupling between TPs and SPs lead to disgust of their dispersion profile which is also depend on metal thickness [64]. Likewise, the

excitation of the TPs-SPs based hybrid mode depends on total internal reflection (TIR) conditions and these modes are polarization-sensitive [89].

We use the R -profile to show the coupling between TPs and SPs where d_{Ag} can play important role. Numerical analysis is shown in Fig. 5.3(a), 5.3(b), and 5.3(c) when d_{Ag} are 50 nm, 60 nm, and 70 nm, respectively. When $d_{Ag} = 50$ nm as shown in Fig. 5.3(a), there is very little splitting between SPs and TPs hybrid mode and spectral repulsion is very small and about 2 nm at $\varphi = 0^\circ$. SPs and TPs hybrid mode overlap and not sense each other significantly. Similar tendency is observed when we increase the value of φ . However, increasing φ the value of R increases which may degrades the sensor performances.

In Fig. 5.3(b), when $d_{Ag} = 60$ nm the spectral repulsion is 30 nm at $\varphi = 0^\circ$. Therefore, a minimum gap is observed which repulse the SPs from TPs and moving the SPs far away from the Ag layer. Also, minimum R value is observed which indicates the thinner of R -profile. Thus, enhances the sensor performances. However, increasing the value of φ , the R value increases which indicates small absorption of incident light on GPCs based sensor. As a result, the sensor performances decreases. In Fig. 5.3(c), we show that the spectral repulsion is 8 nm at $\varphi = 0^\circ$ when $d_{Ag} = 70$ nm. The spectral gap decreases when d_{Ag} increases from 60 nm to 70 nm. We note from Ref. [64] that when metal thickness is > 60 nm, SPs and TPs again not very well sense each other due to weak inter-modal interaction [281]. Consequently, using $d_{Ag} = 70$ nm in the proposed GPCs based sensor reduces the sensor performances. As usual, $d_{Ag} = 70$ nm is also shown the dependence of φ .

5.2.4 Simulation Method

In this work, we apply 2-D FDTD simulations to analyze the interaction of the sensor structure with the incident light. The simulation area is 9000×1000 nm², i.e., 9000 nm in the x -direction and 1000 nm in the y -direction. Moreover, we use perfectly

matched layers (PML) boundary condition in the x -direction while Bloch boundary condition in the y -direction. We find the solutions for 2-D structures as the proposed GPCs Hb detection sensor is unvarying in the z -direction. We use a non-uniform meshing technique with ultra-fine mesh grids in the FDTD simulations to limit the overall error to $< 0.05\%$. Also, we have set a high mesh accuracy and used 1000 fs simulation time for the simulation method. We have used either a TM-polarized or a TE-polarized light source with 633-nm wavelength using oblique incidence. This is due to light absorption of GPCs enhance by eight times from normal incidence to oblique incidence [282]. To determine the R -profile, we vary the incidence angle from 55° to 70° with step size 0.0427° . The light source is placed in BK7 region at 4250 nm from BK7-graphene interface. Also, we have recorded the R value and this monitor is located in BK7 at 4400 nm from the same interface.

5.3 Modeling of the Proposed Sensor

5.3.1 Optical Properties

Optical properties of the different layers of the proposed GPCs based Hb sensor are dispersive. As a result, the interaction of light with sensor structure depends on the incident light wavelength. We have used incident wavelength of 633 nm for the proposed sensor because it is normally used in experiments [173]. The wavelength dependent refractive index of the BK7 prism layer is calculated using the following expression [46]

$$n_{\text{BK7}} = \frac{1.03961212\lambda^2}{\lambda^2 - 0.0060006986} + \frac{0.231792344\lambda^2}{\lambda^2 - 0.0200179144} + \frac{1.039612\lambda^2}{\lambda^2 - 103.560653} + 1 \quad (5.1)$$

As, graphene is an optically anisotropic uni-axial material due to its 2-D behavior, its permittivity (ϵ_g) tensor is determined by [283]

$$\epsilon_g = \begin{pmatrix} \epsilon_{g,t} & 0 & 0 \\ 0 & \epsilon_{g,t} & 0 \\ 0 & 0 & \epsilon_{g,n} \end{pmatrix} \quad (5.2)$$

where $\epsilon_{g,n} = 1$ (normal part of graphene permittivity), because electric field of normal incidence cannot stimulate any current in the graphene sheet [283]. However, graphene permittivity ($\epsilon_{g,t}$)(tangential part) is defined as [284]

$$\epsilon_{g,t} = 1 + i \frac{\sigma(\omega)}{\omega \epsilon_0 t_g} \quad (5.3)$$

where $\sigma(\omega)$ is the conductivity of mono-layer graphene, ω is the angular frequency of the incident wave, and ϵ_0 is the permittivity of free space. Mono-layer graphene $\sigma(\omega)$ fundamentally depends on Kubo formula [179]

$$\sigma(\omega) = i \frac{e^2 k_B T}{\pi \hbar^2 (\omega + i\tau^{-1})} \frac{E_f}{k_B T} - \frac{E_f}{i \frac{4\pi \hbar}{\ln 2} \frac{\exp \left(\frac{k_B T}{\hbar (\omega + i\tau^{-1})} \right) + |E_f|}{2 |E_f| + \hbar (\omega + i\tau^{-1})}} \quad (5.4)$$

where k_B is the Boltzmann constant, E_f is the Fermi energy, e is the charge, T is the temperature, \hbar is the reduced Planck constant, and τ is the relaxation time of carriers. Here, we use $E_f = 0.65$ eV, and $T = 300$ K. To model graphene $\sigma(\omega)$, phenomenological scattering rate (Γ) is used in FDTD based method. We use $\Gamma = 0.00051423$ eV where $\tau = 1/2\Gamma$ [285]. The dispersion relation of anisotropic graphene can be expressed by [286]

$$k_x^2 + k_y^2 = \epsilon_{g,t} k_0^2 \text{ for (TE)} \quad (5.5)$$

$$\frac{k_x^2}{\epsilon_{g,t}} + \frac{k_y^2}{\epsilon_{g,t}} = k_0^2 \text{ for (TM)} \quad (5.6)$$

where $k_0 = 2\pi/\lambda$. For TE-polarization, $k_{ix} = \sqrt{k_0^2 \epsilon_i - k_{iy}^2}$, $k_{iy} = k_y = k_0 \sin \vartheta_i$ is the tangential part of the wave-vector of each layer related to the incidence light [287]. ϵ_i is the actually $\epsilon_{g,n}$, ϵ_S , and ϵ_T for the graphene, SiO₂, and TiO₂, respectively. For TM-polarization, the wave-vector of graphene, SiO₂, and TiO₂ are $k_{gx} = \sqrt{k_0^2 \epsilon_{g,t} - k_{gx}^2}$, $k_{sx} = \sqrt{k_0^2 \epsilon_S - k_{iy}^2}$, and $k_{tx} = \sqrt{k_0^2 \epsilon_T - k_{iy}^2}$, respectively where $\epsilon_{g,n} = 1$. We note that for TE-polarization, R -profile depends on $\epsilon_{g,t}$ and not requires the tilting of ϑ_i [288]. However, TM-polarization based R -profile depends on both $\epsilon_{g,t}$, and $\epsilon_{g,n}$ and requires the obliquity of incidence angle. Consequently, GPCs based proposed structure shows isotropic behavior for normal incidence. Alternatively, due to the obliquity of incidence light the proposed GPCs based sensor shows anisotropic behavior.

The refractive index of SiO₂ and TiO₂ are 1.45702 and 2.30, respectively and obtained from the literature [289, 290]. Refractive index of Ag is determined by the Drude-Lorentz model of Ref. [174]. We use AEC as an anti-body which is modelled by FbaB while its refractive index is 1.45 and collected from Ref. [291]. Finally, we set the sensing layer refractive index. Human blood refractive index for Hb varies from 1.32919 to 1.36019 and the Hb level grows 6.1025 g/L for every 0.001 RIU variations in the blood [75]. Therefore, the sensing layer refractive index i.e., refractive index of Hb in blood sample is determined by Barer model [292]

$$n_{\text{Hb}} = n_0 + C\Delta\lambda \quad (5.7)$$

where n_0 is the present refractive index, C is the constant or refraction increment of protein defined as 0.00276 nm, and $\Delta\lambda$ is the change of resonance wavelength. Moreover, a relation is present between the Hb level variations with n_{Hb} which can be obtained from the Ref. [74]

$$H_r = H_0 + A\Delta n \quad (5.8)$$

where H_0 is the present Hb level in g/L, H_r is the final Hb level in g/L, A is a constant which value is 6102.50, and $\Delta n = 0.001$ is the change of refractive index.

5.3.2 Calculation of the R -Profile

To find the R -profile of the proposed GPCs based sensor due to TPs and SPs resonance mode, we use 2-D full-field Maxwell's equations using the FDTD method. In the numerical analysis, we vary ϑ_i . We consider the proposed structure, as shown in Fig. 5.1, as a multi-layer structure and apply the TMM with the actual layer thicknesses of the sensor structure [46]. The R of the multi-layer system for an oblique incident wave is given by [186]

$$R = \frac{(M_{11} + M_{12}q_N)q_1 - (M_{21} + M_{22}q_N)}{(M_{11} + M_{12}q_N)q_1 + (M_{21} + M_{22}q_N)} \quad (5.9)$$

where M is the characteristic matrix of the multi-layer structure and M_{ij} is given by

$$M_{ij} = \begin{matrix} \begin{matrix} \vdots \\ \vdots \\ \vdots \\ \vdots \\ \vdots \end{matrix} \\ \begin{matrix} M_k \\ \vdots \\ \vdots \\ \vdots \\ \vdots \end{matrix} \\ \begin{matrix} \vdots \\ \vdots \\ \vdots \\ \vdots \\ \vdots \end{matrix} \\ ij \end{matrix} \quad (5.10)$$

In Eq. (5.10), i, j are positive integers, and

$$M_k = \begin{pmatrix} \cos \theta_k & -i \sin \theta_k / q_k \\ -iq_k \sin \theta_k & \cos \theta_k \end{pmatrix}, \quad (5.11a)$$

$$q_k = \frac{(\epsilon_k - n_{\text{BK7}}^2 \sin^2 \vartheta_i)^{1/2}}{\epsilon_k}, \quad (5.11b)$$

$$\theta_k = d_k \frac{2\pi}{\lambda} (\epsilon_k - n_{\text{BK7}}^2 \sin^2 \vartheta_i)^{1/2}, \quad (5.11c)$$

where d_k is the thickness of the k -th layer, ϵ_k is the dielectric constant of the k -th layer, and k is an integer varying from second to multi-layer. For TM and TE

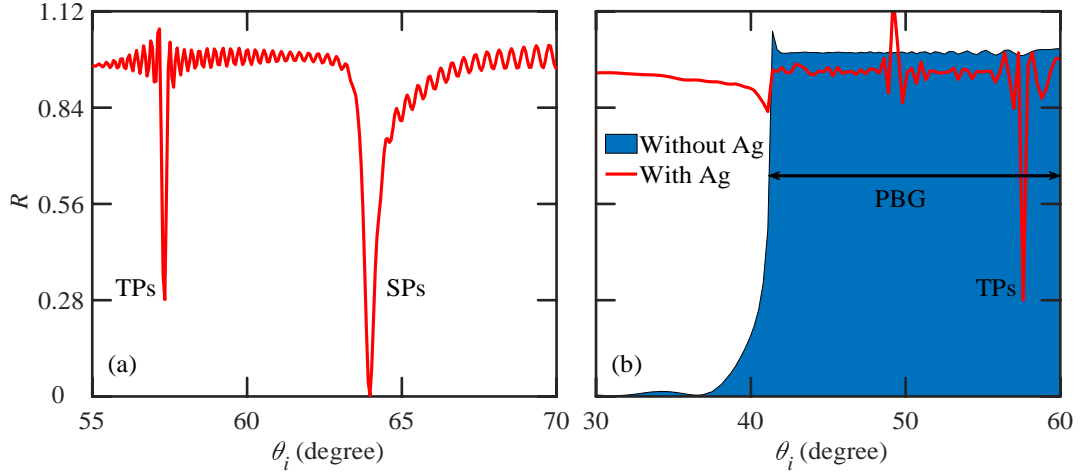


Figure 5.4: (a) R -profile of the proposed GPCs based TPs and SPs hybrid mode when $N = 9$, $n_{\text{HB}} = 1.32919$, and $d_{\text{Ag}} = 60$ nm, and (b) R -profile of the proposed GPCs based sensor using the similar sensor parameters with or without the Ag layer. The solid red line lies within the PBG at 57.52° indicates the excitation of TPs resonance mode.

polarization, R -profile can be calculated by [264]

$$R_{\text{TM}} = |R_{\text{TM}}| \exp(i\varphi_{\text{TM}}) \quad (5.12)$$

$$R_{\text{TE}} = |R_{\text{TE}}| \exp(i\varphi_{\text{TE}}) \quad (5.13)$$

In this analysis, we use $\varphi_{\text{TM}} = 0^\circ$ for TM-polarization and $\varphi_{\text{TE}} = 30^\circ$ or 60° for TE-polarization. Practically, we can use Mach–Zehnder interferometer approach to determine the TM or TE-polarization based R -profile [264].

5.3.3 TPs and SPs Analysis

TPs mode is electromagnetic wave which can excite at the interface between a metal layer and a DBR due to consecutive reflections [69]. In our proposed sensor, TPs create between interface of Ag and GPCs. TPs dispersion curve lies within the light line and thus it can be excited by oblique as well as normal incident wave [293]. We have used TMM to analyze the spectral behavior of layered structure such as

GPCs-based sensor. Here, magnetic and electric field part in various layers of such structures is determined by using matrix operation [69]. When TPs excites, we can write [294]

$$R_M R_{GPCs} = 1 \quad (5.14)$$

where R_M and R_{GPCs} are the amplitude reflection coefficients of the metal and GPCs interface. It is noted that $R_M \simeq -1$ at visible wavelength then R_{GPCs} must be close to -1 [69]. As a result, TPs mode is confined between Ag (permittivity is negative real part) and GPCs band-gap. As the light is incidence on the sensor structure from the GPCs side as shown in Figure 5.1, the gathering of the energy in the TPs mode will make a dip in the R -profile [294]. Moreover, it is important to note that such GPCs based structure where Ag is present, TPs and SPs mode cannot be excited separately at a specific incidence angle [64]. There is a superposition of electromagnetic wave localize at the Ag-GPCs interface (TPs) whereas localize at the Ag-sensing layer interface (SPs) creating hybrid state.

In Fig. 5.4(a), we show the R -profile of the proposed GPCs based sensor structure where $n_{Hb} = 1.32919$, $N = 9$, $\varphi = 0^\circ$. We note that there are two distinct R minimum present. The first dip observes at 57.52° where the second dip at 63.96° . The first dip is TPs excited between Ag-GPCs interface and the second dip is SPs excited between Ag-sensing layer. If we consider the FWHM, TPs show 0.1708° whereas SPs show 0.4730° . We note that SPs mode show 64% widen of FWHM. Besides, there are number of ripples present in the R -profile which are insignificant photonic modes in the various GPCs layers.

In Fig. 5.4(b), we show the R -profile for two cases. In first case, we simulate the sensor structure (BK7-GPCs-Sensing layer) without using the Ag layer for determination of PBG [295]. The proposed structure without Ag show a PBG when ϑ_i varies from 41.1° to 60° . No excited mode is observed in this region. Next, we simulate the structure (BK7-GPCs-Ag-Graphene-Antibody-Sensing layer) with Ag layer. We observer a resonance dip at 57.52° . This resonance is actually a TPs resonance mode

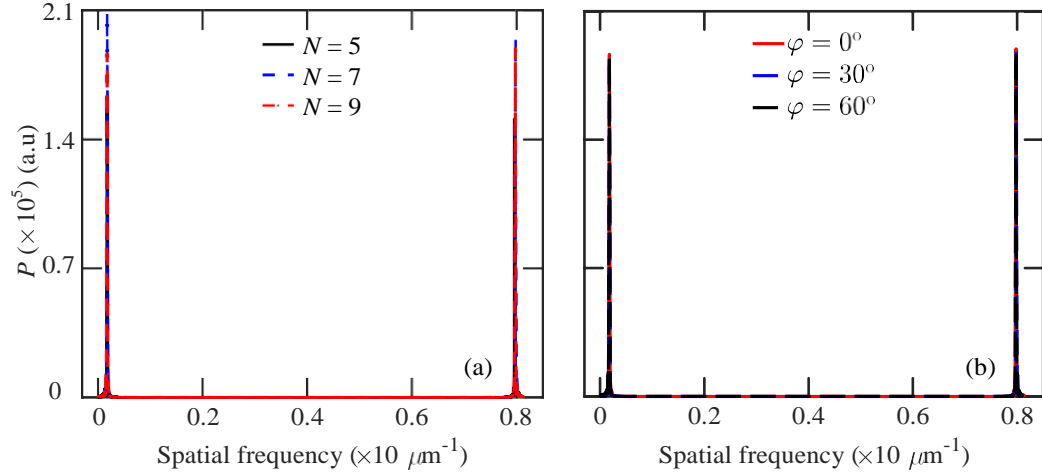


Figure 5.5: Fourier power spectrum as a function of spatial frequency when $n_{\text{Hb}} = 1.32919$, and $d_{\text{Ag}} = 60$ nm (a) Variation the number of unit N , and (b) Different polarization angle.

locate inside the PGB which creates by the interference of electromagnetic waves at the interface between the Ag and GPCs layers [271].

5.3.4 Effect of Energy Transfer

FMSA approach permits to examine the characteristics of each mode like spatial energy density profile and uncoupling of different scatters. We set an approach of how strongly energy transfer from TPs to SPs and couples to a particular mode [296]. In plasmonic-based devices, other modes in addition the SPs mode will be excited in the metal-dielectric structure. The main reason of using FMSA method is to crumble the individual modes. Electromagnetic field parts here in TM or TE polarization change to wave vector of space by a one-dimensional (1-D) fast Fourier transform (FFT). In Fig. 5.5(a), we present Fourier power profile with respect of spatial frequency by varying the N . In addition, we present the same analysis when φ changes to observe the φ -dependent energy transform from TPs to SPs as shown in Figure 5.5(b). We have used $n_{\text{Hb}} = 1.32919$ and $d_{\text{Ag}} = 60$ nm in this analysis.

Here, spatial frequency is plotted in the horizontal axis whereas the vertical axis records the SPs and TPs power.

In Fig. 5.5(a), we show two modes. The first mode at $0.0173 \mu\text{m}^{-1}$ represents the TPs mode whereas the second mode at $0.7983 \mu\text{m}^{-1}$ represents the SPs mode. We have theoretically calculated the spatial frequency and demonstrated that it is the SPs and TPs mode. For SPs mode, we use the wave-vector $k_{\text{SPs}} = k_0 \frac{q}{\frac{\epsilon_m \epsilon_{\text{Hb}}}{\epsilon_m + \epsilon_{\text{Hb}}}}$ and for TPs $k_{\text{TPs}} = k_0 \frac{q}{\epsilon_m \epsilon_{\text{eff}}}$ where ϵ_m is the real part permittivity of Ag and ϵ_{eff} is the effective permittivity of GPCs. In Fig. 5.5(a), when $N = 7$, TPs and SPs both modes show maximum power where TPs (208100 a.u) show better power than SPs (195200 a.u). Increasing N from 7 to 9, TPs power reduces from 208100 a.u to 186600 a.u whereas SPs power reduces from 195200 a.u to 189000 a.u. We note that when $N = 9$, SPs mode show maximum power compared to TPs. However, increasing N from 7 to 9, TPs energy reduction rate is 10.33% where SPs energy reduction rate is 3.18%. Actually, increasing N from 7 to 9, energy transfers from TPs mode to SPs mode.

In Fig. 5.5(b), we show the similar tendency as increasing φ where the power of both TPs and SPs modes are decreased. When $\varphi = 0^\circ$ then TPs show 186600 a.u whereas SPs show 189500 a.u. On the other hand, when $\varphi = 60^\circ$ then TPs show 160700 a.u and SPs show 147700 a.u. Therefore, decreasing φ the energy transfers from TPs mode to SPs mode. In the proposed sensor, our aim is to transfer energy from TPs to SPs. As the maximum energy of TPs is confined in the GPCs and near the Ag-GPCs interface then TPs electromagnetic fields barely relate with the outer sensor surface. So, the TPs mode features mostly its resonance angle (ϑ_r) is unresponsive to the changes of the refractive index of sensing medium [65].

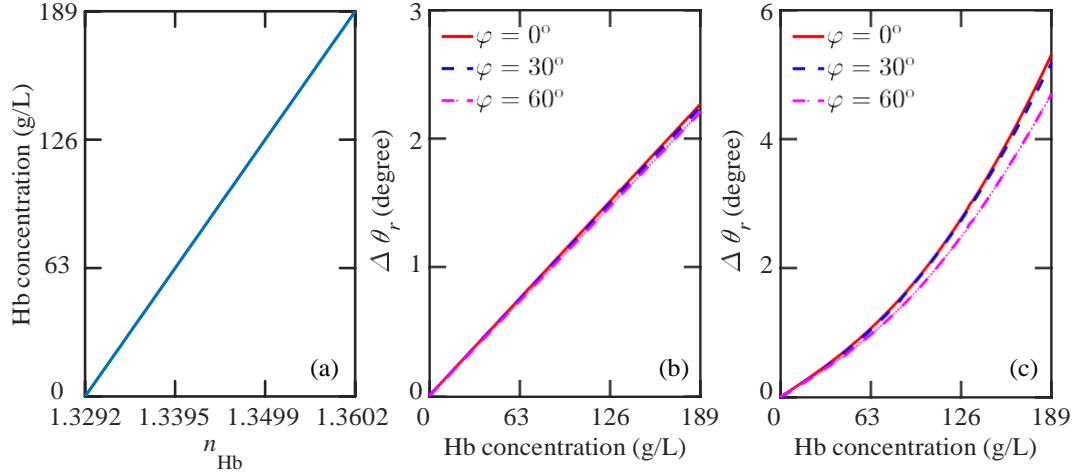


Figure 5.6: (a) Sensing layer refractive index vs. Hb concentration, (b) $\Delta\theta_r$ as a function of Hb concentration for TPs resonance mode, and (c) $\Delta\theta_r$ as a function of Hb concentration for SPs resonance mode.

5.3.5 Sensor Performance Parameters

The sensitivity and FoM are the main performance parameters of a GPCs based SPs and TPs mode resonance sensors. These parameters are determined using the R -profile. The sensitivity is defined as [187]

$$S_{\text{SPs/TPs}} = \frac{\Delta\vartheta_r(\text{SPs/TPs})}{\Delta n_{\text{Hb}}}, \quad (5.15)$$

where $\Delta\vartheta_r(\text{SPs/TPs})$ is the change in resonance angle of ϑ_r for either SPs or TPs mode. On the other hand, FoM is defined as [230]

$$\text{FoM}_{\text{SPs/TPs}} = \frac{S_{\text{SPs/TPs}}}{\text{FWHM}_{\text{SPs/TPs}}}, \quad (5.16)$$

5.4 Sensing Performance

In Figure 5.6(a), we show the Hb concentration as a function of sensing layer refractive index. We vary the Hb concentration from zero to 189 g/L. The sensing layer refractive index n_{Hb} , due to the inclusion of the Hb, is calculated using Eqs. (5.7) and (5.8). When the Hb concentration is zero, then $n_{\text{Hb}} = 1.32919$ which increases linearly as the Hb concentration increases. Moreover, when the Hb concentration is 189 g/L, then $n_{\text{Hb}} = 1.36019$. As the concentration of the Hb changes in human blood sample, the sensing layer experiences a difference in the refractive index i.e., change of $n_{\text{Hb}}(\Delta n_{\text{Hb}})$. Consequently, the index variation changes the SPs as well as TPs wave-vector, which ultimately changes the resonance angle ϑ_r for both TPs and SPs mode.

Figure 5.6(b) shows $\Delta\vartheta_r$ for TPs resonance mode as a function of Hb concentration level for different φ . We note that $\Delta\vartheta_r$ for TPs resonance mode increases with the Hb concentration. However, $\Delta\vartheta_r$ does not vary noticeably when φ changes from 0° to 30° . However, when φ changes from 0° to 60° then $\Delta\vartheta_r$ is little bit significant. In Figure 5.6(c), we show the similar tendency for SPs resonance mode. However, $\Delta\vartheta_r$ changes significantly compared to TPs resonance mode. We note that $\Delta\vartheta_r$ for SPs resonance mode is around 2 times higher than $\Delta\vartheta_r$ of TPs resonance mode i.e., $\Delta\vartheta_r(\text{SPs}) = 2 \times \Delta\vartheta_r(\text{TPs})$.

In Figure 5.7, we show the sensor performances as a function of Hb concentration by using TPs resonance mode independently. Moreover, we analysis the anisotropic behavior of the GPCs based sensor i.e., polarization dependent sensor performances. For anisotropic analysis, we use three different φ such as 0° , 30° , and 60° , respectively. Actually, 0° represents TM mode whereas 30° , and 60° show the sensor performances by TE mode. Figure 5.7(a) shows the sensitivity of the proposed GPCs based sensor as a function of Hb concentration. Considering TPs resonance mode, sensitivity increment is very minute depends on Hb concentration. As energy confinement of TPs is Ag-GPCs interface then TPs electromagnetic fields hardly

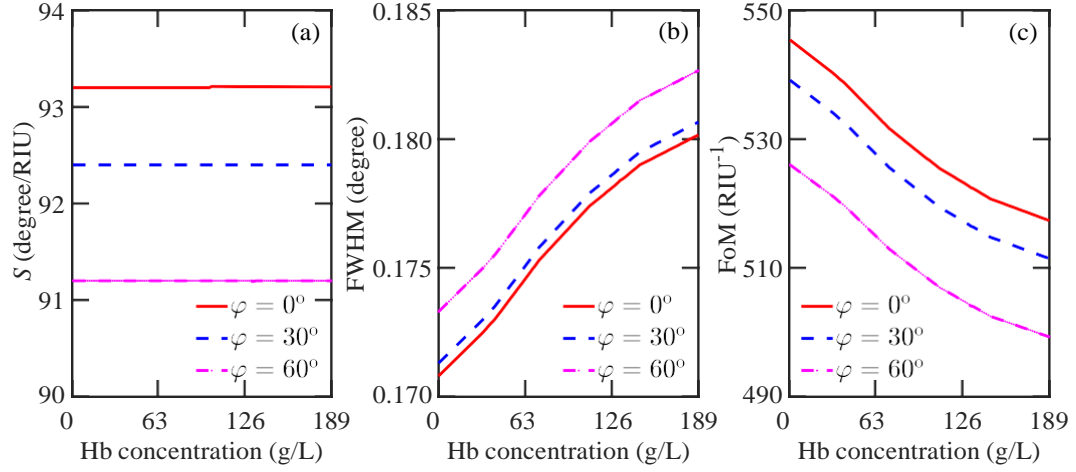


Figure 5.7: (a) S , (b) FWHM, and (c) FoM as a function of Hb concentration of the proposed GPCs based sensor using TPs resonance mode.

interact with the sensing element. Though, $\Delta\vartheta_r$ increments of TPs resonance is linear as shown in Fig. 5.6(b) but Δn_{Hb} is not as small to enhance the sensitivity. However, maximum sensitivity is observed when $\varphi = 0^\circ$ and increasing the value of φ sensitivity decreases steadily, as increasing φ , $\Delta\vartheta_r$ reduces gradually as shown in Fig. 5.6(b). Therefore, we note that TPs mode show low polarization-dependent sensitivity.

In Fig. 5.7(b), we show the FWHM of the proposed GPCs based sensor as a function of Hb concentration for different φ for TPs resonance mode. Increasing Hb concentration or φ , the FWHM increases. This is because the R -profile is broadened when Hb concentration increases or φ increases. However, the value of FWHM is quite satisfactory as compared with the FWHM of SPs mode. In Fig. 5.7(c), we show the FoM of the proposed sensor for TPs resonance mode. Generally, FoM decreases when Hb concentration increases or φ increases. However, when $\varphi = 0^\circ$ and Hb concentration is zero, then FoM is maximum and this value is 545 RIU^{-1} . The value of FoM gradually decreases when Hb concentration increase and 517 RIU^{-1} when Hb concentration is 189 g/L . As the increasing Hb concentration raises the n_{Hb} value, $\Delta\vartheta_r$ increases. However, the FWHM increases as Hb concentration increases then FoM decreases. Similar tendency is observed when $\varphi = 30^\circ$ or $\varphi = 60^\circ$. However, FoM

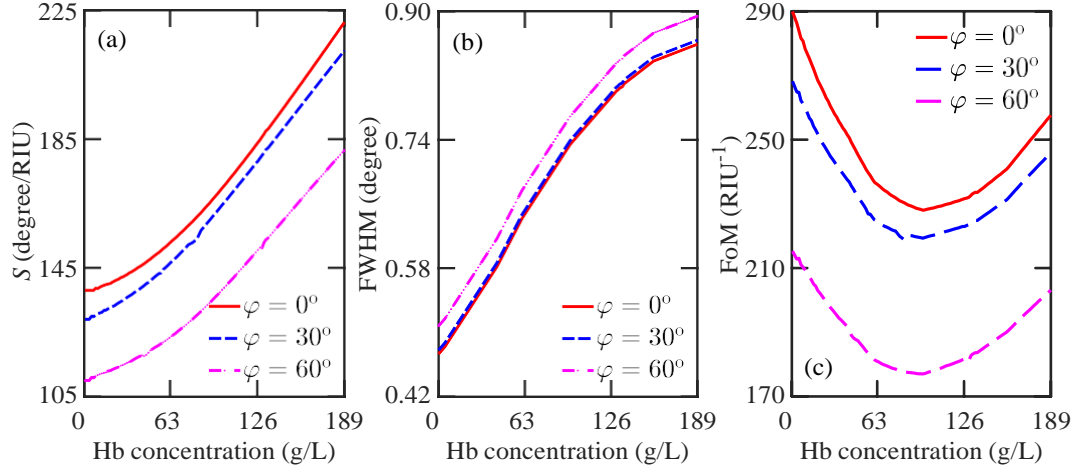


Figure 5.8: (a) S , (b) FWHM, and (c) FoM as a function of Hb concentration of the proposed GPCs based sensor using SPs resonance mode.

decrease more when $\varphi = 60^\circ$ compared to $\varphi = 30^\circ$. Therefore, the proposed GPCs based sensor shows polarization-dependent performances for FWHM and FoM.

Figure 5.8(a) shows the sensitivity of the proposed GPCs based sensor as a function of Hb concentration. Considering SPs resonance mode, sensitivity increment is very significant based on Hb concentration. As energy confinement of SPs is Ag-sensing layer interface, then SPs electromagnetic fields interact easily with the sensing element. Increasing Hb concentration from zero to 189 g/L, sensitivity increases 138 degree/RIU to 220 degree/RIU. When Hb concentration 189 g/L, sensitivity increment from TPs to SPs mode is 57.60%. However, increasing φ , sensitivity decreases and this reduction is more severe when $\varphi = 60^\circ$. We note that when Hb concentration is 189 g/L, increasing φ from 0° to 60° reduces sensitivity 220 degree/RIU to 181 degree/RIU i.e., 17.72% decreases of sensitivity. Thus, sensitivity of the proposed GPCs based sensor is polarization-dependent.

In Fig. 5.8(b), we show the FWHM of the proposed GPCs based sensor as a function of Hb concentration for different φ for SPs resonance mode. Increasing Hb concentration or φ , the FWHM increases. These values are comparatively larger than TPs mode and about 3 times higher than TPs mode. This is because the R -profile of

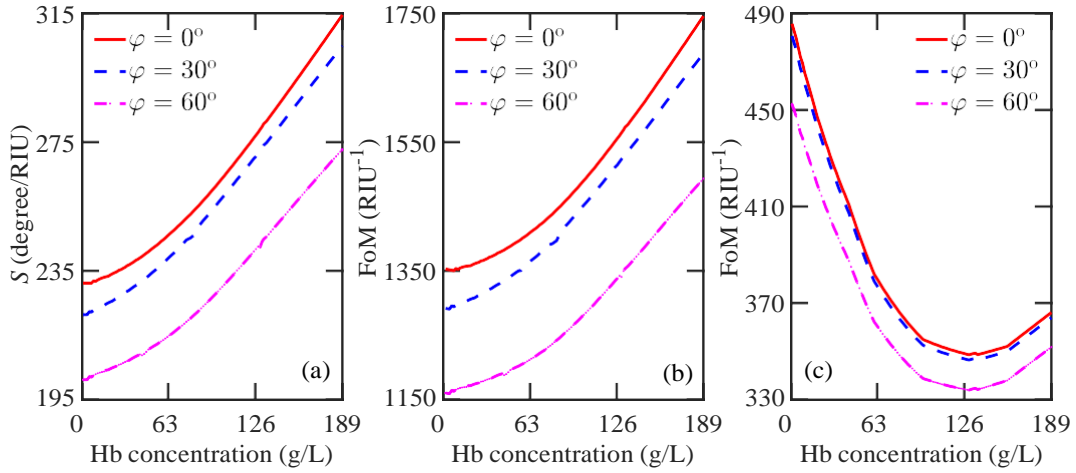


Figure 5.9: (a) S , (b) FWHM, and (c) FoM as a function of Hb concentration of the proposed GPCs based sensor of TPs and SPs hybrid resonance mode applying DDM.

SPs is more broadened than TPs when Hb concentration increases or φ increases. The main theme of wide FWHM of SPs mode is the losses of Ag which is essential for plasmonic wave creation [89]. In Fig. 5.8(c), we show the FoM of the proposed sensor for SPs resonance mode. Generally, FoM decreases when Hb concentration is from zero to 100 g/L. After that it starts to increase. This tendency is observed for all the value of φ . As usual the sensitivity analysis, FoM reduction rate is more severed when $\varphi = 60^\circ$.

However, when $\varphi = 0^\circ$ and Hb concentration is zero, then FoM is maximum and this value is 290 RIU^{-1} . If we use SPs instead of TPs, then FoM reduces 46.77% when $\varphi = 0^\circ$. The value of FoM gradually decreases when Hb concentration increase and 228 RIU^{-1} when Hb concentration is 100 g/L. As the increasing Hb concentration raises the n_{Hb} value, $\Delta\vartheta_r$ increases. However, the FWHM increases as Hb concentration increases then FoM decreases. Similar tendency is observed when $\varphi = 30^\circ$ or $\varphi = 60^\circ$. FoM is increasing after 100 g/L Hb concentration due to increment rate of sensitivity is gradually higher in this Hb concentration range. We note that SPs resonance mode shows polarization-dependent performances of the proposed GPCs based sensor.

In a hybrid TPs-SPs mode, we should give attention to the TPs mode as it drives the SPs mode away from the Ag layer, therefore decreases the losses of SPs. In addition, TPs resonance mode can be used for the unintended follow-up of the processes that occurs out-side of the Ag layer [89]. In TPs resonance mode, the FWHM is thinner due to low losses as the main part of surface wave is propagated in the interface of GPCs and Ag. Accordingly, a small part of the TPs enters into the Ag, the resonance becomes thinner and offers higher FoM. The fundamental drawback of TPs using biosensing areas is that this mode excites at the inner interface between AG-GPCs and hence, not directly accessible at the sensing element [89]. Consequently, using hybrid TPs-SPs mode for biosensing explores the TPs mode in a strong coupling region and applying one more mode provides the accuracy of sensing performances [261]. For hybrid TPs and SPs mode, we have an extra sensitivity modification option such as TPs resonance mode which is varying the robust coupling effect. As a result, we can control the width of R -profile by transferring the TPs mode energy to the SPs mode and hence, SPs provides the minimum R value and thinner width [89]. Next, we calculate the sensitivity and FoM using DDM as our proposed GPCs based sensor offers hybrid TPs-SPs mode. The sensitivity and FoM is calculated by [297]

$$S_{\text{DDM}} = \frac{\Delta\vartheta_{\text{SPs}}}{\Delta n_{\text{Hb}}} + \frac{\Delta\vartheta_{\text{TPs}}}{\Delta n_{\text{Hb}}} \quad (5.17)$$

where $\Delta\vartheta_{\text{SPs}}$ and $\Delta\vartheta_{\text{TPs}}$ are the change of resonance angle in SPs and TPs resonance mode, respectively. Moreover, we can determine the FoM by using the following expression [297]

$$\text{FoM} = S_{\text{DDM}}/\text{FWHM}_{\text{SPs/TPs}} \quad (5.18)$$

where $\text{FWHM}_{\text{SPs/TPs}}$ is FWHM for either SPs or TPs resonance mode. In DDM, usually FWHM_{SPs} is used for FoM calculation. As TPs resonance mode has little effect on sensing layer, we can also use this resonance for FoM calculation. In Fig. 5.9(a), we show the sensitivity of the proposed GPCs based sensor as a function of Hb concentration for different φ using the DDM. As usual, sensitivity increases when Hb concentration increases. On the other side, sensitivity decreases when

the value of φ increases. We note that when Hb concentration is 189 g/L then sensitivity is maximum i.e., 314.5 degree/RIU. Comparing the sensitivity of DDM with normal SPs resonance at this particular Hb concentration, sensitivity enhances by 30%. Besides, increasing φ the sensitivity decreases as usual and this decrement is more significant when $\varphi = 60^\circ$. Thus, sensitivity analysis using DDM also show polarization-dependent characteristics.

In Fig. 5.9(b), we show the FoM using TPs resonance mode. We find absolutely high FoM when $\varphi = 0^\circ$ and at 189 g/L Hb concentration level this value is 1740 RIU⁻¹. This value of FoM is quite impressive. As using TPs resonance provides thinner FWHM due to small loss of incident light at AG-GPCs interface. In addition, the FoM using TPs also show polarization-dependent behavior. In Fig. 5.9(c), we also show the FoM of the proposed sensor for SPs resonance mode. Generally, FoM decreases when Hb concentration increases from zero to 126 g/L, then it starts to increase. This tendency is observed for all the value of φ . As usual the sensitivity analysis, FoM reduction rate is more severed when $\varphi = 60^\circ$. Compared the result with SPs resonance mode, when $\varphi = 0^\circ$ and Hb concentration is zero, we find the FoM enhancement is around 40.02% using DDM. Using SPs mode in Figure 5.8(c), FoM is progressively decreased at Hb concentration is around 100 g/L. However, using DDM this position shifts to 126 g/L as DDM offers more sensitivity enhancement.

We note that the proposed GPCs based sensor performances especially the sensitivity and FoM are meaningfully better compared to that of the state-of-the-art optical sensors. We compare the sensitivity and FoM of the proposed GPCs based sensor in Table 1 with some recently reported sensors. We have compared the maximum sensitivity and FoM reachable from the proposed sensor as this stage Hb concentration is 189 g/L which corresponds $n_{\text{Hb}} = 1.36019$ with those reported in literature, as given in Table 5.1. We note that we have considered the sensors that use the DDM technique or not to determine the sensitivity and FoM. The compared sensors

Table 5.1: Performance comparison of our proposed sensor with different recently proposed sensors with or without using DDM.

Sensor configuration	S (degree/RIU)	FoM (RIU⁻¹)
Metal grating [298]	237	138
Graphene hybrid TPs [63]	—	161
2-D materials SPR [257]	235	71
PtSe ₂ SPR [259]	162	15
Graphene TPs-SPs [65]	—	12
Graphene SPR [74]	200	—
This work (TPs)	93	545
This work (SPs)	189	290
This work (DDM, SPs)	314.5	486
This work (DDM, TPs)	314.5	1746

also operate at 633 nm incident wavelength and report results for a sample of index ~ 1.36 .

5.5 Conclusion

The proposed anisotropic GPCs based hybrid SPs and TPs mode sensor can be used to sense the hemoglobin level in blood sample with very high sensitivity and figure-of-merit. We find that the sensor performances depend on the hybrid plasmonic mode which can control through the coupling effect of TPs and SPs with appropriate thickness of metal layer. Moreover, this coupling effect decreases the losses of noble metal in visible wavelength and hence, thinner the plasmonic mode such as TPs or SPs resonance. We apply anisotropic property on GPCs and observe the polarization-dependent sensor performance. We note that using double-dips method, maximum 314.5 degree/RIU sensitivity and 486 RIU⁻¹ are found when Hb concentration is 189 g/L. Besides, we can employ the TPs resonance mode as an secondary probe which can provide an extra information, such as helpful for the analysis of adsorption process at different interfaces of metal-GPCs. The performances of the

TPs and SPs hybrid mode of GPCs based sensor can be used for various types of proteins detection.

CHAPTER 6

GRAPHENE NANOSTRIP-BASED TM MODE DUAL-CHANNEL REFRACTIVE INDEX SENSOR

Generally, transverse magnetic (TM) polarization-based surface plasmons (SPs) are excited in plasmonic devices. While the transverse electric (TE) modes can be excited in graphene up to the visible frequency range, TM modes can be supported only from terahertz to the mid-infrared region. This work shows that graphene TM mode can be created in the visible spectrum by applying a suitable voltage across the graphene layer and using an appropriate interfacing dielectric layer thickness. Furthermore, utilizing this TM mode, this work proposes a dual-channel refractive index sensor, a promising alternative to the traditional Kretschmann arrangement. In the proposed sensor, two graphene layers, one with graphene nanostrip arrays, are exploited for efficient TM mode excitation. The nanostrips in the first graphene layer scatter the incoming radiation to the second graphene layer and generate TM mode at both layers even at the oblique incidence of light. The proposed dual-channel sensor shows a 2530 degree/RIU peak sensitivity when the sensing channels have the same analyte. Besides, two different analytes in the two channels having

different refractive indices can be detected simultaneously. The proposed graphene-based sensor will significantly impact biosensing and refractive index sensing without needing noble metal in the structure.

6.1 Introduction

Surface plasmons (SPs) propagate at a metal–dielectric interface, confining light in sub-wavelength dimensions [10]. During the past decade, SPs excited at a metal–dielectric interface have drawn significant interest for their applications in biosensing. However, metals are inherently lossy, and the propagation length of metal-based SPs is limited due to high losses. In addition, the direct excitation of metal-based SPs is impossible due to the wave-vector mismatch between the incident light and the SPs and the difficulty in altering the dielectric properties to overcome such a mismatch [98]. On the other hand, plasmons excited at a graphene–dielectric interface show controllable electromagnetic (EM) properties, comparatively low loss, and intense light absorption [92]. As a result, plasmons excited in graphene are promising alternatives for metal-based SPs in many areas of photonic and plasmonic devices, from mid-infrared (MIR) to terahertz (THz) wavelength region [299–302]. In addition, plasmons in graphene characteristics strongly depend on the substrate’s physical and geometrical parameters and can be tailored as per requirement [303].

Graphene shows an extraordinary property variation from dielectric to metallic response at energies near $\hbar\omega \approx 2E_f$, where E_f is the Fermi energy, \hbar is the reduced Plank’s constant, and ω is the angular wavelength [304]. In graphene, E_f can be efficiently controlled by doping [304, 305]. Graphene conductivity (σ_g), especially the imaginary part, changes sign from positive to negative when $\hbar\omega > 2E_f$, with the minimum at $\hbar\omega = 2E_f$ [191, 306]. The change of sign occurs since the electric field reverses the direction of the current [307]. The negative sign of σ_g (imaginary part) confirms the presence of the transverse electric (TE) mode in graphene

[306]. However, the TE mode's dispersion relation is very close to the light line, and it cannot confine the incident light sufficiently [307]. On the other hand, when $\sigma_g(\text{ima}) > 0$, that supports transverse magnetic (TM) mode in graphene [307]. Furthermore, graphene does not support TE and TM modes in the same wavelength region [98]. By applying a suitable gate voltage (V_g) to the graphene and using an appropriate interfacing dielectric layer thickness, the TM mode can be excited at a desired wavelength [169], allowing designing optoelectronic and plasmonic devices in optical frequency.

When $\hbar\omega < 1.667E_f$, graphene shows metallic response with a positive imaginary part of σ_g , supporting TM mode and ensuring strong light confinement and huge wave vectors [95]. However, graphene TM modes can reach up to the MIR range, whereas graphene TE mode up to the visible range [96]. Moreover, TM modes show collective electron oscillations, and therefore, the real part of ϵ_g must be negative to excite TM modes in graphene [308]. TM mode has been experimentally observed in graphene micro-ribbon arrays, infrared nano-imaging, nano-scopy and sub-wavelength gratings from THz to infrared (IR) wavelength range [97–99]. Besides, when photon energies (E_p) are $> 2E_f$, mono-layer graphene shows 2.3% light absorption, which limits the conversion from light to the electronic signals in a graphene layer [309].

Kretschmann-based angular interrogation method is generally used to create SPs, showing a high signal-to-noise ratio. However, the resonance angle shifting must be significant for enhanced sensor performance. The sensitivity of a Kretschmann configuration sensor is usually low, ~ 200 degree/RIU (refractive index unit) [100]. However, it is possible to increase the sensitivity by decreasing the refractive index of the prism material, although this approach reduces the detection accuracy [100]. To overcome the low sensitivity problem, several research groups have proposed various modified structures [229, 310, 311], e.g., metal nano-grooves-based plasmonic sensors to decrease the reflected light intensity [101]. Moreover, a silver (Ag)-gold (Au) grating SPR based sensor has shown maximum 346 degree/RIU sensitivity [312].

Nevertheless, these SPR sensors are not prism-based though prism-based sensors are extensively used in commercial SPR sensors [313]. Besides, graphene nanostrips with Au-aluminium (Al)-based SPR sensor has shown maximum 165 degree/RIU sensitivity and 164.28 RIU⁻¹ figure-of-merit (FoM), respectively[260]. Anyway, nanostrips geometry such as thickness and length effect on sensing performance are not analysed. Recently a SPR sensor based on Au grating where SPR and localized SPR (LSPR) coupling effect is proposed and found maximum 397.3 degree/RIU sensitivity though detection accuracy is not calculated[314].

On the other hand, TM mode in doped mono-layer graphene on a dielectric layer have been investigated through attenuated total reflectance (ATR) based technique in THz wavelength [315]. Likewise, graphene-based constructions using ATR have been proposed for polarizers and switches by adjusting the V_g [316, 317]. In addition, graphene can be sandwiched between different dielectric materials, such as SiO₂ and Si layers to control E_f and the electron density (n_g) [41, 91, 303]. By applying a suitable V_g , n_g can be increased. When $n_g \gtrsim 4 \times 10^{14} \text{ cm}^{-2}$, $E_f = 2.3 \text{ eV}$ [98, 318]. Furthermore, the properties of TM mode in graphene strongly depend on the relative permittivity (ϵ_r) and thickness (d) of SiO₂ [41]. However, it is observed that ϵ_r of SiO₂ is comparatively small. The only parameter to increase the E_f is the d of SiO₂. Alternatively, ZnO can be considered instead of SiO₂ due to its high ϵ_r [319].

This work shows that TM mode in graphene can be excited using the ATR method in the visible wavelength without needing the noble metal. We show that graphene optical properties can be effectively tuned by changing the thickness of the interfacing dielectric layer (d_{ZnO}) and V_g . Moreover, we use the Kubo analytical model to determine the optical properties of graphene layer. The proposed sensor uses dual channels for refractive index sensing, where graphene nanostrips set in the first graphene layer. These nanostrips scatter the incident light to a second graphene layer through different dielectric layers. To calculate the proposed dual-channel refractive index sensor performance, especially the sensitivity, we use transfer matrix

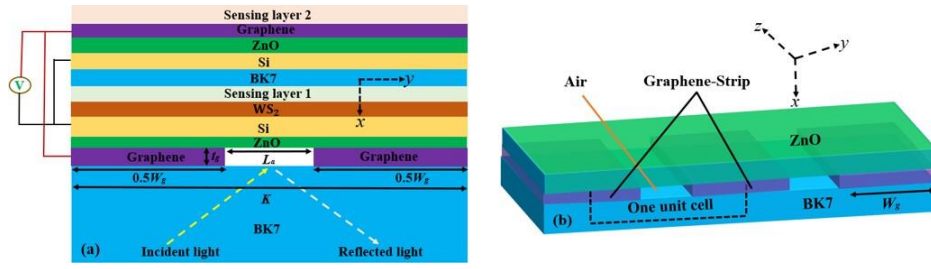


Figure 6.1: (a) 2-D schematic of the proposed graphene nanostraps based TM mode dual-channel refractive index sensor (one unit cell), and (b) 3-D schematic view of BK7, graphene-nanostraps, and ZnO of the proposed refractive index sensor.

method (TMM)-based angular interrogation. In addition, we use the logical multiplication for the calculation of total sensitivity. Our proposed dual-channel sensor shows maximum 2530 degree/RIU sensitivity when both the sensing channels have the same refractive index.

This chapter is organized such as: In Sec. 6.2, we present the proposed dual-channel sensor configuration. In Sec. 6.3, we define the optical properties of different materials. We describe the numeric techniques in Sec. 6.4 that solves the Maxwell expression by finite difference time domain (FDTD) procedure. We also present the dynamics of incident light in Sec. 6.5. Moreover, in Sec. 6.6, we show the results of the proposed dual-channel sensor. In Sec. 6.7, we summarize the findings of the proposed sensor.

6.2 Sensor Structure and Materials

Figure 6.1 shows the proposed dual-channel TM mode in graphene refractive index sensor. The proposed sensor structure is an effective substitute for the conventional Kretschmann configuration, allowing the sensor to excite the TM modes in graphene using oblique incidence of light. A semi-infinite BK7 prism is used as the glass

substrate. Light is incident to the prism–graphene interface from the prism side. Using a collinear optical arrangement for the incidence on plasmonic nanostructures will help to reduce the noise and miniaturize the sensor size [320]. The intensity of the reflected light is detected from the same side. The incident light has a 633 nm wavelength.

Graphene nanostrip arrays are placed on the prism material. Graphene nanostrips are separated by a distance $L_a = 100$ nm, as shown in Fig. 6.1, with air filling gaps between the strips. Using air pockets between graphene strips helps increase the resonance dip of the reflection profile [164]. The width (W_g) and thickness (t_g) of each graphene nanostrip are 500 nm and 50 nm, respectively. Graphene nanostrips have a periodicity (K) of $K = W_g + L_a = 600$ nm. For numerical analysis, we have considered only one unit cell of the structure with periodic boundary conditions.

In the visible wavelength, the graphene dielectric constant (ϵ_g) can be controlled using a suitable V_g [91]. The ZnO layer used in the proposed sensor between graphene and Si acts as an insulating layer, creating a parallel capacitor model [170]. Such an arrangement can change graphene optical properties [41]. We apply V_g between Si and graphene to control n_g , E_f , and electron mobility (μ_g) of the graphene [169, 170]. The thickness of ZnO and Si are 5 nm and 50 nm, respectively. As graphene's optical properties change with V_g , it behaves like a noble metal in the visible wavelength.

2-D materials like graphene, tungsten diselenide (WSe_2), molybdenum disulfide (MoS_2), and tungsten disulfide (WS_2) can alter the surface characteristics to enhance the adsorption of bio-molecules [321]. We use single-layer WS_2 on top of the Si layer for bio-molecule adsorption. The proposed sensor uses two sensing channels. The first one is located on the top of the WS_2 with a thickness $d_{S1} = 100$ nm [322]. The second sensing layer is on top of the second graphene layer. We also assume a thickness $d_{S2} = 100$ nm for the second sensing channel. However, a 30-nm-thin BK7 layer separates the first sensing channel from the Si layer to decrease the reflected

light intensity (R). The BK7 glass material is the substrate for the second sensing layer arrangement. The first graphene layer consists of nanostrips to help the excitation of TM modes in graphene. In addition, the periodic array of graphene nanostrips creates a scattering pattern, which illuminates the second graphene layer that acts like a metal [229] and produce TM modes at the graphene–sensing layer 2 interface.

6.3 Optical Properties

The performance of the proposed dual-channel refractive index sensor depends on the constituent materials' complex refractive indices. Therefore, the performance of the sensor also depends on the incident wavelength as materials show dispersive optical properties. The refractive index of BK7 prism is wavelength-dependent and can be determined by the method defined in Ref.[46]. The ϵ_g of two-dimensional (2-D) mono-layer graphene can be defined by [178]

$$\epsilon_g = 1 + i \frac{\sigma_g}{\omega \epsilon_0 t_m}, \quad (6.1)$$

where t_m is the thickness of mono-layer graphene and ϵ_0 is the free space permittivity. The permittivity of graphene (ϵ_g) has two components considering the orientation of the structure, such as tangential and normal. However, for the normal part, electric field cannot excite any current in the graphene sheet [283].

The optical properties of a few-layer graphene sheet are the same as the mono-layer graphene [178]. Generally, σ_g of a graphene sheet is calculated through the Kubo formula [95]

$$\sigma_g = i \frac{e^2 k_B T}{\pi \hbar^2 (\omega + i\tau^{-1})} \frac{E_f}{k_B T} + 2 \ln \frac{\exp \left(\frac{k_B T}{2 |E_f|} \right) + 1}{2 |E_f| + \hbar (\omega + i\tau^{-1})} + \frac{E_f}{4\pi \hbar} \ln \frac{\exp \left(\frac{k_B T}{2 |E_f|} \right) - 1}{2 |E_f| + \hbar (\omega + i\tau^{-1})}, \quad (6.2)$$

where K_B denotes the Boltzmann constant, T denotes the temperature, and e denotes the electron charge. The carrier relaxation time (τ) is related by [41]

$$\tau = \frac{\mu E_f^2}{e v_f} . \quad (6.3)$$

In this work, we use $v_f = 1.49 \times 10^6$ m/s[323] and determine the Fermi energy, $E_f = \sqrt{\hbar v_f (\pi n_g)}$ [180]. The graphene Fermi energy can be changed by applying V_g . The considered relation can be determine by a parallel capacitor model. The n_g of the graphene is determine by $n_g = \epsilon_r \epsilon_0 V_g / e d_{\text{ZnO}}$ [180]. Here, ϵ_r is the permittivity of ZnO. We use $\epsilon_r = 8.5$ for ZnO[324]. Graphene μ_g is defined by[181]

$$\mu_g(n_g, T) = \frac{\mu_0}{1 + (n_g/n^{\text{ref}})^A} \times \frac{1}{1 + (T/T^{\text{ref}} - 1)^B}, \quad (6.4)$$

where $\mu_0 = 225000 \text{ cm}^2 \text{V}^{-1} \text{s}^{-1}$, $n_{\text{ref}} = 1.1 \times 10^{13} \text{ cm}^{-2}$, $T = 300 \text{ K}$, $T_{\text{ref}} = 300 \text{ K}$, $A = 2.2$ and $B = 3$ [181, 325]. The refractive indices of ZnO, Si and WS_2 are collected from literature[48, 162, 326]. We use the sample refractive indices 1.33–1.45 for the sensing channels.

6.4 Simulation Method

To determine the R -profile of the proposed dual-channel refractive index sensor, we solve 2-D vectorial Maxwell's equations by the numerical FDTD method. We get the solutions for 2-D configurations as the proposed dual-channel structure is uniform in the z -direction. For 2-D simulation, we set $4000 \text{ nm} \times 600 \text{ nm}$ simulation area that includes the dual-channel sensing area. The perfectly matched layer boundary condition (BC) is set in the x -direction and the Bloch boundary condition in the y -direction.

We have used non-uniform meshing in the simulation area, ensuring a high mesh accuracy and maximum mesh refinement. In our FDTD simulations, the mesh

refinement approach is used to obtain sub-cell precision and ensure accuracy for the metal layer and metal–dielectric interface [327]. We have used 1 ns simulation time for the convergence of the FDTD calculations. We have used a TM-polarized light source with 633-nm wavelength. The incidence angle has been varied from 45° to 75° with step size 0.326° to determine the R -profile. The light source is placed in BK7 region at 1.90 μm from BK7-graphene interface. Also, we have recorded the R value and this monitor is placed in BK7 at 1.95 μm from the same interface.

6.5 Dynamics of Incident Light

The traditional Kretschmann configuration-based sensors obey the following expression[100]

$$\frac{2\pi}{\lambda} n_p \sin \vartheta_r = \text{Re}\{\beta\}, \quad (6.5)$$

where λ is the wavelength of the incident light, n_p is the refractive index of the glass prism, ϑ_r is the resonance angle, and β is the propagation constant of plasmons in graphene. In our dual-channel sensor configuration, the incident light is scattered from the first graphene nanostrip layer. The graphene nanostrip layer creates TM modes, creating extensive propagating vector moving in different directions [229]. The TM modes at the first graphene–sensing layer interface follow the expression [229]

$$\sin \vartheta_{r1} = \frac{z\lambda}{K \sqrt{\epsilon_p}}, \quad (6.6)$$

where ϵ_p is the permittivity of prism layer and z is the scattering order. From the graphene nanostrips, the dispersed radiation spreads to the second graphene layer through the dielectric layers. Hence, TM modes are also created at the second graphene–sensing layer interface, satisfying the following expression [229]

$$\sin \vartheta_{r2} = \frac{\sqrt{\epsilon_g \epsilon_{s2}}}{\epsilon_p (\epsilon_g + \epsilon_{s2})}, \quad (6.7)$$

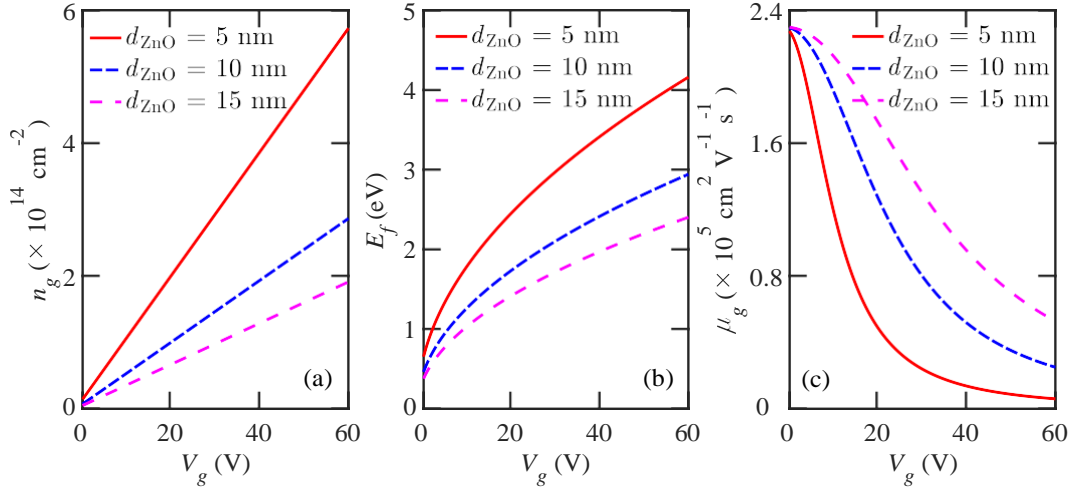


Figure 6.2: Optical properties of graphene as a function of V_g for three different thickness of ZnO (a) n_g , (b) E_f , and (c) μ_g .

where ϵ_{52} is the permittivity of the second sensing layer.

The transfer matrix approach is used for the calculation of R -profile for an N -layer system. The reflected light intensity is calculated by [113]

$$R = |r_p|^2, \quad (6.8)$$

where r_p is the coefficient of reflection of TM polarization.

6.6 Results and Discussion

Figure 6.2 shows the optical properties of graphene as a function of V_g for three thicknesses of ZnO. Figure 2(a) shows that n_g increases with V_g . Moreover, n_g also increases as d_{ZnO} decreases. A similar tendency is observed in Fig. 2(b), where E_f increases with V_g . However, E_f increases when d_{ZnO} decreases. Alternatively, μ_g decreases when V_g increases, as shown in Fig. 2(c), while μ_g increases as d_{ZnO} increases.

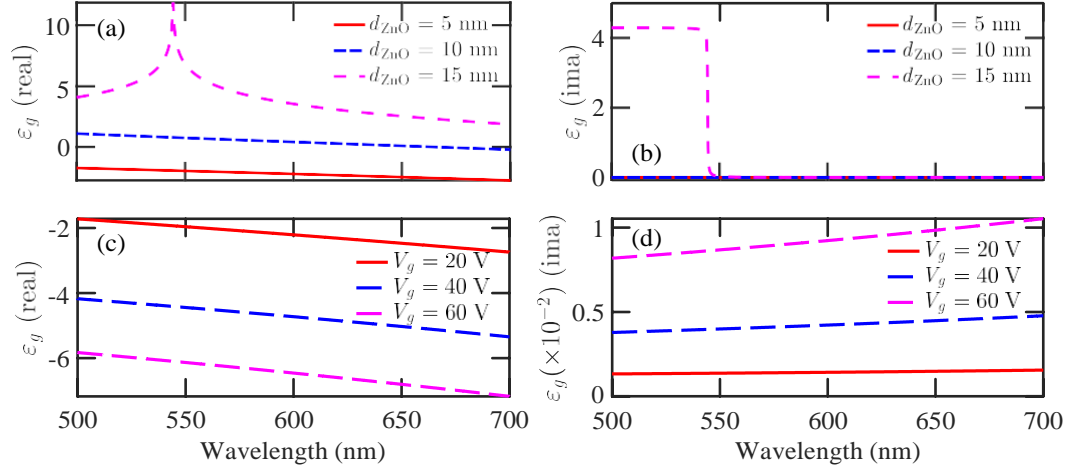


Figure 6.3: The ϵ_g of graphene as a function of wavelength. Three different thickness of ZnO where $V_g = 20$ V (a) Real, and (b) Imaginary and three different V_g where $d_{\text{ZnO}} = 5$ nm (c) Real, and (d) Imaginary.

Figure 6.3 shows ϵ_g against the light wavelength for different values of d_{ZnO} and V_g . First, we set $V_g = 20$ V and change d_{ZnO} . Figure 6.3(a) shows the real part of ϵ_g whereas Fig. 6.3(b) shows the imaginary part for different d_{ZnO} . The real part of ϵ_g decreases as the wavelength increases. Moreover, d_{ZnO} has significant impact on the real part of ϵ_g . When $d_{\text{ZnO}} = 5$ nm, the real part of ϵ_g is negative. The negative real part of ϵ_g confirms the existence of TM mode [306, 308]. Moreover, the ϵ_g (imaginary) of graphene is almost zero when d_{ZnO} is 5 nm and 10 nm. The real part of ϵ_g is positive and diverges logarithmically at 545 nm wavelength when $d_{\text{ZnO}} = 15$ nm. This is due to the step-like performance of the imaginary ϵ_g which indicates the inter-band absorption of radiation at $\hbar\omega > 2E_f$ [306].

Figures 6.3(c) and 6.3(d) show ϵ_g against wavelength for three different V_g , when $d_{\text{ZnO}} = 5$ nm. It is noted that the real part of ϵ_g becomes more negative as the wavelength increases, as shown in Fig. 6.3(c). The imaginary part of ϵ_g has a small value when $V_g = 20$ V, as shown in Figure 6.3(d). However, when $V_g = 60$ V, the imaginary part of ϵ_g is also small and quite satisfy. Therefore, it is clear that incident wavelength, V_g , and d_{ZnO} have significant influence on ϵ_g . When $d_{\text{ZnO}} = 5$ nm and $V_g = 60$ V, $E_f \gg E_p$ in the visible wavelength range, as shown in Fig. 6.2(b).

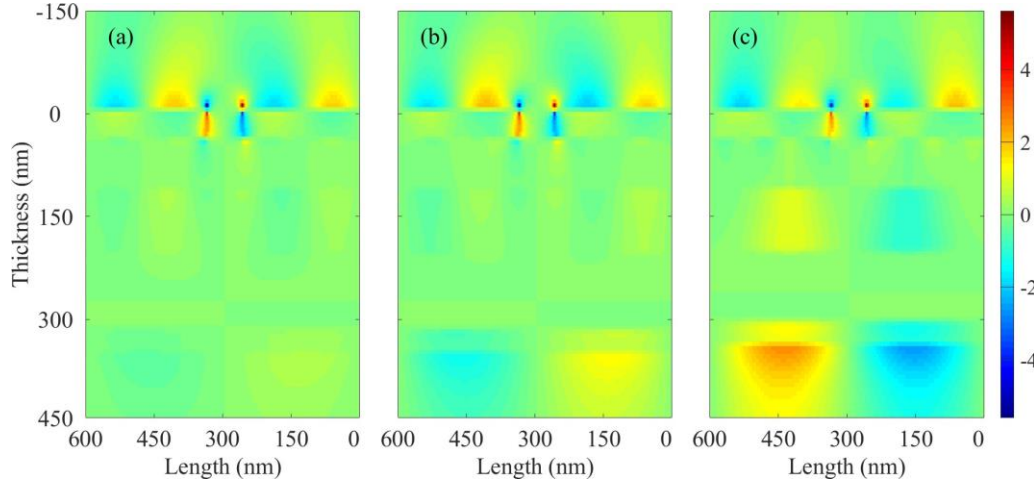


Figure 6.4: Observation of TM mode excitation when $d_{\text{ZnO}} = 5$ nm, $n_{s1} = n_{s2} = 1.33$, $L_a = 100$ nm, and $t_g = 50$ nm (a) $V_g = 20$ V, (b) $V_g = 40$ V, and (c) $V_g = 60$ V.

Therefore, σ_g is dominated by intra-band influence and can be estimated via the Drude model [328]. At 633 nm wavelength, the real part of ϵ_g is negative and the imaginary part has an insignificant value. Hence, graphene acts like a noble metal.

Figure 6.4 shows the excitation of TM modes in graphene for different V_g . In Fig. 6.4(a), we show that two TM modes are excited when $V_g = 20$ V. The first TM mode is excited at the BK7-graphene nanostrips-sensing layer 1 arrangement. The TM mode shows a symmetric behavior, i.e., one mode propagates at the graphene nanostrips–prism interface and the other propagates between the graphene nanostrips and the sensing layer 1 arrangement. As air-pockets are present in the graphene nanostrip layer, scattering patterns are observed. The scattered light reaches the second graphene layer and excites additional TM modes at the graphene–sensing layer 2 interface. In Figs. 6.4(b) and 6.4(c), we show the similar tendency when $V_g = 40$ V and $V_g = 60$ V, respectively. However, as ϵ_g (real) negative value reduces with a increasing V_g , the TM mode excitation in the second graphene layer increases as well with a increasing V_g . We have used $V_g = 60$ V in results presented in the following analysis.

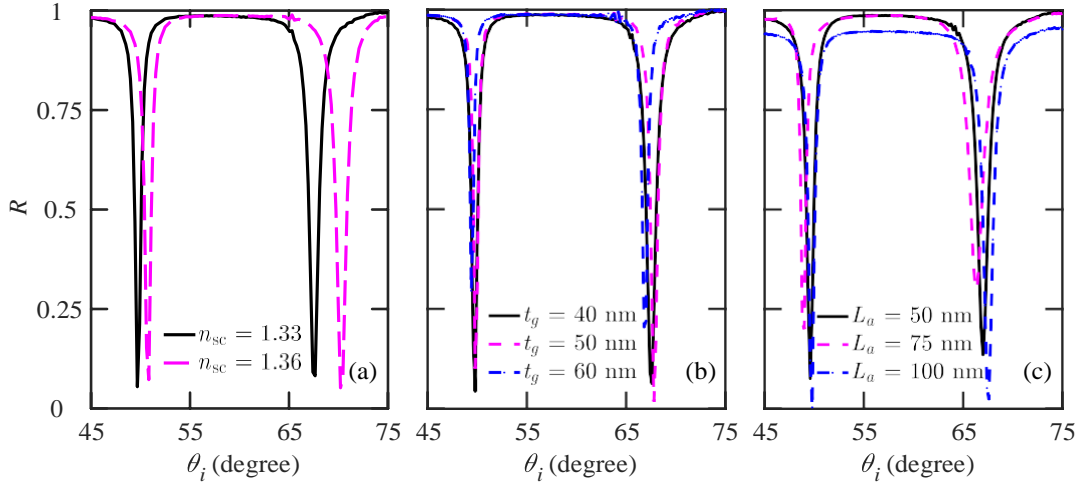


Figure 6.5: R -profile of the proposed dual-channel refractive index sensor (a) Similar n_s for both the sensing channel when $L_a = 100$ nm and $t_g = 50$ nm, (b) Variation of t_g when $L_a = 100$ nm, and $n_{s1} = n_{s2} = 1.33$, and (c) Variation of L_a when $n_{s1} = n_{s2} = 1.33$, and $t_g = 50$ nm.

Figure 6.5(a) shows the R -profile as a function of the incident angle (ϑ_i). As the proposed sensor has dual channels, we can take different or similar sensing materials for each channel. We use $n_{s1} = n_{s2} = 1.33$ and $n_{s1} = n_{s2} = 1.36$ for the first and second sensing channel. In each case, we observe two resonance dips. When $n_{s1} = n_{s2} = 1.33$, we observe dips at 49.80° and 67.60° . We consider these two resonance dips as reference resonance angles, ϑ_{r1} and ϑ_{r2} , for the first and the second sensing channels. On the other hand, when $n_{s1} = n_{s2} = 1.36$, the first resonance dip is shifted to 50.83° and the second resonance dip is found at 70.20° , respectively. When $n_{s1} = n_{s2} = 1.36$, we detect that the resonance angles shift and the R -profiles widen. At the same time, the R_{\min} decreases a little. We note that increasing n_{s1} or n_{s2} , confinement of incident light increases. As a result, R_{\min} decreases. Moreover, increasing n_{s1} or n_{s2} the excited GP_{s1} and GP_{s2} are decayed faster [91]. Hence, the R -profile is widened.

In Fig. 6.5(b), we show the R -profile for different thickness of each graphene nanorip. Increasing t_g , the R value is decreased. However, when $t_g = 50$ nm, then R value is minimum. When $t_g > 50$ nm, R value is increased which indicates the

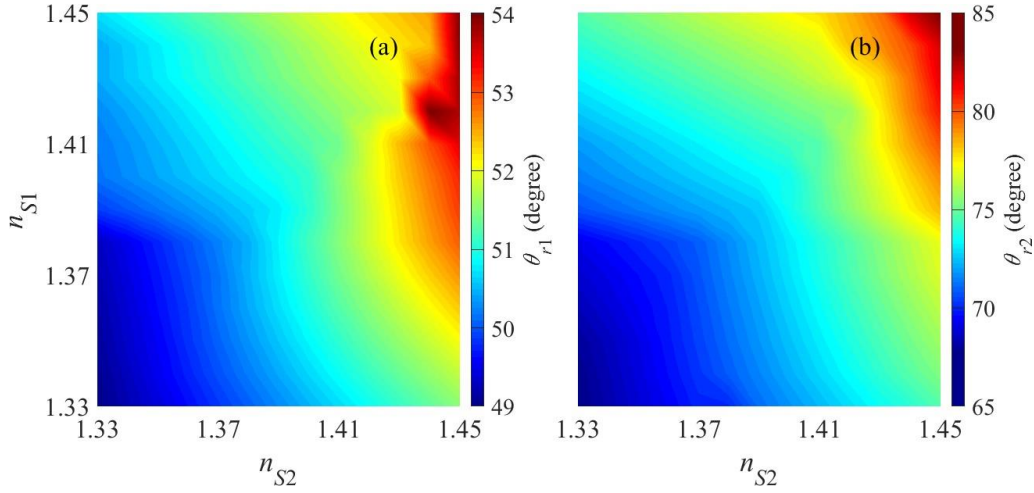


Figure 6.6: The resonance angle shifting of the proposed structure as a function of dual-channel sensing layer refractive index (a) ϑ_{r1} , and (b) ϑ_{r2} .

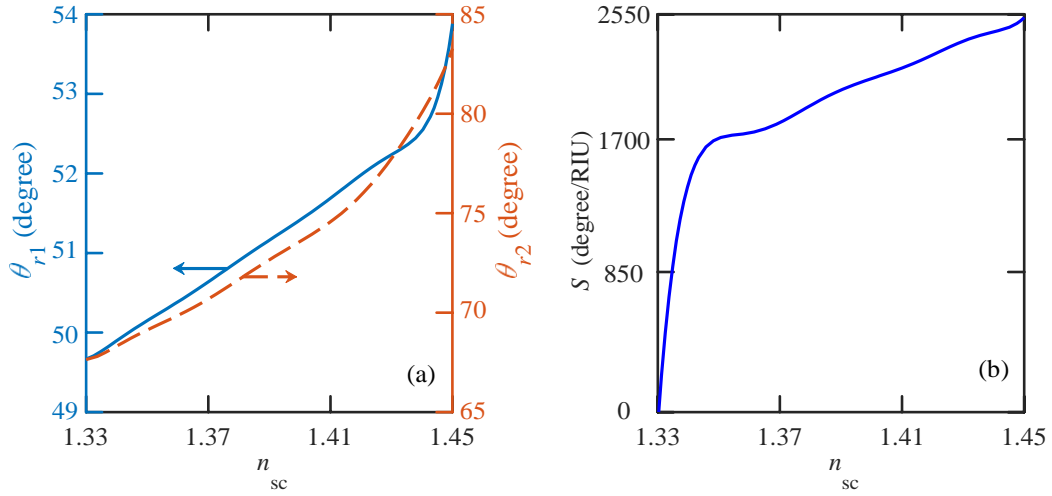


Figure 6.7: Resonance angle shifting and sensitivity analysis when both sensing channels have the same refractive index (a) Resonance angle shifting, and (b) Sensitivity.

absorption of incident light decreases. Similar tendency is observed in Ref. [91]. In Fig. 6.5(c), we show the R -profile for three different value of L_a . We find that when $L_a = 100$ nm both GP_{S1} and GP_{S2} are minimum which confirms the maximum absorption of incident light. Thus, in our proposed sensor we set $L_a = 100$ nm.

Figures 6.6(a) and 6.6(b) show the shift of ϑ_{r1} and ϑ_{r2} for cases when n_{S1} and n_{S2} are the same or different. The shift in ϑ_{r1} and ϑ_{r2} increases as n_{S1} or n_{S2} increases.

However, ϑ_{r1} shifts smaller than ϑ_{r2} . When $n_{s1} = n_{s2} = 1.45$, maximum value of $\vartheta_{r1} = 53.88^\circ$ and $\vartheta_{r2} = 83.27^\circ$ are observed. The angle shifting property is high when $n_{s1} = 1.35$ to 1.45 and $n_{s2} = 1.42$ to 1.45 for ϑ_{r1} . Similar tendency is observed, when $n_{s1} = 1.37$ to 1.45 and $n_{s2} = 1.41$ to 1.45 for ϑ_{r2} . We note that the second sensing layer produces greater angle shifting and narrower spectral region than the first sensing layer. On the other hand, the proposed dual-channel refractive index sensor can sense the two different sensing elements independently. For example, when $n_{s1} = 1.36$ and $n_{s2} = 1.40$, we get $\vartheta_{r1} = 50.36^\circ$ and $\vartheta_{r2} = 69.86^\circ$, as shown in Figs. 6.6(a) and 6.6(b), respectively.

Figure 6.7(a) shows the resonance angle shifting when both the channels have the same refractive index. When $n_{s1} = n_{s2} = 1.33$, we can consider it $n_{sc} = 1.33$ and find $\vartheta_{r1} = 49.80^\circ$ and $\vartheta_{r2} = 67.60^\circ$, respectively. Next, when $n_{s1} = n_{s2} = 1.34$, we get $\vartheta_{r1} = 49.99^\circ$ and $\vartheta_{r2} = 67.91^\circ$, separately. We calculate the sensitivity of each individual channel by $S_1 = \Delta\vartheta_{r1}/\Delta n_{s1}$ degree/RIU and $S_2 = \Delta\vartheta_{r2}/\Delta n_{s2}$ degree/RIU, respectively. In Figure 6.7(b), we show the combined sensitivity when both the sensing channels have same refractive index. If $n_{s1} = n_{s2}$, then we can write $S_1 = 1$ and $S_2 = 1$. To calculate the total sensitivity, we can follow the logical multiplication [329]

$$S = S_1 S_2 \quad (6.9)$$

where S is the total sensitivity. Therefore, when $n_{s1} = n_{s2} = 1.34$, S is 1645 degree/RIU. Increasing n_{s1} and n_{s2} and maintain this $n_{s1} = n_{s2}$, the tendency of S is upward. When $n_{s1} = n_{s2} = 1.45$, S is maximum and we get 2530 degree/RIU.

Figure 6.8 shows the sensitivity of the proposed sensor when n_{s1} and n_{s2} vary. Figure 6.8(a) shows the sensitivity of the first sensing channel and Fig. 6.8(b) shows that of the second. To calculate the sensitivity, we use expressions $S_1 = (\vartheta_{r1} - 49.80)/(n_{s1} - 1.33)$ and $S_2 = (\vartheta_{r2} - 67.60)/(n_{s2} - 1.33)$ for first and second sensing channel, respectively. We note when $n_{s1} = 1.340$ – 1.355 and $n_{s2} = 1.40$ – 1.45 , the sensitivity is maximum for both the sensing channel. We find $S_1 = 236$ degree/RIU

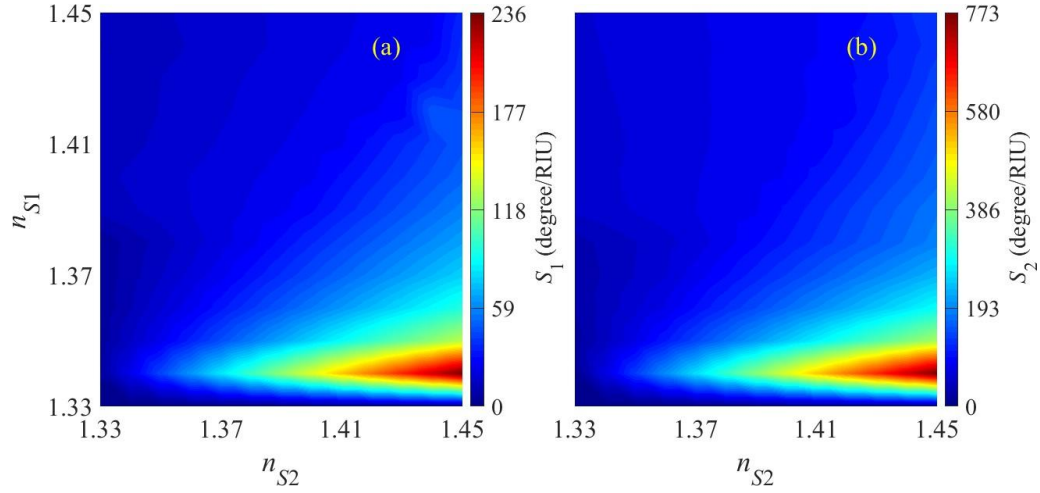


Figure 6.8: Sensitivity analysis of the proposed dual-channel sensor as a function of dissimilar sensing layer refractive index (a) S_1 , and (b) S_2 .

and $S_2 = 773$ degree/RIU in a specific narrow region. If we want to detect specific bio-molecules or pathogens which refractive index is in this specific region, we can detect these molecules with high sensitivity. Such specific sensitivity in a narrow refractive index region is also observed in Ref. [330]. Moreover, the second sensing channel shows almost 3.25 times higher sensitivity than the first sensing channel. However, when $n_{S1} = 1.355\text{--}1.410$ and $n_{S2} = 1.38\text{--}1.45$, S_2 is impressive compared to the existing literature [46, 331–334].

6.7 Conclusion

We show that the unusual TM modes in graphene at visible wavelength can be excited in the modified Kretschmann configuration without the need of noble metal. Our proposed graphene nanostrips based plasmonic sensor produces TM modes between graphene nanostrips and first sensing layer. Whereas these nanostrips then scatter the incoming incidence light with a large propagating vector and produces another TM modes in the graphene-second sensing layer interface. The creation of TM modes depend on several factors such as gate-voltage, incident wavelength, and

thickness of ZnO. The proposed dual-channel refractive index sensor is highly sensitive when both channels have the same refractive index. Moreover, our proposed sensor can detect the refractive index separately using the two different resonance dips. The structural and material properties are conceivable and can be fabricable.

CHAPTER 7

CONCLUSIONS

The absorption of incident light is a significant property of SPs, enabling sub-wavelength control of light [13]. On the other hand, electron oscillations in metal are damped when SPs are excited [14]. As a result, the R -profile is practically spreading due to increase the absorption of incident light. We observe that this problem is more significant in the visible wavelength range. Typically, Ag is used in SPR biosensors due to its low cost. Ag is vulnerable to oxidation, and the SPR sensor performances hamper due to the wider R -profile caused by the oxide layer [33]. Diverse options are available to decrease the Ag oxidation in SPR biosensors [34]. Unfortunately, these options are not ideally suitable for reducing the Ag oxidation.

To avoid the problem of oxidation, the potential material will be graphene which has many exclusive properties [35]. The absorption of the incident light of monolayer graphene is 2.3% in the visible wavelength, a significant amount for a 0.34 nm layer thickness. However, more strong light-matter interaction is required for optical sensing [49]. We observe that using multi-layer graphene in SPR biosensors can increase light absorption though graphene produces extra damping in SPs because of its large imaginary refractive index. Hence, multi-layer graphene widens the R -profile and decreases the detection accuracy [52]. To increase the light-matter interaction, GPCs-based sensor can be used as SPs will be excited in GPCs with

high photon absorption [49]. But, the GPCs-based sensor shows the scatter SP modes which decreases the sensor performances.

Instead of using R -profile for sensor performances, we have searched for alternate parameters to enhance the sensor performance. We have observed poor magnetic response of different dielectric materials, mainly in visible wavelength [16]. Though the magnetic response has been proposed in metal-insulator-metal configurations using Fano resonances, this structure is not suitable for biosensing because destructive interference is created due to anti-phase dipole oscillations [19]. On the other hand, SPR-based Kretschmann biosensors present poor magnetic response, and their magnetic properties have never been applied for biosensing.

On the other side, GPs have shown adjustable electromagnetic properties and strongly depend on substrate physical and geometrical parameters. From THz to the MIR frequency region, graphene shows a metallic response that offers high light confinement and very large wave vectors [95]. However, GPs mode can reach from THz to MIR range whereas TE up to visible range [96].

The primary purpose of this thesis is to enhance the SPR biosensor performances, which must have low losses and high resonance angle shifting to increase the sensitivity and FoM. Also, we have developed a method for determining sensor performances using magnetic resonance through planar multi-layer optical biosensors for the first time. We have also proposed the enhancement of light absorption of graphene monolayer by using controlled V_g . On that side, we have proposed a graphene-based SPR sensor to detect critical pathogens such as SARS-CoV-2, S-protein, and Hb-protein. Besides, we have shown theoretically that the excitement of TM mode in graphene without needing noble metals in the visible wavelength can significantly enhance sensor performances.

We now summarize the major findings of this dissertation:

- We have proposed the Kretschmann-based configuration, which created a strong magnetic resonance at a specific sensing layer refractive index. The magnetic response of this structure at a particular index range was high, which showed potential in sensing applications. We described the theoretical models we used to calculate μ_{eff} and R using the S-parameters retrieval method. Moreover, we discussed the Kretschmann-based SPR sensor's possible experimental set-up and the FDTD simulation approach. We showed that the magnetic response in visible wavelength could lead to a new method for detecting diverse critical bio-molecules. We have compared the results with the conventional technique in state-of-the-art sensors, which frequently use more complex structures.
- We have proposed a graphene SPR glucose sensor where monolayer graphene optical properties were controlled by a suitable V_g . We modified the monolayer graphene Fermi energy using V_g to increase the absorption of incident light and hence, improved the sensitivity and FoM of the proposed sensor. To determine the sensor performances, We used a TMM-based angular interrogation method. We calculated the monolayer graphene conductivity using the Kubo formula at different applied V_g at visible wavelength. The proposed glucose sensor detected the BSL with high accuracy. In addition, the proposed sensor sensed the BSL without using any labels, tags, or chemical enzymes. On the other hand, we discussed the proposed sensor and sensing element affected by temperature where variation by $\pm 10^\circ\text{C}$ around room temperature changed the detection accuracy by only $< 5\%$.
- We have extended our work by using a multi-layer graphene SPR sensor to detect SARS-CoV-2, S-protein with fM concentration range without needing any labeling or complex sample preparation. We used multi-layers graphene in the proposed sensor where ACE2 antibodies immobilized on the graphene surface that helped for efficient adsorption of the SARS-CoV-2, S-protein. We used thin layers of novel 2-D materials, such as WS_2 , KNbO_3 , and BP or BlueP, between graphene and Ag layers to increase the light absorption and

hence, the sensor performances. We showed that the proposed sensor detected the S-protein by using the property of resonance angle shifting. The proposed sensor detected as small as 1 fM S-protein concentration, which is appropriate for the initial detection of COVID-19 patients. Moreover, we have compared the proposed sensor LoD with the existing literature and found it much smaller. We applied the FDTD method to describe the sensor response to incident light. In addition, we used the Langmuir model to determine the binding kinetics between ACE2 and S-protein. Though the analysis of the proposed sensor was theoretical, we think an experimental clarification of these findings was vital, which was out of the scope of this work. We think such promising results of the proposed sensor confirmed its suitability for SARS-CoV-2 and S-protein detection and may find applications in detecting other biochemical and biological analytes.

- We have designed a GPCs-based TPs and SPs hybrid mode for Hb detection in the visible wavelength region. We have optimized the Ag thickness and the number of the unit cell of GPC based on R minimum and FWHM. The energy transfers from TPs mode to SPs mode were determined by FMSA. We also showed the anti-crossing effect between TPs mode and SPs mode for different polarization angles using the TMM. We used Barer's analytical model to calculate the optical properties of Hb in the blood. The sensor performances, especially the change of resonance angle and FWHM for both the TPs mode and SPs mode, were calculated using TMM-based angular interrogation method. We applied the DDM to determine the sensitivity and FoM. The proposed sensor has shown energy exchanges from TPs mode to SPs mode, which ultimately improved the sensitivity for Hb detection. Besides, we showed the effect of TPs resonance on sensing and found that TPs significantly impact sensing, particularly the high FoM.
- Finally, we have modified the conventional Kretschmann-based configuration where TM mode in graphene was excited in the visible wavelength without

needing the noble metal. We showed that graphene optical properties could be effectively tuned by changing the thickness of the insulating dielectric layer (d_{ZnO}) and V_g . We used the Kubo analytical model to determine the optical properties of the graphene layer. The proposed sensor used dual channels for refractive index sensing, where graphene nanostrips are set in the first graphene layer. These nanostrips scattered the incident light to a second graphene layer through different dielectric layers. To calculate the proposed dual-channel refractive index sensor performances, especially the sensitivity, we used the TMM-based angular interrogation technique. We used logical multiplication for the calculation of total sensitivity. The proposed dual-channel refractive index sensor was highly sensitive when both channels had the same refractive index. Using two different resonance dips, our proposed sensor sensed the refractive index separately. We think the proposed sensor's structural and material properties were conceivable and could be manufacturable.

Bibliography

- [1] D. R. Thévenot, K. Toth, R. A. Durst, and G. S. Wilson, “Electrochemical biosensors: recommended definitions and classification,” *Biosensors and Bioelectronics*, vol. 16, no. 1-2, pp. 121–131, 2001.
- [2] C. Karunakaran, R. Rajkumar, and K. Bhargava, “Introduction to biosensors,” in *Biosensors and Bioelectronics*, pp. 1–68, Elsevier Ltd., 2015.
- [3] J. H. Luong, K. B. Male, and J. D. Glennon, “Biosensor technology: technology push versus market pull,” *Biotechnology Advances*, vol. 26, no. 5, pp. 492–500, 2008.
- [4] P. Damborský, J. Švitel, and J. Katrlík, “Optical biosensors,” *Essays in Biochemistry*, vol. 60, no. 1, pp. 91–100, 2016.
- [5] N. Yildirim, F. Long, C. Gao, M. He, H.-C. Shi, and A. Z. Gu, “Aptamer-based optical biosensor for rapid and sensitive detection of 17 β -estradiol in water samples,” *Environmental Science & Technology*, vol. 46, no. 6, pp. 3288–3294, 2012.
- [6] P. Kozma, F. Kehl, E. Ehrentreich-Förster, C. Stamm, and F. F. Bier, “Integrated planar optical waveguide interferometer biosensors: A comparative review,” *Biosensors and Bioelectronics*, vol. 58, pp. 287–307, 2014.
- [7] J. Xu, D. Suarez, and D. S. Gottfried, “Detection of avian influenza virus using an interferometric biosensor,” *Analytical and Bioanalytical Chemistry*, vol. 389, no. 4, pp. 1193–1199, 2007.

-
- [8] U. Dinish, C. Y. Fu, K. S. Soh, B. Ramaswamy, A. Kumar, and M. Olivo, “Highly sensitive sers detection of cancer proteins in low sample volume using hollow core photonic crystal fiber,” *Biosensors and Bioelectronics*, vol. 33, no. 1, pp. 293–298, 2012.
- [9] H. Sarker, M. Faisal, and M. A. Mollah, “Slotted photonic crystal fiber-based plasmonic biosensor,” *Applied Optics*, vol. 60, no. 2, pp. 358–366, 2021.
- [10] W. L. Barnes, A. Dereux, and T. W. Ebbesen, “Surface plasmon subwavelength optics,” *Nature*, vol. 424, no. 6950, pp. 824–830, 2003.
- [11] C. Nylander, B. Liedberg, and T. Lind, “Gas detection by means of surface plasmon resonance,” *Sensors and Actuators*, vol. 3, pp. 79–88, 1982.
- [12] E. Kretschmann and H. Raether, “Radiative decay of non radiative surface plasmons excited by light,” *Zeitschrift für Naturforschung A*, vol. 23, no. 12, pp. 2135–2136, 1968.
- [13] D. K. Gramotnev and S. I. Bozhevolnyi, “Plasmonics beyond the diffraction limit,” *Nature Photonics*, vol. 4, no. 2, pp. 83–91, 2010.
- [14] V. N. Konopsky and E. V. Alieva, “Long-range propagation of plasmon polaritons in a thin metal film on a one-dimensional photonic crystal surface,” *Physical Review Letters*, vol. 97, no. 25, p. 253904, 2006.
- [15] A. Degiron and D. R. Smith, “Numerical simulations of long-range plasmons,” *Optics Express*, vol. 14, no. 4, pp. 1611–1625, 2006.
- [16] L. D. Landau, J. Bell, M. Kearsley, L. Pitaevskii, E. Lifshitz, and J. Sykes, *Electrodynamics of Continuous Media*, vol. 8. Elsevier Ltd., 2013.
- [17] A. Poddubny, I. Iorsh, P. Belov, and Y. Kivshar, “Hyperbolic metamaterials,” *Nature Photonics*, vol. 7, no. 12, pp. 948–957, 2013.

- [18] V. P. Drachev, V. A. Podolskiy, and A. V. Kildishev, “Hyperbolic metamaterials: new physics behind a classical problem,” *Optics Express*, vol. 21, no. 12, pp. 15048–15064, 2013.
- [19] G. T. Papadakis, D. Fleischman, A. Davoyan, P. Yeh, and H. A. Atwater, “Optical magnetism in planar metamaterial heterostructures,” *Nature Communications*, vol. 9, no. 1, pp. 1–9, 2018.
- [20] J. Chen, W. Fan, T. Zhang, C. Tang, X. Chen, J. Wu, D. Li, and Y. Yu, “Engineering the magnetic plasmon resonances of metamaterials for high-quality sensing,” *Optics Express*, vol. 25, no. 4, pp. 3675–3681, 2017.
- [21] H. Vahed and C. Nadri, “Sensitivity enhancement of spr optical biosensor based on graphene–mos2 structure with nanocomposite layer,” *Optical Materials*, vol. 88, pp. 161–166, 2019.
- [22] Q.-Q. Meng, X. Zhao, C.-Y. Lin, S.-J. Chen, Y.-C. Ding, and Z.-Y. Chen, “Figure of merit enhancement of a surface plasmon resonance sensor using a low-refractive-index porous silica film,” *Sensors*, vol. 17, no. 8, p. 1846, 2017.
- [23] A. Shalabney and I. Abdulhalim, “Figure-of-merit enhancement of surface plasmon resonance sensors in the spectral interrogation,” *Optics Letters*, vol. 37, no. 7, pp. 1175–1177, 2012.
- [24] Z. Li, K. Aydin, and E. Ozbay, “Determination of the effective constitutive parameters of bianisotropic metamaterials from reflection and transmission coefficients,” *Physical Review E*, vol. 79, no. 2, p. 026610, 2009.
- [25] R. Marqués, F. Medina, and R. Rafii-El-Idrissi, “Role of bianisotropy in negative permeability and left-handed metamaterials,” *Physical Review B*, vol. 65, no. 14, p. 144440, 2002.
- [26] H. Ouyang, C. C. Striemer, and P. M. Fauchet, “Quantitative analysis of the sensitivity of porous silicon optical biosensors,” *Applied Physics Letters*, vol. 88, no. 16, p. 163108, 2006.

- [27] T. L. Kelly, A. Garcia Sega, and M. J. Sailor, "Identification and quantification of organic vapors by time-resolved diffusion in stacked mesoporous photonic crystals," *Nano Letters*, vol. 11, no. 8, pp. 3169–3173, 2011.
- [28] X. Chen, B.-I. Wu, J. A. Kong, and T. M. Grzegorzczak, "Retrieval of the effective constitutive parameters of bianisotropic metamaterials," *Physical Review E*, vol. 71, no. 4, p. 046610, 2005.
- [29] Z. Li, K. Aydin, and E. Ozbay, "Retrieval of effective parameters for bianisotropic metamaterials with omega shaped metallic inclusions," *Photonics and Nanostructures-Fundamentals and Applications*, vol. 10, no. 3, pp. 329–336, 2012.
- [30] A. V. Kildishev, J. D. Borneman, X. Ni, V. M. Shalaev, and V. P. Drachev, "Bianisotropic effective parameters of optical metamagnetics and negative-index materials," *Proceedings of the IEEE*, vol. 99, no. 10, pp. 1691–1700, 2011.
- [31] D. Smith, S. Schultz, P. Markoš, and C. Soukoulis, "Determination of effective permittivity and permeability of metamaterials from reflection and transmission coefficients," *Physical Review B*, vol. 65, no. 19, p. 195104, 2002.
- [32] B. H. Ong, X. Yuan, S. C. Tjin, J. Zhang, and H. M. Ng, "Optimised film thickness for maximum evanescent field enhancement of a bimetallic film surface plasmon resonance biosensor," *Sensors and Actuators B: Chemical*, vol. 114, no. 2, pp. 1028–1034, 2006.
- [33] S. H. Choi and K. M. Byun, "Investigation on an application of silver substrates for sensitive surface plasmon resonance imaging detection," *JOSA A*, vol. 27, no. 10, pp. 2229–2236, 2010.

- [34] S. Szunerits, N. Maalouli, E. Wijaya, J.-P. Vilcot, and R. Boukherroub, “Recent advances in the development of graphene-based surface plasmon resonance (spr) interfaces,” *Analytical and Bioanalytical Chemistry*, vol. 405, no. 5, pp. 1435–1443, 2013.
- [35] F. Schedin, A. K. Geim, S. V. Morozov, E. W. Hill, P. Blake, M. I. Katsnelson, and K. S. Novoselov, “Detection of individual gas molecules adsorbed on graphene,” *Nature Materials*, vol. 6, no. 9, pp. 652–655, 2007.
- [36] Z. Li, E. A. Henriksen, Z. Jiang, Z. Hao, M. C. Martin, P. Kim, H. L. Stormer, and D. N. Basov, “Dirac charge dynamics in graphene by infrared spectroscopy,” *Nature Physics*, vol. 4, no. 7, pp. 532–535, 2008.
- [37] V. Gusynin, S. Sharapov, and J. Carbotte, “Unusual microwave response of dirac quasiparticles in graphene,” *Physical Review Letters*, vol. 96, no. 25, p. 256802, 2006.
- [38] B. Wunsch, T. Stauber, F. Sols, and F. Guinea, “Dynamical polarization of graphene at finite doping,” *New Journal of Physics*, vol. 8, no. 12, p. 318, 2006.
- [39] T. Stauber, N. Peres, and A. Geim, “Optical conductivity of graphene in the visible region of the spectrum,” *Physical Review B*, vol. 78, no. 8, p. 085432, 2008.
- [40] M. Bruna and S. Borini, “Optical constants of graphene layers in the visible range,” *Applied Physics Letters*, vol. 94, no. 3, p. 031901, 2009.
- [41] H. Lu, C. Zeng, Q. Zhang, X. Liu, M. M. Hossain, P. Reineck, and M. Gu, “Graphene-based active slow surface plasmon polaritons,” *Scientific Reports*, vol. 5, no. 1, pp. 1–7, 2015.
- [42] J. Dyro, *Clinical Engineering Handbook*. Elsevier Ltd., 2004.
- [43] F. D. A. USA, *Blood Glucose Meter Accuracy 2014*, accessed June 10, 2020.

- [44] W. Lam, L. Chu, C. Wong, and Y. Zhang, "A surface plasmon resonance system for the measurement of glucose in aqueous solution," *Sensors and Actuators B: Chemical*, vol. 105, no. 2, pp. 138–143, 2005.
- [45] P. S. Menon, B. Mulyanti, N. A. Jamil, C. Wulandari, H. S. Nugroho, G. S. Mei, N. F. Z. Abidin, L. Hasanah, R. E. Pawinanto, and D. D. Berhanuddin, "Refractive index and sensing of glucose molarities determined using au-cr k-spr at 670/785 nm wavelength," *Sains Malaysiana*, vol. 48, no. 6, pp. 1259–1265, 2019.
- [46] P. Sun, M. Wang, L. Liu, L. Jiao, W. Du, F. Xia, M. Liu, W. Kong, L. Dong, and M. Yun, "Sensitivity enhancement of surface plasmon resonance biosensor based on graphene and barium titanate layers," *Applied Surface Science*, vol. 475, pp. 342–347, 2019.
- [47] H. Jiang, S. Choudhury, Z. A. Kudyshev, D. Wang, L. J. Prokopeva, P. Xiao, Y. Jiang, and A. V. Kildishev, "Enhancing sensitivity to ambient refractive index with tunable few-layer graphene/hbn nanoribbons," *Photonics Research*, vol. 7, no. 7, pp. 815–822, 2019.
- [48] A. S. Kushwaha, A. Kumar, R. Kumar, and S. Srivastava, "A study of surface plasmon resonance (spr) based biosensor with improved sensitivity," *Photonics and Nanostructures-Fundamentals and Applications*, vol. 31, pp. 99–106, 2018.
- [49] P. Cao, X. Yang, S. Wang, Y. Huang, N. Wang, D. Deng, and C. T. Liu, "Ultra-strong graphene absorption induced by one-dimensional parity-time symmetric photonic crystal," *IEEE Photonics Journal*, vol. 9, no. 1, pp. 1–9, 2017.
- [50] J. Kim, M. Kasture, T. Hwang, A. Kulkarni, R. Amin, S. Park, T. Kim, and S. Gosavi, "Graphene-based waveguides: novel method for detecting biological activity," *Applied Biochemistry and Biotechnology*, vol. 167, no. 5, pp. 1069–1075, 2012.

- [51] J. A. Kim, T. Hwang, S. R. Dugasani, R. Amin, A. Kulkarni, S. H. Park, and T. Kim, "Graphene based fiber optic surface plasmon resonance for biochemical sensor applications," *Sensors and Actuators B: Chemical*, vol. 187, pp. 426–433, 2013.
- [52] P. K. Maharana and R. Jha, "Chalcogenide prism and graphene multilayer based surface plasmon resonance affinity biosensor for high performance," *Sensors and Actuators B: Chemical*, vol. 169, pp. 161–166, 2012.
- [53] K. V. Sreekanth, S. Zeng, J. Shang, K.-T. Yong, and T. Yu, "Excitation of surface electromagnetic waves in a graphene-based bragg grating," *Scientific Reports*, vol. 2, no. 1, pp. 1–7, 2012.
- [54] F. Al-Sheqefi and W. Belhadj, "Photonic band gap characteristics of one-dimensional graphene-dielectric periodic structures," *Superlattices and Microstructures*, vol. 88, pp. 127–138, 2015.
- [55] A. H. Aly and Z. A. Zaky, "Ultra-sensitive photonic crystal cancer cells sensor with a high-quality factor," *Cryogenics*, vol. 104, p. 102991, 2019.
- [56] A. H. Aly and H. A. Elsayed, "Transmittance properties of one-dimensional metallic-dielectric photonic crystals in near-zero permittivity," *Physica Scripta*, vol. 94, no. 12, p. 125501, 2019.
- [57] C. Qin, B. Wang, H. Huang, H. Long, K. Wang, and P. Lu, "Low-loss plasmonic supermodes in graphene multilayers," *Optics Express*, vol. 22, no. 21, pp. 25324–25332, 2014.
- [58] H. Hajian, H. Caglayan, and E. Ozbay, "Long-range tamm surface plasmons supported by graphene-dielectric metamaterials," *Journal of Applied Physics*, vol. 121, no. 3, p. 033101, 2017.
- [59] Y. Xiang, X. Dai, J. Guo, H. Zhang, S. Wen, and D. Tang, "Critical coupling with graphene-based hyperbolic metamaterials," *Scientific Reports*, vol. 4, no. 1, pp. 1–7, 2014.

- [60] A. A. Sayem, M. Rahman, M. Mahdy, I. Jahangir, *et al.*, “Negative refraction with superior transmission in graphene-hexagonal boron nitride (hbn) multi-layer hyper crystal,” *Scientific Reports*, vol. 6, no. 1, pp. 1–11, 2016.
- [61] X. Wang, X. Jiang, Q. You, J. Guo, X. Dai, and Y. Xiang, “Tunable and multichannel terahertz perfect absorber due to tamm surface plasmons with graphene,” *Photonics Research*, vol. 5, no. 6, pp. 536–542, 2017.
- [62] A. Kavokin, I. Shelykh, and G. Malpuech, “Lossless interface modes at the boundary between two periodic dielectric structures,” *Physical Review B*, vol. 72, no. 23, p. 233102, 2005.
- [63] J. Hu, Y. Huang, Y. Chen, J. Wu, J. Wang, *et al.*, “High-sensitivity multi-channel refractive-index sensor based on a graphene-based hybrid tamm plasmonic structure,” *Optical Materials Express*, vol. 11, no. 11, pp. 3833–3843, 2021.
- [64] B. Afinogenov, V. Bessonov, A. Nikulin, and A. Fedyanin, “Observation of hybrid state of tamm and surface plasmon-polaritons in one-dimensional photonic crystals,” *Applied Physics Letters*, vol. 103, no. 6, p. 061112, 2013.
- [65] S. Kumar, M. K. Shukla, P. S. Maji, and R. Das, “Self-referenced refractive index sensing with hybrid-tamm-plasmon-polariton modes in sub-wavelength analyte layers,” *Journal of Physics D: Applied Physics*, vol. 50, no. 37, p. 375106, 2017.
- [66] P. S. Maji, M. K. Shukla, and R. Das, “Blood component detection based on miniaturized self-referenced hybrid tamm-plasmon-polariton sensor,” *Sensors and Actuators B: Chemical*, vol. 255, pp. 729–734, 2018.
- [67] Z. A. Zaky and A. H. Aly, “Modeling of a biosensor using tamm resonance excited by graphene,” *Applied Optics*, vol. 60, no. 5, pp. 1411–1419, 2021.

- [68] H. Su, T. Jiang, R. Zhou, Z. Li, Z. Peng, S. Wang, M. Zhang, H. Liang, I. L. Li, and S. Ruan, "High-sensitivity terahertz sensor based on tamm plasmon polaritons of a graphene asymmetric structure," *JOSA B*, vol. 38, no. 6, pp. 1877–1884, 2021.
- [69] M. M. Keshavarz and A. Alighanbari, "Terahertz refractive index sensor based on tamm plasmon-polaritons with graphene," *Applied Optics*, vol. 58, no. 13, pp. 3604–3612, 2019.
- [70] B. Ferguson and X.-C. Zhang, "Materials for terahertz science and technology," *Nature Materials*, vol. 1, no. 1, pp. 26–33, 2002.
- [71] W. Withayachumnankul, J. F. O'ÁZ'Hara, W. Cao, I. Al-Naib, and W. Zhang, "Limitation in thin-film sensing with transmission-mode terahertz time-domain spectroscopy," *Optics Express*, vol. 22, no. 1, pp. 972–986, 2014.
- [72] D. T. Gilbertson, J. P. Ebben, R. N. Foley, E. D. Weinhandl, B. D. Bradbury, and A. J. Collins, "Hemoglobin level variability: associations with mortality," *Clinical Journal of the American Society of Nephrology*, vol. 3, no. 1, pp. 133–138, 2008.
- [73] T. B. Drüeke, F. Locatelli, N. Clyne, K.-U. Eckardt, I. C. Macdougall, D. Tsakiris, H.-U. Burger, and A. Scherhag, "Normalization of hemoglobin level in patients with chronic kidney disease and anemia," *New England Journal of Medicine*, vol. 355, no. 20, pp. 2071–2084, 2006.
- [74] S. Mostufa, A. K. Paul, and K. Chakrabarti, "Detection of hemoglobin in blood and urine glucose level samples using a graphene-coated spr based biosensor," *OSA Continuum*, vol. 4, no. 8, pp. 2164–2176, 2021.
- [75] A. K. Ajad, M. J. Islam, M. R. Kaysir, and J. Atai, "Highly sensitive bio sensor based on wgm ring resonator for hemoglobin detection in blood samples," *Optik*, vol. 226, p. 166009, 2021.

- [76] E. Mauriz, “Recent progress in plasmonic biosensing schemes for virus detection,” *Sensors*, vol. 20, no. 17, p. 4745, 2020.
- [77] X. Peng, Y. Zhou, K. Nie, F. Zhou, Y. Yuan, J. Song, and J. Qu, “Promising near-infrared plasmonic biosensor employed for specific detection of sars-cov-2 and its spike glycoprotein,” *New Journal of Physics*, vol. 22, no. 10, p. 103046, 2020.
- [78] G. Qiu, Z. Gai, Y. Tao, J. Schmitt, G. A. Kullak-Ublick, and J. Wang, “Dual-functional plasmonic photothermal biosensors for highly accurate severe acute respiratory syndrome coronavirus 2 detection,” *ACS Nano*, vol. 14, no. 5, pp. 5268–5277, 2020.
- [79] G.-S. Park, K. Ku, S.-H. Baek, S.-J. Kim, S. I. Kim, B.-T. Kim, and J.-S. Maeng, “Development of reverse transcription loop-mediated isothermal amplification assays targeting severe acute respiratory syndrome coronavirus 2 (sars-cov-2),” *The Journal of Molecular Diagnostics*, vol. 22, no. 6, pp. 729–735, 2020.
- [80] X. Zhu, X. Wang, L. Han, T. Chen, L. Wang, H. Li, S. Li, L. He, X. Fu, S. Chen, *et al.*, “Reverse transcription loop-mediated isothermal amplification combined with nanoparticles-based biosensor for diagnosis of covid-19,” *MedRxiv*, 2020.
- [81] H. Hossein, K. M. Ali, M. Hosseini, A. Sarveazad, S. Safari, and M. Yousefifard, “Value of chest computed tomography scan in diagnosis of covid-19; a systematic review and meta-analysis,” *Clinical and Translational Imaging*, vol. 8, no. 6, pp. 469–481, 2020.
- [82] M. Egger, C. Bundschuh, K. Wiesinger, C. Gabriel, M. Clodi, T. Mueller, and B. Dieplinger, “Comparison of the elecsys® anti-sars-cov-2 immunoassay with the edia® enzyme linked immunosorbent assays for the detection of sars-cov-2 antibodies in human plasma,” *Clinica Chimica Acta*, vol. 509, pp. 18–21, 2020.

- [83] Y. Fang, H. Zhang, J. Xie, M. Lin, L. Ying, P. Pang, and W. Ji, "Sensitivity of chest ct for covid-19: comparison to rt-pcr," *Radiology*, 2020.
- [84] N. A. S. Omar, Y. W. Fen, J. Abdullah, A. R. Sadrolhosseini, Y. Mustapha Kamil, N. â. M. Fauzi, H. S. Hashim, and M. A. Mahdi, "Quantitative and selective surface plasmon resonance response based on a reduced graphene oxide–polyamidoamine nanocomposite for detection of dengue virus e-proteins," *Nanomaterials*, vol. 10, no. 3, p. 569, 2020.
- [85] Z. Omair and M. A. Talukder, "Sensitivity analysis of gold nanorod biosensors for single molecule detection," *Plasmonics*, vol. 14, no. 6, pp. 1611–1619, 2019.
- [86] J.-H. Lee, B.-C. Kim, B.-K. Oh, and J.-W. Choi, "Highly sensitive localized surface plasmon resonance immunosensor for label-free detection of hiv-1," *Nanomedicine: Nanotechnology, Biology and Medicine*, vol. 9, no. 7, pp. 1018–1026, 2013.
- [87] A. Ahmadvand, B. Gerislioglu, Z. Ramezani, A. Kaushik, P. Manickam, and S. A. Ghoreishi, "Femtomolar-level detection of sars-cov-2 spike proteins using toroidal plasmonic metasensors," *arXiv preprint arXiv:2006.08536*, 2020.
- [88] G. Seo, G. Lee, M. J. Kim, S.-H. Baek, M. Choi, K. B. Ku, C.-S. Lee, S. Jun, D. Park, H. G. Kim, *et al.*, "Rapid detection of covid-19 causative virus (sars-cov-2) in human nasopharyngeal swab specimens using field-effect transistor-based biosensor," *ACS Nano*, vol. 14, no. 4, pp. 5135–5142, 2020.
- [89] E. Buzavaite-Verteliene, I. Plikusiene, T. Tolenis, A. Valavicius, J. Anulyte, A. Ramanavicius, and Z. Balevicius, "Hybrid tamm-surface plasmon polariton mode for highly sensitive detection of protein interactions," *Optics Express*, vol. 28, no. 20, pp. 29033–29043, 2020.

- [90] M. Baitimirova, R. Viter, J. Andzane, A. van der Lee, D. Voiry, I. Iatsunskyi, E. Coy, L. Mikoliunaite, S. Tumenas, K. Załeński, *et al.*, “Tuning of structural and optical properties of graphene/zno nanolaminates,” *The Journal of Physical Chemistry C*, vol. 120, no. 41, pp. 23716–23725, 2016.
- [91] M. M. Hossain and M. A. Talukder, “Gate-controlled graphene surface plasmon resonance glucose sensor,” *Optics Communications*, vol. 493, p. 126994, 2021.
- [92] X. Y. He and R. Li, “Comparison of graphene-based transverse magnetic and electric surface plasmon modes,” *IEEE Journal of Selected Topics in Quantum Electronics*, vol. 20, no. 1, pp. 62–67, 2013.
- [93] A. Vakil and N. Engheta, “Transformation optics using graphene,” *Science*, vol. 332, no. 6035, pp. 1291–1294, 2011.
- [94] F. H. Koppens, D. E. Chang, and F. J. García de Abajo, “Graphene plasmonics: a platform for strong light–matter interactions,” *Nano Letters*, vol. 11, no. 8, pp. 3370–3377, 2011.
- [95] G. W. Hanson, “Dyadic green’s functions and guided surface waves for a surface conductivity model of graphene,” *Journal of Applied Physics*, vol. 103, no. 6, p. 064302, 2008.
- [96] D. A. Kuzmin, I. V. Bychkov, V. G. Shavrov, and L. N. Kotov, “Transverse-electric plasmonic modes of cylindrical graphene-based waveguide at near-infrared and visible frequencies,” *Scientific Reports*, vol. 6, no. 1, pp. 1–6, 2016.
- [97] L. Ju, B. Geng, J. Horng, C. Girit, M. Martin, Z. Hao, H. A. Bechtel, X. Liang, A. Zettl, Y. R. Shen, *et al.*, “Graphene plasmonics for tunable terahertz metamaterials,” *Nature Nanotechnology*, vol. 6, no. 10, pp. 630–634, 2011.
- [98] F. Ramos-Mendieta, J. Hernández-López, and M. Palomino-Ovando, “Transverse magnetic surface plasmons and complete absorption supported by doped graphene in otto configuration,” *AIP Advances*, vol. 4, no. 6, p. 067125, 2014.

- [99] X. Zhu, W. Yan, P. Uhd Jepsen, O. Hansen, N. Asger Mortensen, and S. Xiao, “Experimental observation of plasmons in a graphene monolayer resting on a two-dimensional subwavelength silicon grating,” *Applied Physics Letters*, vol. 102, no. 13, p. 131101, 2013.
- [100] D.-W. Huang, Y.-F. Ma, M.-J. Sung, and C.-P. Huang, “Approach the angular sensitivity limit in surface plasmon resonance sensors with low index prism and large resonant angle,” *Optical Engineering*, vol. 49, no. 5, p. 054403, 2010.
- [101] A. Dhawan, M. Canva, and T. Vo-Dinh, “Narrow groove plasmonic nano-gratings for surface plasmon resonance sensing,” *Optics Express*, vol. 19, no. 2, pp. 787–813, 2011.
- [102] A. Polyakov, K. Thompson, S. Dhuey, D. Olynick, S. Cabrini, P. Schuck, and H. Padmore, “Plasmon resonance tuning in metallic nanocavities,” *Scientific Reports*, vol. 2, no. 1, pp. 1–5, 2012.
- [103] M. H. Elshorbagy, A. Cuadrado, and J. Alda, “Plasmonic sensor based on dielectric nanoprisms,” *Nanoscale Research Letters*, vol. 12, no. 1, pp. 1–7, 2017.
- [104] M. Burrese, D. Van Oosten, T. Kampfrath, H. Schoenmaker, R. Heideman, A. Leinse, and L. Kuipers, “Probing the magnetic field of light at optical frequencies,” *Science*, vol. 326, no. 5952, pp. 550–553, 2009.
- [105] M. W. Klein, C. Enkrich, M. Wegener, and S. Linden, “Second-harmonic generation from magnetic metamaterials,” *Science*, vol. 313, no. 5786, pp. 502–504, 2006.
- [106] I. V. Shadrivov, A. B. Kozyrev, D. van der Weide, and Y. S. Kivshar, “Nonlinear magnetic metamaterials,” *Optics Express*, vol. 16, no. 25, pp. 20266–20271, 2008.

- [107] H. N. Krishnamoorthy, Z. Jacob, E. Narimanov, I. Kretzschmar, and V. M. Menon, "Topological transitions in metamaterials," *Science*, vol. 336, no. 6078, pp. 205–209, 2012.
- [108] O. Tabasi and C. Falamaki, "Recent advancements in the methodologies applied for the sensitivity enhancement of surface plasmon resonance sensors," *Analytical Methods*, vol. 10, no. 32, pp. 3906–3925, 2018.
- [109] Q. Yu, S. Chen, A. D. Taylor, J. Homola, B. Hock, and S. Jiang, "Detection of low-molecular-weight domoic acid using surface plasmon resonance sensor," *Sensors and Actuators B: Chemical*, vol. 107, no. 1, pp. 193–201, 2005.
- [110] O. Lopez-Sanchez, D. Lembke, M. Kayci, A. Radenovic, and A. Kis, "Ultra-sensitive photodetectors based on monolayer mos₂," *Nature Nanotechnology*, vol. 8, no. 7, pp. 497–501, 2013.
- [111] L. Wu, J. Guo, Q. Wang, S. Lu, X. Dai, Y. Xiang, and D. Fan, "Sensitivity enhancement by using few-layer black phosphorus-graphene/tmdcs heterostructure in surface plasmon resonance biochemical sensor," *Sensors and Actuators B: Chemical*, vol. 249, pp. 542–548, 2017.
- [112] S. Pal, Y. Prajapati, J. Saini, and V. Singh, "Sensitivity enhancement of metamaterial-based surface plasmon resonance biosensor for near infrared," *Optica Applicata*, vol. 46, no. 1, 2016.
- [113] J. Maurya, Y. Prajapati, V. Singh, J. Saini, and R. Tripathi, "Performance of graphene–mos₂ based surface plasmon resonance sensor using silicon layer," *Optical and Quantum Electronics*, vol. 47, no. 11, pp. 3599–3611, 2015.
- [114] B. Meshginqalam and J. Barvestani, "Aluminum and phosphorene based ultrasensitive spr biosensor," *Optical Materials*, vol. 86, pp. 119–125, 2018.
- [115] B. Caballero, A. García-Martín, and J. C. Cuevas, "Hybrid magnetoplasmonic crystals boost the performance of nanohole arrays as plasmonic sensors," *ACS Photonics*, vol. 3, no. 2, pp. 203–208, 2016.

- [116] Y. Zhu, H. Zhang, D. Li, Z. Zhang, S. Zhang, J. Yi, and W. Wang, “Magnetic plasmons in a simple metallic nanogroove array for refractive index sensing,” *Optics Express*, vol. 26, no. 7, pp. 9148–9154, 2018.
- [117] E. T. Papaioannou, H. Fang, B. Caballero, E. M. Akinoglu, M. Giersig, A. García-Martín, and P. Fumagalli, “Role of interactions in the magneto-plasmonic response at the geometrical threshold of surface continuity,” *Optics Express*, vol. 25, no. 26, pp. 32792–32799, 2017.
- [118] C. R. Simovski, P. A. Belov, and S. He, “Backward wave region and negative material parameters of a structure formed by lattices of wires and split-ring resonators,” *IEEE Transactions on Antennas and Propagation*, vol. 51, no. 10, pp. 2582–2591, 2003.
- [119] D. Smith, D. Vier, T. Koschny, and C. Soukoulis, “Electromagnetic parameter retrieval from inhomogeneous metamaterials,” *Physical Review E*, vol. 71, no. 3, p. 036617, 2005.
- [120] P. Markoš and C. M. Soukoulis, “Transmission properties and effective electromagnetic parameters of double negative metamaterials,” *Optics Express*, vol. 11, no. 7, pp. 649–661, 2003.
- [121] S. Arslanagić, T. V. Hansen, N. A. Mortensen, A. H. Gregersen, O. Sigmund, R. W. Ziolkowski, and O. Breinbjerg, “A review of the scattering-parameter extraction method with clarification of ambiguity issues in relation to metamaterial homogenization,” *IEEE Antennas and Propagation Magazine*, vol. 55, no. 2, pp. 91–106, 2013.
- [122] X. Chen, T. M. Grzegorzczak, B.-I. Wu, J. Pacheco Jr, and J. A. Kong, “Robust method to retrieve the constitutive effective parameters of metamaterials,” *Physical Review E*, vol. 70, no. 1, p. 016608, 2004.
- [123] S. Mayer, *Magnetic Permeability Meter Ferromaster*, 2019 (accessed January 20, 2020).

- [124] X. Zhao, T. Huang, P. S. Ping, X. Wu, P. Huang, J. Pan, Y. Wu, and Z. Cheng, "Sensitivity enhancement in surface plasmon resonance biochemical sensor based on transition metal dichalcogenides/graphene heterostructure," *Sensors*, vol. 18, no. 7, p. 2056, 2018.
- [125] W. Mukhtar, P. S. Menon, S. Shaari, M. Malek, and A. Abdullah, "Angle shifting in surface plasmon resonance: experimental and theoretical verification," *Journal of Physics: Conference Series*, vol. 431, no. 1, p. 012028, 2013.
- [126] S. Zeng, S. Hu, J. Xia, T. Anderson, X.-Q. Dinh, X.-M. Meng, P. Coquet, and K.-T. Yong, "Graphene–mos2 hybrid nanostructures enhanced surface plasmon resonance biosensors," *Sensors and Actuators B: Chemical*, vol. 207, pp. 801–810, 2015.
- [127] H. Xu, L. Wu, X. Dai, Y. Gao, and Y. Xiang, "An ultra-high sensitivity surface plasmon resonance sensor based on graphene-aluminum-graphene sandwich-like structure," *Journal of Applied Physics*, vol. 120, no. 5, p. 053101, 2016.
- [128] A. Das and M. A. Talukder, "Theoretical analysis of bimetallic nanorod dimer biosensors for label-free molecule detection," *AIP Advances*, vol. 8, no. 2, p. 025302, 2018.
- [129] D. Rodrigo, O. Limaj, D. Janner, D. Etezadi, F. J. García de Abajo, V. Pruneri, and H. Altug, "Mid-infrared plasmonic biosensing with graphene," *Science*, vol. 349, no. 6244, pp. 165–168, 2015.
- [130] C. Rockstuhl, F. Lederer, C. Etrich, T. Pertsch, and T. Scharf, "Design of an artificial three-dimensional composite metamaterial with magnetic resonances in the visible range of the electromagnetic spectrum," *Physical Review Letters*, vol. 99, no. 1, p. 017401, 2007.
- [131] L. Petrakis, "Spectral line shapes: Gaussian and lorentzian functions in magnetic resonance," *Journal of Chemical Education*, vol. 44, no. 8, p. 432, 1967.

- [132] Y.-L. Ho, Y. Lee, E. Maeda, and J.-J. Delaunay, “Coupling of localized surface plasmons to u-shaped cavities for high-sensitivity and miniaturized detectors,” *Optics Express*, vol. 21, no. 2, pp. 1531–1540, 2013.
- [133] Z. Chen, X. Zhao, C. Lin, S. Chen, L. Yin, and Y. Ding, “Figure of merit enhancement of surface plasmon resonance sensors using absentee layer,” *Applied Optics*, vol. 55, no. 25, pp. 6832–6835, 2016.
- [134] N. Maccaferri, K. E Gregorczyk, T. V. De Oliveira, M. Kataja, S. Van Dijken, Z. Pirzadeh, A. Dmitriev, J. Åkerman, M. Knez, and P. Vavassori, “Ultrasensitive and label-free molecular-level detection enabled by light phase control in magnetoplasmonic nanoantennas,” *Nature Communications*, vol. 6, no. 1, pp. 1–9, 2015.
- [135] M. A. Otte, B. Sepulveda, W. Ni, J. P. Juste, L. M. Liz-Marzán, and L. M. Lechuga, “Identification of the optimal spectral region for plasmonic and nanoplasmonic sensing,” *ACS Nano*, vol. 4, no. 1, pp. 349–357, 2010.
- [136] Y. Shen, J. Zhou, T. Liu, Y. Tao, R. Jiang, M. Liu, G. Xiao, J. Zhu, Z.-K. Zhou, X. Wang, *et al.*, “Plasmonic gold mushroom arrays with refractive index sensing figures of merit approaching the theoretical limit,” *Nature Communications*, vol. 4, no. 1, pp. 1–9, 2013.
- [137] Q. Ouyang, S. Zeng, L. Jiang, L. Hong, G. Xu, X.-Q. Dinh, J. Qian, S. He, J. Qu, P. Coquet, *et al.*, “Sensitivity enhancement of transition metal dichalcogenides/silicon nanostructure-based surface plasmon resonance biosensor,” *Scientific Reports*, vol. 6, no. 1, pp. 1–13, 2016.
- [138] A. Verma, A. Prakash, and R. Tripathi, “Sensitivity enhancement of surface plasmon resonance biosensor using graphene and air gap,” *Optics Communications*, vol. 357, pp. 106–112, 2015.

- [139] M. S. Rahman, M. S. Anower, M. R. Hasan, M. B. Hossain, and M. I. Haque, “Design and numerical analysis of highly sensitive au-mos₂-graphene based hybrid surface plasmon resonance biosensor,” *Optics Communications*, vol. 396, pp. 36–43, 2017.
- [140] S. Chen and C. Lin, “Figure of merit analysis of graphene based surface plasmon resonance biosensor for visible and near infrared,” *Optics Communications*, vol. 435, pp. 102–107, 2019.
- [141] J. Chen, C. Tang, P. Mao, C. Peng, D. Gao, Y. Yu, Q. Wang, and L. Zhang, “Surface-plasmon-polaritons-assisted enhanced magnetic response at optical frequencies in metamaterials,” *IEEE Photonics Journal*, vol. 8, no. 1, pp. 1–7, 2015.
- [142] I. D. Federation, *9th Edition of the Diabetes Atlas 2019*, accessed June 10, 2020.
- [143] S. Haxha and J. Jhoja, “Optical based noninvasive glucose monitoring sensor prototype,” *IEEE Photonics Journal*, vol. 8, no. 6, pp. 1–11, 2016.
- [144] S. K. Srivastava, R. Verma, and B. D. Gupta, “Surface plasmon resonance based fiber optic glucose biosensor,” in *Third Asia Pacific Optical Sensors Conference*, vol. 8351, pp. 451–456, SPIE, 2012.
- [145] E.-H. Yoo and S.-Y. Lee, “Glucose biosensors: an overview of use in clinical practice,” *Sensors*, vol. 10, no. 5, pp. 4558–4576, 2010.
- [146] K. Tonyushkina and J. H. Nichols, “Glucose meters: a review of technical challenges to obtaining accurate results,” *Journal of Diabetes Science and Technology*, vol. 3, no. 4, pp. 971–980, 2009.
- [147] C. Li, S. Xu, J. Yu, Z. Li, W. Li, J. Wang, A. Liu, B. Man, S. Yang, and C. Zhang, “Local hot charge density regulation: Vibration-free pyroelectric nanogenerator for effectively enhancing catalysis and in-situ surface enhanced raman scattering monitoring,” *Nano Energy*, vol. 81, p. 105585, 2021.

- [148] C. Zhang, C. Li, J. Yu, S. Jiang, S. Xu, C. Yang, Y. J. Liu, X. Gao, A. Liu, and B. Man, “Sers activated platform with three-dimensional hot spots and tunable nanometer gap,” *Sensors and Actuators B: Chemical*, vol. 258, pp. 163–171, 2018.
- [149] X. Zhao, C. Liu, J. Yu, Z. Li, L. Liu, C. Li, S. Xu, W. Li, B. Man, and C. Zhang, “Hydrophobic multiscale cavities for high-performance and self-cleaning surface-enhanced raman spectroscopy (sers) sensing,” *Nanophotonics*, vol. 9, no. 16, pp. 4761–4773, 2020.
- [150] J. Yu, M. Yang, Z. Li, C. Liu, Y. Wei, C. Zhang, B. Man, and F. Lei, “Hierarchical particle-in-quasicavity architecture for ultratrace in situ raman sensing and its application in real-time monitoring of toxic pollutants,” *Analytical Chemistry*, vol. 92, no. 21, pp. 14754–14761, 2020.
- [151] E. D’costa, I. Higgins, and A. Turner, “Quinoprotein glucose dehydrogenase and its application in an amperometric glucose sensor,” *Biosensors*, vol. 2, no. 2, pp. 71–87, 1986.
- [152] S. Shtelzer and S. Braun, “An optical biosensor based upon glucose oxidase immobilized in sol-gel silicate matrix,” *Biotechnology and Applied Biochemistry*, vol. 19, no. 3, pp. 293–305, 1994.
- [153] X. Yang, Y. Lu, M. Wang, and J. Yao, “A photonic crystal fiber glucose sensor filled with silver nanowires,” *Optics Communications*, vol. 359, pp. 279–284, 2016.
- [154] H. Thenmozhi, M. M. Rajan, V. Devika, D. Vigneswaran, and N. Ayyanar, “D-glucose sensor using photonic crystal fiber,” *Optik*, vol. 145, pp. 489–494, 2017.
- [155] S. Yang, Y. Zhang, X. Peng, Y. Lu, S. Xie, J. Li, W. Chen, Z. Jiang, J. Peng, and H. Li, “Theoretical study and experimental fabrication of high negative

- dispersion photonic crystal fiber with large area mode field,” *Optics Express*, vol. 14, no. 7, pp. 3015–3023, 2006.
- [156] P. S. Menon, F. A. Said, G. S. Mei, D. D. Berhanuddin, A. A. Umar, S. Shaari, and B. Y. Majlis, “Urea and creatinine detection on nano-laminated gold thin film using kretschmann-based surface plasmon resonance biosensor,” *PLoS One*, vol. 13, no. 7, p. e0201228, 2018.
- [157] H. H. Nguyen, J. Park, S. Kang, and M. Kim, “Surface plasmon resonance: a versatile technique for biosensor applications,” *Sensors*, vol. 15, no. 5, pp. 10481–10510, 2015.
- [158] N. N. M. Rosddi, Y. W. Fen, N. A. A. Anas, N. A. S. Omar, N. S. M. Ramdzan, and W. M. E. M. M. Daniyal, “Cationically modified nanocrystalline cellulose/carboxyl-functionalized graphene quantum dots nanocomposite thin film: Characterization and potential sensing application,” *Crystals*, vol. 10, no. 10, p. 875, 2020.
- [159] A. Panda, P. D. Pukhrambam, and G. Keiser, “Performance analysis of graphene-based surface plasmon resonance biosensor for blood glucose and gas detection,” *Applied Physics A*, vol. 126, no. 3, pp. 1–12, 2020.
- [160] N. Mudgal, A. Saharia, A. Agarwal, J. Ali, P. Yupapin, and G. Singh, “Modeling of highly sensitive surface plasmon resonance (spr) sensor for urine glucose detection,” *Optical and Quantum Electronics*, vol. 52, no. 6, pp. 1–14, 2020.
- [161] P. Alonso-González, A. Y. Nikitin, F. Golmar, A. Centeno, A. Pesquera, S. Vélez, J. Chen, G. Navickaite, F. Koppens, A. Zurutuza, *et al.*, “Controlling graphene plasmons with resonant metal antennas and spatial conductivity patterns,” *Science*, vol. 344, no. 6190, pp. 1369–1373, 2014.
- [162] M. S. Rahman, M. R. Hasan, K. A. Rikta, and M. Anower, “A novel graphene coated surface plasmon resonance biosensor with tungsten disulfide (ws₂) for sensing dna hybridization,” *Optical Materials*, vol. 75, pp. 567–573, 2018.

- [163] B. Deng, Q. Guo, C. Li, H. Wang, X. Ling, D. B. Farmer, S.-j. Han, J. Kong, and F. Xia, “Coupling-enhanced broadband mid-infrared light absorption in graphene plasmonic nanostructures,” *ACS Nano*, vol. 10, no. 12, pp. 11172–11178, 2016.
- [164] Z. Yu and S. Fan, “Extraordinarily high spectral sensitivity in refractive index sensors using multiple optical modes,” *Optics Express*, vol. 19, no. 11, pp. 10029–10040, 2011.
- [165] Y. Kaneoka, K. Nishigaki, Y. Mizutani, and T. Iwata, “Precise measurement of the thickness of a dielectric layer on a metal surface by use of a modified otto optical configuration,” *International Journal of Optomechatronics*, vol. 9, no. 1, pp. 48–61, 2015.
- [166] B. Yektaparast and H. Shirkani, “Controlling optical absorption of graphene in near-infrared region by surface plasmons,” *Plasmonics*, vol. 13, no. 5, pp. 1623–1630, 2018.
- [167] C. R. Dean, A. F. Young, I. Meric, C. Lee, L. Wang, S. Sorgenfrei, K. Watanabe, T. Taniguchi, P. Kim, K. L. Shepard, *et al.*, “Boron nitride substrates for high-quality graphene electronics,” *Nature Nanotechnology*, vol. 5, no. 10, pp. 722–726, 2010.
- [168] A. Woessner, M. B. Lundberg, Y. Gao, A. Principi, P. Alonso-González, M. Carrega, K. Watanabe, T. Taniguchi, G. Vignale, M. Polini, *et al.*, “Highly confined low-loss plasmons in graphene–boron nitride heterostructures,” *Nature Materials*, vol. 14, no. 4, pp. 421–425, 2015.
- [169] J. Hu, Y. Qing, S. Yang, Y. Ren, X. Wu, W. Gao, and C. Wu, “Tailoring total absorption in a graphene monolayer covered subwavelength multilayer dielectric grating structure at near-infrared frequencies,” *JOSA B*, vol. 34, no. 4, pp. 861–868, 2017.

- [170] Y. Yin, Z. Cheng, L. Wang, K. Jin, and W. Wang, "Graphene, a material for high temperature devices—intrinsic carrier density, carrier drift velocity and lattice energy," *Scientific Reports*, vol. 4, no. 1, pp. 1–6, 2014.
- [171] M. Kim, C. Y. Jeong, H. Heo, and S. Kim, "Optical reflection modulation using surface plasmon resonance in a graphene-embedded hybrid plasmonic waveguide at an optical communication wavelength," *Optics Letters*, vol. 40, no. 6, pp. 871–874, 2015.
- [172] C.-W. Lin, K.-P. Chen, C.-N. Hsiao, S. Lin, and C.-K. Lee, "Design and fabrication of an alternating dielectric multi-layer device for surface plasmon resonance sensor," *Sensors and Actuators B: Chemical*, vol. 113, no. 1, pp. 169–176, 2006.
- [173] G. Lan, S. Liu, Y. Ma, X. Zhang, Y. Wang, and Y. Song, "Sensitivity and figure-of-merit enhancements of liquid-prism spr sensor in the angular interrogation," *Optics Communications*, vol. 352, pp. 49–54, 2015.
- [174] P. K. Maharana, T. Srivastava, and R. Jha, "On the performance of highly sensitive and accurate graphene-on-aluminum and silicon-based spr biosensor for visible and near infrared," *Plasmonics*, vol. 9, no. 5, pp. 1113–1120, 2014.
- [175] S. Z. Uddin and M. A. Talukder, "Two-dimensional materials for improved resolution in total internal reflection fluorescence microscopy," *Materials Research Express*, vol. 4, no. 9, p. 096203, 2017.
- [176] P. R. Gray, P. J. Hurst, S. H. Lewis, and R. G. Meyer, *Analysis and Design of Analog Integrated Circuits*. John Wiley & Sons Ltd., New Jersey, 2009.
- [177] E. D. Palik, *Handbook of Optical Constants of Solids*, vol. 3. Academic Press Ltd., Washington., 1998.
- [178] A. Al Sayem, M. R. C. Mahdy, I. Jahangir, and M. S. Rahman, "Ultrathin ultra-broadband electro-absorption modulator based on few-layer graphene

- based anisotropic metamaterial,” *Optics Communications*, vol. 384, pp. 50–58, 2017.
- [179] Q. Bao, H. Zhang, B. Wang, Z. Ni, C. H. Y. X. Lim, Y. Wang, D. Y. Tang, and K. P. Loh, “Broadband graphene polarizer,” *Nature Photonics*, vol. 5, no. 7, pp. 411–415, 2011.
- [180] W. Gao, J. Shu, C. Qiu, and Q. Xu, “Excitation of plasmonic waves in graphene by guided-mode resonances,” *ACS Nano*, vol. 6, no. 9, pp. 7806–7813, 2012.
- [181] V. E. Dorgan, M.-H. Bae, and E. Pop, “Mobility and saturation velocity in graphene on sio 2,” *Applied Physics Letters*, vol. 97, no. 8, p. 082112, 2010.
- [182] K. I. Bolotin, K. J. Sikes, Z. Jiang, M. Klima, G. Fudenberg, J. Hone, P. Kim, and H. L. Stormer, “Ultrahigh electron mobility in suspended graphene,” *Solid State Communications*, vol. 146, no. 9-10, pp. 351–355, 2008.
- [183] N. I. of Diabetes, Digestive, and K. Diseases, *Diabetes*, 2020 (accessed June 10, 2020).
- [184] P. H. Marathe, H. X. Gao, and K. L. Close, “American diabetes association standards of medical care in diabetes 2017,” 2017.
- [185] P. E. Cryer, L. Axelrod, A. B. Grossman, S. R. Heller, V. M. Montori, E. R. Seaquist, and F. J. Service, “Evaluation and management of adult hypoglycemic disorders: an endocrine society clinical practice guideline,” *The Journal of Clinical Endocrinology & Metabolism*, vol. 94, no. 3, pp. 709–728, 2009.
- [186] J. Yan, K. S. Thygesen, and K. W. Jacobsen, “Nonlocal screening of plasmons in graphene by semiconducting and metallic substrates: first-principles calculations,” *Physical Review Letters*, vol. 106, no. 14, p. 146803, 2011.

- [187] B. Lahiri, S. G. McMeekin, M. Richard, and N. P. Johnson, “Enhanced fano resonance of organic material films deposited on arrays of asymmetric splitting resonators (a-srrs),” *Optics Express*, vol. 21, no. 8, pp. 9343–9352, 2013.
- [188] L. Tong, H. Wei, S. Zhang, and H. Xu, “Recent advances in plasmonic sensors,” *Sensors*, vol. 14, no. 5, pp. 7959–7973, 2014.
- [189] Z. Cheng, Q. Zhou, C. Wang, Q. Li, C. Wang, and Y. Fang, “Toward intrinsic graphene surfaces: a systematic study on thermal annealing and wet-chemical treatment of sio₂-supported graphene devices,” *Nano Letters*, vol. 11, no. 2, pp. 767–771, 2011.
- [190] Q. Bao, H. Zhang, Y. Wang, Z. Ni, Y. Yan, Z. X. Shen, K. P. Loh, and D. Y. Tang, “Atomic-layer graphene as a saturable absorber for ultrafast pulsed lasers,” *Advanced Functional Materials*, vol. 19, no. 19, pp. 3077–3083, 2009.
- [191] S. G. Menabde, D. R. Mason, E. E. Kornev, C. Lee, and N. Park, “Direct optical probing of transverse electric mode in graphene,” *Scientific Reports*, vol. 6, no. 1, pp. 1–6, 2016.
- [192] P. K. Maharana, P. Padhy, and R. Jha, “On the field enhancement and performance of an ultra-stable spr biosensor based on graphene,” *IEEE Photonics Technology Letters*, vol. 25, no. 22, pp. 2156–2159, 2013.
- [193] K. H. Zou, K. Tuncali, and S. G. Silverman, “Correlation and simple linear regression,” *Radiology*, vol. 227, no. 3, pp. 617–628, 2003.
- [194] M. Englert, P. Hartmann, and S. Reichel, “Optical glass: refractive index change with wavelength and temperature,” in *Optical Modelling and Design III*, vol. 9131, pp. 125–138, SPIE, 2014.
- [195] D. Jin-Xiang, Z. Xiao-Kang, Y. Qian, W. Xu-Yang, C. Guang-Hua, and H. De-Yan, “Optical properties of hexagonal boron nitride thin films deposited by radio frequency bias magnetron sputtering,” *Chinese Physics B*, vol. 18, no. 9, p. 4013, 2009.

- [196] J. Matsuoka, N. Kitamura, S. Fujinaga, T. Kitaoka, and H. Yamashita, “Temperature dependence of refractive index of SiO_2 glass,” *Journal of Non-crystalline Solids*, vol. 135, no. 1, pp. 86–89, 1991.
- [197] G. Jellison Jr and F. Modine, “Optical functions of silicon at elevated temperatures,” *Journal of Applied Physics*, vol. 76, no. 6, pp. 3758–3761, 1994.
- [198] F. Zhu, X. Lin, P. Liu, K. Jiang, Y. Wei, Y. Wu, J. Wang, and S. Fan, “Heating graphene to incandescence and the measurement of its work function by the thermionic emission method,” *Nano Research*, vol. 7, no. 4, pp. 553–560, 2014.
- [199] K. Ujihara, “Reflectivity of metals at high temperatures,” *Journal of Applied Physics*, vol. 43, no. 5, pp. 2376–2383, 1972.
- [200] W. Lawrence, “Electron-electron scattering in the low-temperature resistivity of the noble metals,” *Physical Review B*, vol. 13, no. 12, p. 5316, 1976.
- [201] T. Holstein, “Optical and infrared volume absorptivity of metals,” *Physical Review*, vol. 96, no. 2, p. 535, 1954.
- [202] D. Meyer, A. Hewson, and R. Bulla, “Gap formation and soft phonon mode in the holstein model,” *Physical Review Letters*, vol. 89, no. 19, p. 196401, 2002.
- [203] Y. Jiang, S. Pillai, and M. A. Green, “Re-evaluation of literature values of silver optical constants,” *Optics Express*, vol. 23, no. 3, pp. 2133–2144, 2015.
- [204] C.-Y. Tan and Y.-X. Huang, “Dependence of refractive index on concentration and temperature in electrolyte solution, polar solution, nonpolar solution, and protein solution,” *Journal of Chemical & Engineering Data*, vol. 60, no. 10, pp. 2827–2833, 2015.
- [205] S. Kang, M. Yang, Z. Hong, L. Zhang, Z. Huang, X. Chen, S. He, Z. Zhou, Z. Zhou, Q. Chen, *et al.*, “Crystal structure of sars-cov-2 nucleocapsid protein rna binding domain reveals potential unique drug targeting sites,” *Acta Pharmaceutica Sinica B*, vol. 10, no. 7, pp. 1228–1238, 2020.

- [206] P. K. Kumar, "Monitoring intact viruses using aptamers," *Biosensors*, vol. 6, no. 3, p. 40, 2016.
- [207] D. Wrapp, N. Wang, K. S. Corbett, J. A. Goldsmith, C.-L. Hsieh, O. Abiona, B. S. Graham, and J. S. McLellan, "Cryo-em structure of the 2019-ncov spike in the prefusion conformation," *Science*, vol. 367, no. 6483, pp. 1260–1263, 2020.
- [208] S. Priyadarsini, S. Mohanty, S. Mukherjee, S. Basu, and M. Mishra, "Graphene and graphene oxide as nanomaterials for medicine and biology application," *Journal of Nanostructure in Chemistry*, vol. 8, no. 2, pp. 123–137, 2018.
- [209] J. Maurya and Y. Prajapati, "A comparative study of different metal and prism in the surface plasmon resonance biosensor having mos2-graphene," *Optical and Quantum Electronics*, vol. 48, no. 5, pp. 1–12, 2016.
- [210] C. Lin and S. Chen, "Design of highly sensitive guided-wave surface plasmon resonance biosensor with deep dip using genetic algorithm," *Optics Communications*, vol. 445, pp. 155–160, 2019.
- [211] K. Li, L. Li, N. Xu, X. Peng, Y. Zhou, Y. Yuan, J. Song, and J. Qu, "Ultra-sensitive surface plasmon resonance biosensor using blue phosphorus-graphene architecture," *Sensors*, vol. 20, no. 11, p. 3326, 2020.
- [212] Y. Feng, Y. Liu, and J. Teng, "Design of an ultrasensitive spr biosensor based on a graphene-mos 2 hybrid structure with a mgf 2 prism," *Applied Optics*, vol. 57, no. 14, pp. 3639–3644, 2018.
- [213] T. Xue, W. Liang, Y. Li, Y. Sun, Y. Xiang, Y. Zhang, Z. Dai, Y. Duo, L. Wu, K. Qi, *et al.*, "Ultrasensitive detection of mirna with an antimonene-based surface plasmon resonance sensor," *Nature Communications*, vol. 10, no. 1, pp. 1–9, 2019.

- [214] V. Georgakilas, M. Otyepka, A. B. Bourlinos, V. Chandra, N. Kim, K. C. Kemp, P. Hobza, R. Zboril, and K. S. Kim, “Functionalization of graphene: covalent and non-covalent approaches, derivatives and applications,” *Chemical Reviews*, vol. 112, no. 11, pp. 6156–6214, 2012.
- [215] Y. Huang, X. Dong, Y. Shi, C. M. Li, L.-J. Li, and P. Chen, “Nanoelectronic biosensors based on cvd grown graphene,” *Nanoscale*, vol. 2, no. 8, pp. 1485–1488, 2010.
- [216] R. Lu, X. Zhao, J. Li, P. Niu, B. Yang, H. Wu, W. Wang, H. Song, B. Huang, N. Zhu, *et al.*, “Genomic characterisation and epidemiology of 2019 novel coronavirus: implications for virus origins and receptor binding,” *The Lancet*, vol. 395, no. 10224, pp. 565–574, 2020.
- [217] S. Shen, T. H. Tan, and Y.-J. Tan, “Expression, glycosylation, and modification of the spike (s) glycoprotein of sars cov,” *Glycovirolgy Protocols*, pp. 127–135, 2007.
- [218] X. Ou, Y. Liu, X. Lei, P. Li, D. Mi, L. Ren, L. Guo, R. Guo, T. Chen, J. Hu, *et al.*, “Characterization of spike glycoprotein of sars-cov-2 on virus entry and its immune cross-reactivity with sars-cov,” *Nature Communications*, vol. 11, no. 1, pp. 1–12, 2020.
- [219] K. A. Peterlinz, R. M. Georgiadis, T. M. Herne, and M. J. Tarlov, “Observation of hybridization and dehybridization of thiol-tethered dna using two-color surface plasmon resonance spectroscopy,” *Journal of the American Chemical Society*, vol. 119, no. 14, pp. 3401–3402, 1997.
- [220] R. Reitmeier, V. Sivertz, and H. Tartar, “Some properties of monoethanolamine and its aqueous solutions,” *Journal of the American Chemical Society*, vol. 62, no. 8, pp. 1943–1944, 1940.

- [221] D. H. Kim, H. G. Oh, W. H. Park, D. C. Jeon, K. M. Lim, H. J. Kim, B. K. Jang, and K. S. Song, "Detection of alpha-fetoprotein in hepatocellular carcinoma patient plasma with graphene field-effect transistor," *Sensors*, vol. 18, no. 11, p. 4032, 2018.
- [222] G. A. Perchetti, M.-L. Huang, V. Peddu, K. R. Jerome, and A. L. Greninger, "Stability of sars-cov-2 in phosphate-buffered saline for molecular detection," *Journal of Clinical Microbiology*, vol. 58, no. 8, pp. e01094–20, 2020.
- [223] V. T. Hoang, G. Stępniewski, K. H. Czarnecka, R. Kasztelanica, V. C. Long, K. D. Xuan, L. Shao, M. Śmietana, and R. Buczyński, "Optical properties of buffers and cell culture media for optofluidic and sensing applications," *Applied Sciences*, vol. 9, no. 6, p. 1145, 2019.
- [224] C. Wu, X. Zhou, and J. Wei, "Localized surface plasmon resonance of silver nanotriangles synthesized by a versatile solution reaction," *Nanoscale Research Letters*, vol. 10, no. 1, pp. 1–6, 2015.
- [225] J. Yguerabide and E. E. Yguerabide, "Light-scattering submicroscopic particles as highly fluorescent analogs and their use as tracer labels in clinical and biological applications: Ii. experimental characterization," *Analytical Biochemistry*, vol. 262, no. 2, pp. 157–176, 1998.
- [226] R. H. Holm, E. I. Solomon, A. Majumdar, and A. Tenderholt, "Comparative molecular chemistry of molybdenum and tungsten and its relation to hydroxylase and oxotransferase enzymes," *Coordination Chemistry Reviews*, vol. 255, no. 9-10, pp. 993–1015, 2011.
- [227] M. Wang, Y. Huo, S. Jiang, C. Zhang, C. Yang, T. Ning, X. Liu, C. Li, W. Zhang, and B. Man, "Theoretical design of a surface plasmon resonance sensor with high sensitivity and high resolution based on graphene–ws 2 hybrid nanostructures and au–ag bimetallic film," *RSC Advances*, vol. 7, no. 75, pp. 47177–47182, 2017.

- [228] S. B. Desu and D. A. Payne, “Interfacial segregation in perovskites: Iii, microstructure and electrical properties,” *Journal of the American Ceramic Society*, vol. 73, no. 11, pp. 3407–3415, 1990.
- [229] M. H. Elshorbagy, A. Cuadrado, and J. Alda, “High-sensitivity integrated devices based on surface plasmon resonance for sensing applications,” *Photonics Research*, vol. 5, no. 6, pp. 654–661, 2017.
- [230] M. Hossain, M. A. Talukder, *et al.*, “Optical magnetism in surface plasmon resonance–based sensors for enhanced performance,” *Plasmonics*, vol. 16, no. 2, pp. 581–588, 2021.
- [231] B. Ghosh, S. Nahas, S. Bhowmick, and A. Agarwal, “Electric field induced gap modification in ultrathin blue phosphorus,” *Physical Review B*, vol. 91, no. 11, p. 115433, 2015.
- [232] G.-H. Jung, S. Yoo, and Q.-H. Park, “Measuring the optical permittivity of two-dimensional materials without a priori knowledge of electronic transitions,” *Nanophotonics*, vol. 8, no. 2, pp. 263–270, 2019.
- [233] N. Umemura, K. Yoshida, and K. Kato, “Phase-matching properties of knbo 3 in the mid-infrared,” *Applied Optics*, vol. 38, no. 6, pp. 991–994, 1999.
- [234] X. Wang and S. Lan, “Optical properties of black phosphorus,” *Advances in Optics and Photonics*, vol. 8, no. 4, pp. 618–655, 2016.
- [235] Y. Mogulkoc, M. Modarresi, A. Mogulkoc, and Y. Ciftci, “Electronic and optical properties of bilayer blue phosphorus,” *Computational Materials Science*, vol. 124, pp. 23–29, 2016.
- [236] R. R. Nair, P. Blake, A. N. Grigorenko, K. S. Novoselov, T. J. Booth, T. Stauber, N. M. Peres, and A. K. Geim, “Fine structure constant defines visual transparency of graphene,” *Science*, vol. 320, no. 5881, pp. 1308–1308, 2008.

- [237] P. Y. Liu, L. Chin, W. Ser, H. Chen, C.-M. Hsieh, C.-H. Lee, K.-B. Sung, T. Ayi, P. Yap, B. Liedberg, *et al.*, “Cell refractive index for cell biology and disease diagnosis: past, present and future,” *Lab on a Chip*, vol. 16, no. 4, pp. 634–644, 2016.
- [238] H. Zhao, P. H. Brown, and P. Schuck, “On the distribution of protein refractive index increments,” *Biophysical Journal*, vol. 100, no. 9, pp. 2309–2317, 2011.
- [239] V. Ball and J. J. Ramsden, “Buffer dependence of refractive index increments of protein solutions,” *Biopolymers: Original Research on Biomolecules*, vol. 46, no. 7, pp. 489–492, 1998.
- [240] Y. Huang, C. Yang, X.-f. Xu, W. Xu, and S.-w. Liu, “Structural and functional properties of sars-cov-2 spike protein: potential antiviral drug development for covid-19,” *Acta Pharmacologica Sinica*, vol. 41, no. 9, pp. 1141–1149, 2020.
- [241] Y. W. Fen, W. Yunus, and N. A. Yusof, “Optical properties of cross-linked chitosan thin film for copper ion detection using surface plasmon resonance technique,” *Opt. Appl*, vol. 41, no. 4, pp. 999–1013, 2011.
- [242] H. Tombuloglu, H. Sabit, E. Al-Suhaimi, R. Al Jindan, and K. R. Alkharsah, “Development of multiplex real-time rt-pcr assay for the detection of sars-cov-2,” *Plos One*, vol. 16, no. 4, p. e0250942, 2021.
- [243] L. Falzone, N. Musso, G. Gattuso, D. Bongiorno, C. I. Palermo, G. Scalia, M. Libra, and S. Stefani, “Sensitivity assessment of droplet digital pcr for sars-cov-2 detection,” *International Journal of Molecular Medicine*, vol. 46, no. 3, pp. 957–964, 2020.
- [244] A. Alekseenko, D. Barrett, Y. Pareja-Sanchez, R. J. Howard, E. Strandback, H. Ampah-Korsah, U. Rovšnik, S. Zuniga-Veliz, A. Klenov, J. Malloo, *et al.*, “Direct detection of sars-cov-2 using non-commercial rt-lamp reagents on heat-inactivated samples,” *Scientific Reports*, vol. 11, no. 1, pp. 1–10, 2021.

- [245] R. Funari, K.-Y. Chu, and A. Q. Shen, “Detection of antibodies against sars-cov-2 spike protein by gold nanospikes in an opto-microfluidic chip,” *Biosensors and Bioelectronics*, vol. 169, p. 112578, 2020.
- [246] A. A. Rifat, G. A. Mahdiraji, Y. M. Sua, R. Ahmed, Y. Shee, and F. M. Adikan, “Highly sensitive multi-core flat fiber surface plasmon resonance refractive index sensor,” *Optics Express*, vol. 24, no. 3, pp. 2485–2495, 2016.
- [247] F. Haider, R. A. Aoni, R. Ahmed, and A. E. Miroshnichenko, “Highly amplitude-sensitive photonic-crystal-fiber-based plasmonic sensor,” *JOSA B*, vol. 35, no. 11, pp. 2816–2821, 2018.
- [248] J. Li, D. Han, J. Zeng, J. Deng, N. Hu, and J. Yang, “Multi-channel surface plasmon resonance biosensor using prism-based wavelength interrogation,” *Optics Express*, vol. 28, no. 9, pp. 14007–14017, 2020.
- [249] P. L. Kastritis and A. M. Bonvin, “On the binding affinity of macromolecular interactions: daring to ask why proteins interact,” *Journal of The Royal Society Interface*, vol. 10, no. 79, p. 20120835, 2013.
- [250] M. S. Salahudeen and P. S. Nishtala, “An overview of pharmacodynamic modelling, ligand-binding approach and its application in clinical practice,” *Saudi Pharmaceutical Journal*, vol. 25, no. 2, pp. 165–175, 2017.
- [251] R. M. Hoet, E. H. Cohen, R. B. Kent, K. Rookey, S. Schoonbroodt, S. Hogan, L. Rem, N. Frans, M. Daukandt, H. Pieters, *et al.*, “Generation of high-affinity human antibodies by combining donor-derived and synthetic complementarity-determining-region diversity,” *Nature Biotechnology*, vol. 23, no. 3, pp. 344–348, 2005.
- [252] W. Zheng, B. Han, E. Siyu, Y. Sun, X. Li, Y. Cai, and Y.-n. Zhang, “Highly-sensitive and reflective glucose sensor based on optical fiber surface plasmon resonance,” *Microchemical Journal*, vol. 157, p. 105010, 2020.

- [253] S. Z. Uddin, M. R. Tanvir, and M. A. Talukder, “A proposal and a theoretical analysis of an enhanced surface plasmon coupled emission structure for single molecule detection,” *Journal of Applied Physics*, vol. 119, no. 20, p. 204701, 2016.
- [254] H. Ditlbacher, J. R. Krenn, G. Schider, A. Leitner, and F. R. Aussenegg, “Two-dimensional optics with surface plasmon polaritons,” *Applied Physics Letters*, vol. 81, no. 10, pp. 1762–1764, 2002.
- [255] M. Hajati and Y. Hajati, “Plasmonic characteristics of two vertically coupled graphene-coated nanowires integrated with substrate,” *Applied Optics*, vol. 56, no. 4, pp. 870–875, 2017.
- [256] M. Moznuzzaman, M. R. Islam, M. B. Hossain, and I. M. Mehedi, “Modeling of highly improved spr sensor for formalin detection,” *Results in Physics*, vol. 16, p. 102874, 2020.
- [257] A. Kumar, A. K. Yadav, A. S. Kushwaha, and S. Srivastava, “A comparative study among ws₂, mos₂ and graphene based surface plasmon resonance (spr) sensor,” *Sensors and Actuators Reports*, vol. 2, no. 1, p. 100015, 2020.
- [258] T. B. A. Akib, S. F. Mou, M. M. Rahman, M. M. Rana, M. R. Islam, I. M. Mehedi, M. P. Mahmud, and A. Z. Kouzani, “Design and numerical analysis of a graphene-coated spr biosensor for rapid detection of the novel coronavirus,” *Sensors*, vol. 21, no. 10, p. 3491, 2021.
- [259] Y. Jia, Z. Li, H. Wang, M. Saeed, and H. Cai, “Sensitivity enhancement of a surface plasmon resonance sensor with platinum diselenide,” *Sensors*, vol. 20, no. 1, p. 131, 2019.
- [260] A. Bijalwan, B. K. Singh, and V. Rastogi, “Surface plasmon resonance-based sensors using nano-ribbons of graphene and wse₂,” *Plasmonics*, vol. 15, no. 4, pp. 1015–1023, 2020.

- [261] E. Buzavaite-Verteliene, A. Valavicius, L. Grineviciute, T. Tolenis, R. Lukose, G. Niaura, and Z. Balevicius, “Influence of the graphene layer on the strong coupling in the hybrid tamm-plasmon polariton mode,” *Optics Express*, vol. 28, no. 7, pp. 10308–10319, 2020.
- [262] J. Hu, E. Yao, W. Xie, W. Liu, D. Li, Y. Lu, and Q. Zhan, “Strong longitudinal coupling of tamm plasmon polaritons in graphene/dbr/ag hybrid structure,” *Optics Express*, vol. 27, no. 13, pp. 18642–18652, 2019.
- [263] H. Hajian, A. Soltani-Vala, and M. Kalafi, “Characteristics of band structure and surface plasmons supported by a one-dimensional graphene-dielectric photonic crystal,” *Optics Communications*, vol. 292, pp. 149–157, 2013.
- [264] K. V. Sreekanth, S. Zeng, K.-T. Yong, and T. Yu, “Sensitivity enhanced biosensor using graphene-based one-dimensional photonic crystal,” *Sensors and Actuators B: Chemical*, vol. 182, pp. 424–428, 2013.
- [265] Y. V. Bludov, N. Peres, G. Smirnov, and M. Vasilevskiy, “Scattering of surface plasmon polaritons in a graphene multilayer photonic crystal with inhomogeneous doping,” *Physical Review B*, vol. 93, no. 24, p. 245425, 2016.
- [266] Z. Lan, J. W. You, and N. C. Panoiu, “Nonlinear one-way edge-mode interactions for frequency mixing in topological photonic crystals,” *Physical Review B*, vol. 101, no. 15, p. 155422, 2020.
- [267] L. Qi and C. Liu, “Complex band structures of 1d anisotropic graphene photonic crystal,” *Photonics Research*, vol. 5, no. 6, pp. 543–551, 2017.
- [268] B. Roy, S. Majumder, and R. Chakraborty, “Design of low loss surface plasmon polariton waveguide and its use as hybrid tamm sensor with improved sensitivity,” *Optical Engineering*, vol. 59, no. 1, p. 017108, 2020.
- [269] K. Zhang, Y. Liu, F. Xia, S. Li, and W. Kong, “Tuning of the polariton modes induced by longitudinal strong coupling in the graphene hybridized dbr cavity,” *Optics Letters*, vol. 45, no. 13, pp. 3669–3672, 2020.

- [270] P. Törmä and W. L. Barnes, “Strong coupling between surface plasmon polaritons and emitters: a review,” *Reports on Progress in Physics*, vol. 78, no. 1, p. 013901, 2014.
- [271] A. M. Ahmed and A. Mehaney, “Ultra-high sensitive 1d porous silicon photonic crystal sensor based on the coupling of tamm/fano resonances in the mid-infrared region,” *Scientific Reports*, vol. 9, no. 1, pp. 1–9, 2019.
- [272] T. Huang, X. Dang, L. Han, G. Zhang, J. Pan, Y. Wang, and Z. Chen, “Dual-channel sensor based on tamm plasmon polariton and defect mode hybridization in topological insulator covered photonic crystals,” *JOSA B*, vol. 38, no. 6, pp. 1951–1957, 2021.
- [273] F. Ramos-Mendieta and P. Halevi, “Propagation constant-limited surface modes in dielectric superlattices,” *Optics Communications*, vol. 129, no. 1-2, pp. 1–5, 1996.
- [274] K. A. Meradi, F. Tayeboun, A. Guerinik, Z. A. Zaky, and A. H. Aly, “Optical biosensor based on enhanced surface plasmon resonance: theoretical optimization,” *Optical and Quantum Electronics*, vol. 54, no. 2, pp. 1–11, 2022.
- [275] D. Miura, H. Kimura, W. Tsugawa, K. Ikebukuro, K. Sode, and R. Asano, “Rapid, convenient, and highly sensitive detection of human hemoglobin in serum using a high-affinity bivalent antibody–enzyme complex,” *Talanta*, vol. 234, p. 122638, 2021.
- [276] E. G. Semenyuk, O. A. Stremovskiy, E. F. Edelweiss, O. V. Shirshikova, T. G. Balandin, Y. I. Buryanov, and S. M. Deyev, “Expression of single-chain antibody-barstar fusion in plants,” *Biochimie*, vol. 89, no. 1, pp. 31–38, 2007.
- [277] Y. Cao, G. K. Nguyen, J. P. Tam, and C.-F. Liu, “Butelase-mediated synthesis of protein thioesters and its application for tandem chemoenzymatic ligation,” *Chemical Communications*, vol. 51, no. 97, pp. 17289–17292, 2015.

- [278] X. Li, X.-l. Zhang, Y.-m. Cai, L. Zhang, Y. Lin, and Q. Meng, “Site specific labeling of two proteins in one system by atypical split inteins,” *International Journal of Biological Macromolecules*, vol. 109, pp. 921–931, 2018.
- [279] H. Kimura, R. Asano, N. Tsukamoto, W. Tsugawa, and K. Sode, “Convenient and universal fabrication method for antibody–enzyme complexes as sensing elements using the spycatcher/spytag system,” *Analytical Chemistry*, vol. 90, no. 24, pp. 14500–14506, 2018.
- [280] S. Azzini, G. Lheureux, C. Symonds, J.-M. Benoit, P. Senellart, A. Lemaitre, J.-J. Greffet, C. Blanchard, C. Sauvan, and J. Bellessa, “Generation and spatial control of hybrid tamm plasmon/surface plasmon modes,” *ACS Photonics*, vol. 3, no. 10, pp. 1776–1781, 2016.
- [281] R. Das, T. Srivastava, and R. Jha, “On the performance of tamm-plasmon and surface-plasmon hybrid-mode refractive-index sensor in metallo-dielectric heterostructure configuration,” *Sensors and Actuators B: Chemical*, vol. 206, pp. 443–448, 2015.
- [282] J.-T. Liu, N.-H. Liu, J. Li, X. Jing Li, and J.-H. Huang, “Enhanced absorption of graphene with one-dimensional photonic crystal,” *Applied Physics Letters*, vol. 101, no. 5, p. 052104, 2012.
- [283] B. Zhu, G. Ren, S. Zheng, Z. Lin, and S. Jian, “Nanoscale dielectric-graphene-dielectric tunable infrared waveguide with ultrahigh refractive indices,” *Optics Express*, vol. 21, no. 14, pp. 17089–17096, 2013.
- [284] G.-W. Ding, S.-B. Liu, H.-F. Zhang, X.-K. Kong, H.-M. Li, B.-X. Li, S.-Y. Liu, and H. Li, “Tunable electromagnetically induced transparency at terahertz frequencies in coupled graphene metamaterial,” *Chinese Physics B*, vol. 24, no. 11, p. 118103, 2015.
- [285] L. A. Falkovsky, “Optical properties of graphene,” *Journal of Physics: Conference Series*, vol. 129, no. 1, p. 012004, 2008.

- [286] Y. Li, L. Qi, J. Yu, Z. Chen, Y. Yao, and X. Liu, "One-dimensional multiband terahertz graphene photonic crystal filters," *Optical Materials Express*, vol. 7, no. 4, pp. 1228–1239, 2017.
- [287] L. Hu and S. Chui, "Characteristics of electromagnetic wave propagation in uniaxially anisotropic left-handed materials," *Physical Review B*, vol. 66, no. 8, p. 085108, 2002.
- [288] Z. Saleki, A. Majarshin, Y.-A. Luo, and D.-L. Zhang, "Spectral statistics of a 1d photonic crystal containing an anisotropic graphene-based hyperbolic metamaterial defect layer," *Optical Materials*, vol. 121, p. 111483, 2021.
- [289] H. Philipp, "Silicon dioxide (sio₂)(glass)," in *Handbook of Optical Constants of Solids*, pp. 749–763, Elsevier Ltd., 1997.
- [290] I. Iatsunskiy, E. Coy, R. Viter, G. Nowaczyk, M. Jancelewicz, I. Baleviciute, K. Załeński, and S. Jurga, "Study on structural, mechanical, and optical properties of al₂o₃–tio₂ nanolaminates prepared by atomic layer deposition," *The Journal of Physical Chemistry C*, vol. 119, no. 35, pp. 20591–20599, 2015.
- [291] A. W. Peterson, M. Halter, A. Tona, K. Bhadriraju, and A. L. Plant, "Surface plasmon resonance imaging of cells and surface-associated fibronectin," *BMC Cell Biology*, vol. 10, no. 1, pp. 1–17, 2009.
- [292] W. Bogaerts, P. De Heyn, T. Van Vaerenbergh, K. De Vos, S. Kumar Selvaraja, T. Claes, P. Dumon, P. Bienstman, D. Van Thourhout, and R. Baets, "Silicon microring resonators," *Laser & Photonics Reviews*, vol. 6, no. 1, pp. 47–73, 2012.
- [293] S. Kumar, P. S. Maji, and R. Das, "Tamm-plasmon resonance based temperature sensor in a ta₂o₅/sio₂ based distributed bragg reflector," *Sensors and Actuators A: Physical*, vol. 260, pp. 10–15, 2017.

- [294] M. Kaliteevski, I. Iorsh, S. Brand, R. Abram, J. Chamberlain, A. Kavokin, and I. Shelykh, “Tamm plasmon-polaritons: Possible electromagnetic states at the interface of a metal and a dielectric bragg mirror,” *Physical Review B*, vol. 76, no. 16, p. 165415, 2007.
- [295] B. Augu  , M. C. Fuertes, P. C. Angelom  , N. L. Abdala, G. J. Soler Illia, and A. Fainstein, “Tamm plasmon resonance in mesoporous multilayers: toward a sensing application,” *ACS Photonics*, vol. 1, no. 9, pp. 775–780, 2014.
- [296] A.-L. Baudrion, F. de Leon-Perez, O. Mahboub, A. Hohenau, H. Ditlbacher, F. J. Garcia-Vidal, J. Dintinger, T. W. Ebbesen, L. Martin-Moreno, and J. R. Krenn, “Coupling efficiency of light to surface plasmon polariton for single subwavelength holes in a gold film,” *Optics Express*, vol. 16, no. 5, pp. 3420–3429, 2008.
- [297] M. Zhao, J. Wang, Y. Zhang, M. Ge, P. Zhang, J. Shen, and C. Li, “Self-referenced refractive index sensor based on double-dips method with bimetal-dielectric and double-groove grating,” *Optics Express*, vol. 30, no. 5, pp. 8376–8390, 2022.
- [298] D. Cai, Y. Lu, K. Lin, P. Wang, and H. Ming, “Improving the sensitivity of spr sensors based on gratings by double-dips method (ddm),” *Optics Express*, vol. 16, no. 19, pp. 14597–14602, 2008.
- [299] N. Zhang, W. Luo, L. Wang, J. Fan, W. Wu, M. Ren, X. Zhang, W. Cai, and J. Xu, “Strong in-plane scattering of acoustic graphene plasmons by surface atomic steps,” *Nature Communications*, vol. 13, no. 1, pp. 1–6, 2022.
- [300] L. Cui, J. Wang, and M. Sun, “Graphene plasmon for optoelectronics,” *Reviews in Physics*, vol. 6, p. 100054, 2021.
- [301] I. Epstein, D. Alcaraz, Z. Huang, V.-V. Pusapati, J.-P. Hugonin, A. Kumar, X. M. Deputy, T. Khodkov, T. G. Rappoport, J.-Y. Hong, *et al.*, “Far-field

- excitation of single graphene plasmon cavities with ultracompressed mode volumes,” *Science*, vol. 368, no. 6496, pp. 1219–1223, 2020.
- [302] A. Woessner, Y. Gao, I. Torre, M. B. Lundberg, C. Tan, K. Watanabe, T. Taniguchi, R. Hillenbrand, J. Hone, M. Polini, *et al.*, “Electrical 2π phase control of infrared light in a 350-nm footprint using graphene plasmons,” *Nature Photonics*, vol. 11, no. 7, pp. 421–424, 2017.
- [303] Z. Fei, A. Rodin, G. O. Andreev, W. Bao, A. McLeod, M. Wagner, L. Zhang, Z. Zhao, M. Thiemens, G. Dominguez, *et al.*, “Gate-tuning of graphene plasmons revealed by infrared nano-imaging,” *Nature*, vol. 487, no. 7405, pp. 82–85, 2012.
- [304] F. Wang, Y. Zhang, C. Tian, C. Girit, A. Zettl, M. Crommie, and Y. R. Shen, “Gate-variable optical transitions in graphene,” *Science*, vol. 320, no. 5873, pp. 206–209, 2008.
- [305] D. R. Mason, S. G. Menabde, S. Yu, and N. Park, “Plasmonic excitations of 1d metal-dielectric interfaces in 2d systems: 1d surface plasmon polaritons,” *Scientific Reports*, vol. 4, no. 1, pp. 1–6, 2014.
- [306] S. A. Mikhailov and K. Ziegler, “New electromagnetic mode in graphene,” *Physical Review Letters*, vol. 99, no. 1, p. 016803, 2007.
- [307] O. Kotov, M. Kol’chenko, and Y. E. Lozovik, “Ultrahigh refractive index sensitivity of te-polarized electromagnetic waves in graphene at the interface between two dielectric media,” *Optics Express*, vol. 21, no. 11, pp. 13533–13546, 2013.
- [308] T. M. Wijesinghe, M. Premaratne, and G. P. Agrawal, “Low-loss dielectric-loaded graphene surface plasmon polariton waveguide based biochemical sensor,” *Journal of Applied Physics*, vol. 117, no. 21, p. 213105, 2015.

- [309] H. Lu, B. P. Cumming, and M. Gu, “Highly efficient plasmonic enhancement of graphene absorption at telecommunication wavelengths,” *Optics Letters*, vol. 40, no. 15, pp. 3647–3650, 2015.
- [310] M. Sun, T. Sun, Y. Liu, L. Zhu, F. Liu, Y. Huang, and C. Chang-Hasnain, “Integrated plasmonic refractive index sensor based on grating/metal film resonant structure,” in *High Contrast Metastructures V*, vol. 9757, pp. 86–91, SPIE, 2016.
- [311] L. Li, Y. Liang, J. Guang, W. Cui, X. Zhang, J.-F. Masson, and W. Peng, “Dual kretschmann and otto configuration fiber surface plasmon resonance biosensor,” *Optics Express*, vol. 25, no. 22, pp. 26950–26957, 2017.
- [312] A. Bijalwan and V. Rastogi, “Sensitivity enhancement of a conventional gold grating assisted surface plasmon resonance sensor by using a bimetallic configuration,” *Applied Optics*, vol. 56, no. 35, pp. 9606–9612, 2017.
- [313] F.-C. Chien and S.-J. Chen, “A sensitivity comparison of optical biosensors based on four different surface plasmon resonance modes,” *Biosensors and Bioelectronics*, vol. 20, no. 3, pp. 633–642, 2004.
- [314] H. Cai, M. Wang, J. Liu, and X. Wang, “Theoretical and experimental study of a highly sensitive spr biosensor based on au grating and au film coupling structure,” *Optics Express*, vol. 30, no. 15, pp. 26136–26148, 2022.
- [315] C. How Gan, “Analysis of surface plasmon excitation at terahertz frequencies with highly doped graphene sheets via attenuated total reflection,” *Applied Physics Letters*, vol. 101, no. 11, p. 111609, 2012.
- [316] Y. V. Bludov, M. I. Vasilevskiy, and N. M. Peres, “Tunable graphene-based polarizer,” *Journal of Applied Physics*, vol. 112, no. 8, p. 084320, 2012.
- [317] Y. V. Bludov, N. M. Peres, and M. I. Vasilevskiy, “Unusual reflection of electromagnetic radiation from a stack of graphene layers at oblique incidence,” *Journal of Optics*, vol. 15, no. 11, p. 114004, 2013.

- [318] D. K. Efetov and P. Kim, “Controlling electron-phonon interactions in graphene at ultrahigh carrier densities,” *Physical Review Letters*, vol. 105, no. 25, p. 256805, 2010.
- [319] W. M. Haynes, *CRC handbook of chemistry and physics*. CRC Press Ltd., Florida, 2014.
- [320] A. K. Sharma and A. K. Pandey, “Self-referenced plasmonic sensor with tio 2 grating on thin au layer: simulated performance analysis in optical communication band,” *JOSA B*, vol. 36, no. 8, pp. F25–F31, 2019.
- [321] Z. Lin, S. Chen, and C. Lin, “Sensitivity improvement of a surface plasmon resonance sensor based on two-dimensional materials hybrid structure in visible region: A theoretical study,” *Sensors*, vol. 20, no. 9, p. 2445, 2020.
- [322] S. Pal, A. Verma, J. P. Saini, and Y. K. Prajapati, “Sensitivity enhancement using silicon-black phosphorus-tdmc coated surface plasmon resonance biosensor,” *IET Optoelectronics*, vol. 13, no. 4, pp. 196–201, 2019.
- [323] C. Hwang, D. A. Siegel, S.-K. Mo, W. Regan, A. Ismach, Y. Zhang, A. Zettl, and A. Lanzara, “Fermi velocity engineering in graphene by substrate modification,” *Scientific Reports*, vol. 2, no. 1, pp. 1–4, 2012.
- [324] S. V. Vegesna, V. J. Bhat, D. Bürger, J. Dellith, I. Skorupa, O. G. Schmidt, and H. Schmidt, “Increased static dielectric constant in znmno and zncoo thin films with bound magnetic polarons,” *Scientific Reports*, vol. 10, no. 1, pp. 1–11, 2020.
- [325] J.-H. Chen, C. Jang, S. Xiao, M. Ishigami, and M. S. Fuhrer, “Intrinsic and extrinsic performance limits of graphene devices on sio₂,” *Nature Nanotechnology*, vol. 3, no. 4, pp. 206–209, 2008.
- [326] D. E. Aspnes and A. Studna, “Dielectric functions and optical parameters of si, ge, gap, gaas, gasb, inp, inas, and insb from 1.5 to 6.0 ev,” *Physical Review B*, vol. 27, no. 2, p. 985, 1983.

- [327] W. Yu and R. Mittra, "A conformal finite difference time domain technique for modeling curved dielectric surfaces," *IEEE Microwave and Wireless Components Letters*, vol. 11, no. 1, pp. 25–27, 2001.
- [328] Y. Huang, S. Zhong, H. Yao, and D. Cui, "Tunable terahertz plasmonic sensor based on graphene/insulator stacks," *IEEE Photonics Journal*, vol. 9, no. 1, pp. 1–10, 2017.
- [329] S. L. Harris and D. Harris, *Digital design and computer architecture*. Morgan Kaufmann Ltd., Burlington, USA, 2015.
- [330] Y. Xu, L. Wu, and L. K. Ang, "Mos₂-based highly sensitive near-infrared surface plasmon resonance refractive index sensor," *IEEE Journal of Selected Topics in Quantum Electronics*, vol. 25, no. 2, pp. 1–7, 2018.
- [331] X. Dai, Y. Liang, Y. Zhao, S. Gan, Y. Jia, and Y. Xiang, "Sensitivity enhancement of a surface plasmon resonance with tin selenide (snse) allotropes," *Sensors*, vol. 19, no. 1, p. 173, 2019.
- [332] Y. Jia, Y. Liao, and H. Cai, "Sensitivity improvement of surface plasmon resonance biosensors with ges-metal layers," *Electronics*, vol. 11, no. 3, p. 332, 2022.
- [333] S. Singh, A. K. Sharma, P. Lohia, and D. Dwivedi, "Theoretical analysis of sensitivity enhancement of surface plasmon resonance biosensor with zinc oxide and blue phosphorus/mos₂ heterostructure," *Optik*, vol. 244, p. 167618, 2021.
- [334] L. Wu, Y. Xiang, and Y. Qin, "Ch₃nh₃pbbr₃ thin film served as guided-wave layer for enhancing the angular sensitivity of plasmon biosensor," *Biosensors*, vol. 11, no. 11, p. 415, 2021.